TEMPO Ozone Profile Retrieval Algorithm Theoretical Basis Document

Junsung Park[1], Xiong Liu[1], Juseon Bak[2] and Kelly Chance[1]
[1]Center for Astrophysics | Harvard & Smithsonian
[2]Pusan National University

Corresponding author: Junsung Park (joonsung.park@cfa.harvard.edu)

VERSION	v1.0
RELEASE DATE	April 10, 2026
KEYWORDS	OZONE OZONE PROFILE TEMPO AIR QUALITY ATMOSPHERIC CHEMISTRY
REVIEWERS	Dr. Arno Keppens (Royal Belgian Institute for Space Aeronomy) Dr. Matthew S. Johnson (NASA Ames Research Center)
DOI	10.5067/doc/tempo/RetrievalAlgorithmTheoretical/BasisDocumentV1.0

This document should be cited as:
Park, J., Liu, X., Bak, J., & Chance, K. (2026). TEMPO Ozone Profile Retrieval Algorithm Theoretical Basis Document. NASA Algorithm Publication Tool, https://doi.org/10.5067/doc/tempo/RetrievalAlgorithmTheoretical/BasisDocumentV1.0

Table of Contents

Abstract

This Algorithm Theoretical Basis Document (ATBD) describes the retrieval algorithm and product details for the Level 2 Ozone Profile (O3PROF) product from the Tropospheric Emissions: Monitoring of Pollution (TEMPO) satellite instrument. For the TEMPO O3PROF retrieval algorithm version 4 (V04), the first publicly released version, an optimal estimation-based algorithm has been developed for retrieving ozone profiles from backscattered radiances from 308 to 340 nm in the UV (spectral fitting windows are subject to change in the future and can also be extended to the visible band (~540–650 nm)). This algorithm implements computationally expensive online radiative transfer calculation. Therefore, to meet processing time requirements, retrievals are performed on spatially co-added pixels (currently 4 pixels in the N/S direction, resulting in an O3PROF pixel footprint of approximately 8 km × 4.75 km at the center of the field of regard). The main product parameters are partial ozone columns in DU at 24 layers from the surface (determined by actual terrain height rather than sea level) to ~60 km, with the first layer from surface to surface +2 km (i.e., 0–2 km ozone above ground-level), and their random-noise and smoothing error profiles with total, stratospheric, and tropospheric ozone columns. This ATBD describes the TEMPO V04 O3PROF data product's retrieval algorithm, algorithm inputs and outputs, validation, and practices for best use.

Plain Language Summary

TEMPO (Tropospheric Emissions: Monitoring of Pollution) is a satellite mission in geostationary orbit that measures trace gases, clouds, and aerosols of importance to air quality. This document describes the retrieval algorithm and product details of the TEMPO Ozone Profile (O3PROF) product.

Version Description

This is Version 1.0 (initial release) of the TEMPO ozone profile ATBD. This document was initially released under DOI 10.5067/doc/tempo/RetrievalAlgorithmTheoretical/BasisDocumentV1.0 on April 10, 2026.

1. Introduction

1.1. TEMPO Overview

Tropospheric Emissions: Monitoring of Pollution (TEMPO) is NASA's first Earth Venture Instrument (EVI-1) project, selected in 2012. It is a PI-led instrument project at the Smithsonian Astrophysical Observatory (SAO) with project management at NASA Langley Research Center (LaRC) and instrument development at Ball Aerospace and Technologies Corporation (now BAE Systems). TEMPO is NASA's first payload to be hosted on a commercial spacecraft. After the TEMPO instrument delivery in November 2018, the TEMPO mission partnered with the satellite provider Maxar in 2019 and the host Intelsat in 2020. The TEMPO instrument was launched on April 7, 2023 on board the commercial communication satellite Intelsat-40e (IS-40e) by a SpaceX Falcon 9 rocket into a geostationary orbit (GEO) at 91° W. TEMPO's first direct sun observation took place on August 1, 2023, followed by the first Earth-view observations on August 2, 2023. TEMPO began nominal operations on October 17, 2023.

TEMPO uses the ultraviolet/visible (UV/VIS) spectroscopic technique to measure atmospheric pollution across North America, from Mexico City/Puerto Rico to the Canadian oil sands, and from the Atlantic to the Pacific, hourly and at high spatial resolution (the native spatial sampling is approximately 2 km × 4.75 km at the center of the Field of Regard (FOR)). TEMPO spectroscopic measurements in the UV (293–494 nm) and VIS (538–741 nm) wavelengths provide a tropospheric measurement suite that includes key gases of tropospheric air pollution chemistry. Measurements are made from GEO, which allows for nearly continuous daylight monitoring to capture the inherent high temporal variability in pollutants due to emissions, chemistry, and meteorology. TEMPO's small spatial footprint resolves pollution sources at a suburban scale.

TEMPO measures the spectra required to retrieve the mission baseline data products of total column and profile ozone (O_3), nitrogen dioxide (NO_2), formaldehyde (HCHO), and cloud fraction and pressure. In addition, TEMPO spectra can also be used to derive sulfur dioxide (SO_2), bromine monoxide (BrO), glyoxal ($C_2H_2O_2$), water vapor (H_2O), nitrous acid (HNO_2), aerosols, and Ultraviolet B (UVB) radiation. TEMPO thus can measure the major constituents, directly or by proxy, involved in tropospheric O_3 chemistry, as well as several other tropospheric and stratospheric constituents. TEMPO provides near-real-time air quality products disseminated to the public via the Atmospheric Science Data Center (ASDC) at NASA LaRC.

TEMPO makes the first tropospheric trace gas measurements from GEO for North America by building upon the heritage of six spectrometers operating in low Earth orbit (LEO): the Global Ozone Monitoring Experiment (GOME) (Burrows et al., 1999), the Scanning Imaging Absorption Spectrometer for Atmospheric Cartography (SCIAMACHY) (Bovensmann et al., 1999), the Ozone Monitoring Instrument (OMI) (Levelt et al., 2006), GOME-2 (Munro et al.,

2016), Ozone Mapping and Profiler Suite (OMPS) (Flynn et al., 2014), and Tropospheric Monitoring Instrument (TROPOMI) (Veefkind et al., 2012), as well as the Geostationary Environment Monitoring Spectrometer (GEMS) instrument (Kim et al., 2020), launched into GEO in 2020 to measure air pollutants over eastern Asia. These legacy instruments have demonstrated the technologies necessary to provide the measurement precision required for TEMPO using very similar retrieval algorithms. Novel to the GEO missions are hourly measurements with finer spatial resolution. This observational strategy makes TEMPO an innovative application of well-proven techniques, producing a revolutionary dataset for air quality science and applications over North America.

1.2. TEMPO Instrument and Measurements

Table 1.1 shows key characteristics of the TEMPO instrument and nominal hourly measurements. More instrument details can be found in Zoogman et al. (2017) and the TEMPO Level 1B (L1B) Algorithm Theoretical Basis Document (Chong et al., 2026). The TEMPO instrument is a UV/VIS imaging grating spectrometer using two 2-D 2k × 1k charge-coupled device (CCD) detectors in one focal plane covering the two bands ~293–494 nm (referred to as the UV band) and ~538-741 nm (VIS band). The 2k (2048) dimension is for the spatial direction and 1k (1028) dimension is for the spectral direction. The TEMPO instrument slit aligns with the North/South (N/S) direction and simultaneously measures 2048 (N/S or across-track) spatial pixels, of which 2036 pixels have good performance. Each band has 1028 spectral pixels, of which ~1016 pixels have good performance. The spectral resolution is ~0.6 nm at full width at half maximum (FWHM) and the spectral interval is ~0.2 nm. Examples of typical TEMPO spectra with absorption features are shown in Figure 1.1.

Table 1.1. *TEMPO instrument and measurement characteristics*

Volume, Mass	1.4 m × 1.1 m × 1.2 m, 137 kg
Average operating power	138 W
Detector size	Two 2048 (spatial) × 1028 (spectral) detectors
Wavelength range	UV band: ~293–494 nm, VIS band: 538–741 nm
Spectral resolution	~0.6 nm @ FWHM (0.54–0.63 nm)
Spectral sampling	~0.2 nm or ~3 pixels / FWHM (2.7–3.2 nm)
Spectral co-registration[1]	< 0.1 pixel (for UV, visible, UV/visible)
Orbit	Geostationary (35786 km), 91.0°W above the Equator
Instantaneous field of view[2]	41.49 µrad (N/S) × 129.20 µrad (E/W)
Modulation Transfer Function @Nyquist[2]	0.31-0.41 (N/S) × 0.38-0.49 (E/W)
Field of view[2,3]	4.87° (N/S) × 8.66° (E/W)
Spatial resolution[2]	2.0 km (N/S) × 4.75 km (E/W) at center of field of regard (FOR) (33.5231°N, 89.2170°W)
Temporal resolution[4]	~1 hour, ~3-second snapshot per mirror step

Spectra per hour [2,3,4,5]	2036 (N/S) × 1181 (E/W)
Maximum Signal-to-Noise Ratio[6]	1372–1394 at 330–340 nm

[1]Smile (mapping of the same wavelength to different pixels of the focal plane for different spatial columns), keystone (deviation of signal mapping from the correct spatial channel across the focal plane), and UV/visible co-alignment are within 0.1 pixel.
[2]N/S represents the North/South (across-track) direction; E/W represents the East/West (mirror step) direction.
[3]Estimated with a 128 µrad E/W mirror step size (1.2 µrad overlapping between two steps) and 1181 positions.
[4]For the nominal mode. In the early morning or late afternoon, optimized modes can measure the daylight portion every ~40 minutes. Special modes can measure a selected portion of FOR every 5–10 minutes.
[5]2036 out of 2048 spatial pixels are valid pixels.
[6]For the nominal radiance without pixel binning, derived using in-flight data from September 1, 2023.

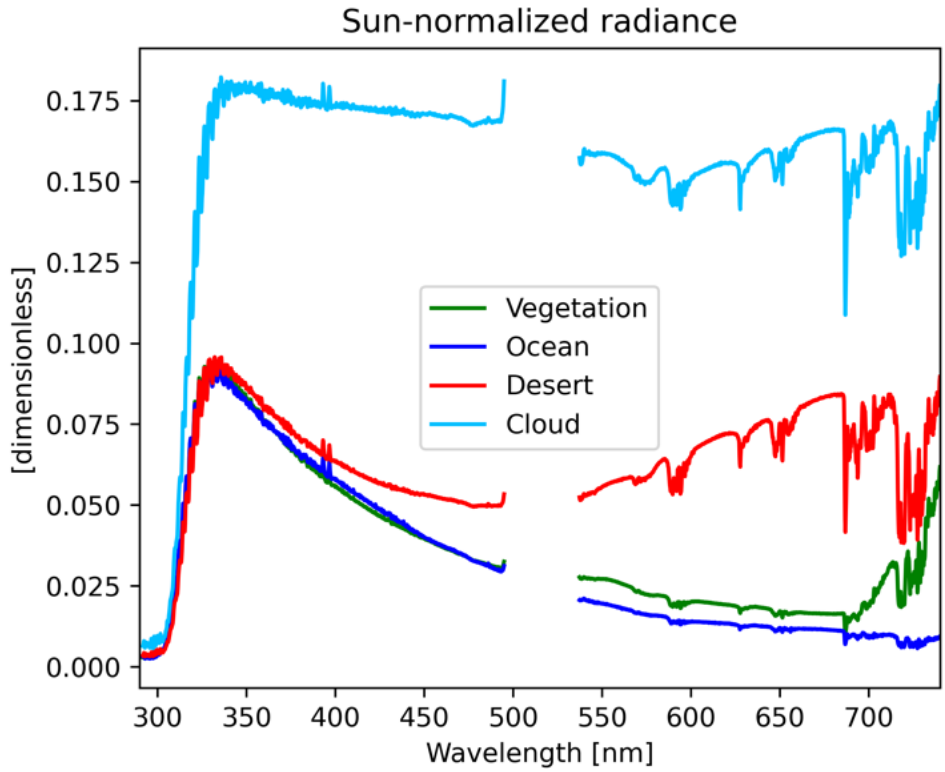

Figure 1.1. *Examples of a typical TEMPO Sun-normalized radiance spectra observed over vegetation (green), ocean (blue), desert (red), and cloud (cyan) scenes. The spectral coverage includes UV bands (~293–494 nm) and VIS bands (~538–741 nm).*

TEMPO can make three types of measurements: Earth-view radiance, solar irradiance, and dark current measurements. The Calibration Mechanism Assembly (CMA) controls the instrument aperture via a wheel with four selectable positions (open, closed, working diffuser, reference diffuser). The two diffusers allow recording of the top-of-atmosphere solar irradiance. The working diffuser is used on a more frequent (e.g., weekly) basis, and the reference diffuser is used every 3–6 months to assess trends in degradation of the working diffuser from radiation exposure and contamination. Solar measurements may be made when the Sun is unobscured

within 30° to the instrument boresight during night. Earth-view radiance measurements are made in the open position during the daytime. Dark current data are collected with the wheel in the closed position a few times each day, before and after the Earth-view, and before the solar measurements.

In a typical day, the TEMPO scan pattern includes optimized scanning in the early morning and late afternoon/evening, and nominal hourly scanning during the middle of the day. A TEMPO nominal hourly scan samples the entire FOR from East to West within 1 hour in 1181 mirror steps. The early morning and late afternoon/evening optimized scans increase the temporal sampling of the sunlit portion of the FOR to every 40 minutes by skipping observations over the dark parts of the continent. Hourly scans are split into 9 granules; each granule includes ~6.7 minutes of data. Due to the fixed Instantaneous Field of View (IFOV), the footprint size on the ground depends on the viewing zenith angle (VZA). The footprint is ~2.0 km (N/S) × 4.75 km (E/W) (~9.5 km^2) at the center of the FOR, with an area varying from ~1.65 km (N/S) × 4.54 km (E/W) (~7.5 km^2) over Mexico City to ~3.94 km × 5.05 km (E/W) (~20 km^2) over the Canadian oil sands. In addition to performing standard operations, TEMPO can use up to 25% of the observation time to perform special observations in high-time scan mode, scanning a selected portion of the FOR (i.e., N/S strip) at much higher temporal resolution (e.g., 5–10 minutes). Special observations can alternate with nominal hourly scans (e.g., 1-hour special observation followed by 1-hour nominal scan of FOR).

Figure 1.2 shows the signal-to-noise ratio (SNR) at native pixel resolution for the nominal radiance, which is a clear-sky average radiance over the TEMPO FOR from different seasons, and was used for SNR requirement analyses since the inception of the TEMPO project. An integration time of 100 milliseconds with 26 frames is used to minimize saturation while scanning the FOR within 1 hour in 1181 mirror steps. The SNR maximizes at ~1350 around 330–380 nm, while it is ~900 at 450 nm and ~500–900 for the VIS band. Below 330 nm, it quickly decreases to 750, 190, and 20 at 320, 310, and 300 nm, respectively.

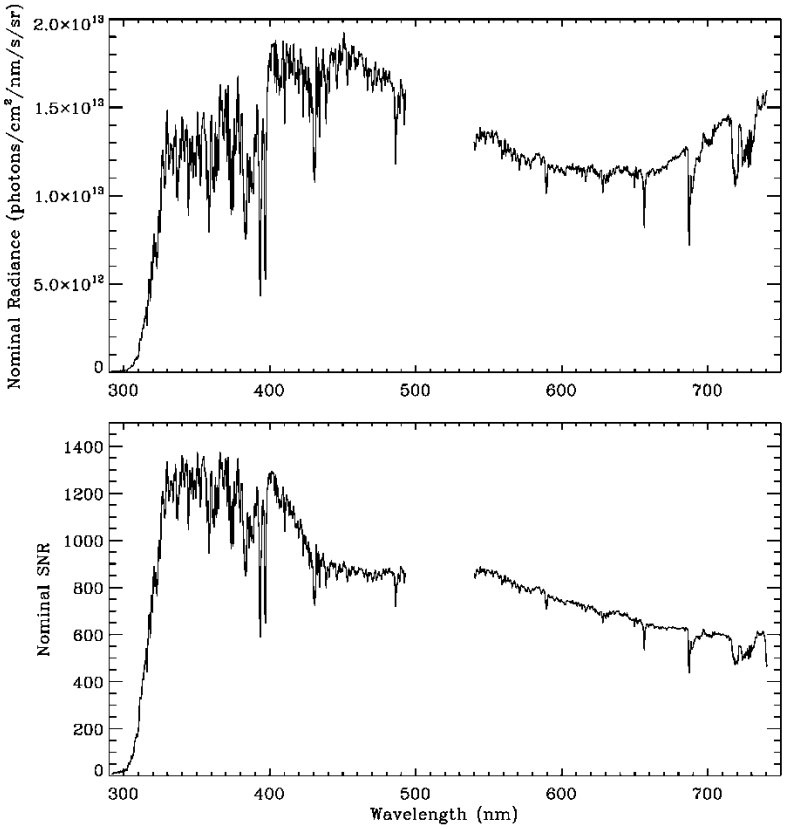

Figure 1.2. *Nominal radiance used in TEMPO SNR requirement and verification analysis (top) and final SNR at native pixel resolution (bottom) for 100 milliseconds integration time with 26 frames and a total coverage time of 59.8 minutes with 1181 mirror steps.*

1.3. Scope of this ATBD

The purpose of this algorithm theoretical basis document (ATBD) is to describe the theoretical basis and practical implementation of the TEMPO ozone profile retrieval algorithm, which uses a nonlinear optimal estimation (Rodgers, 2000). The generated output contains the retrieved ozone profiles, including 0–2 km ozone above the surface, a priori ozone profile and associated error, total column ozone, stratospheric column ozone, tropospheric column ozone, and other fitting variables such as surface albedo and cloud fraction, which are composed of state vectors in the retrieval algorithm. It contains random noise and total retrieval error profiles for ozone, the covariance matrix, the averaging kernels (AKs), degrees of freedom for signal, fitting residuals, and the root-mean-square error of fitting residuals, which are very useful parameters for evaluating a retrieved profile.

1.4. Ozone Profile

Figure 1.3 shows examples of the retrieved total column ozone and the tropospheric column, which are calculated by integrating the retrieved ozone profile, from a typical hourly scan of TEMPO. The observation data have been filtered for cloudy pixels, as UV/VIS measurements of tropospheric pollutants are generally inaccurate under thick clouds.

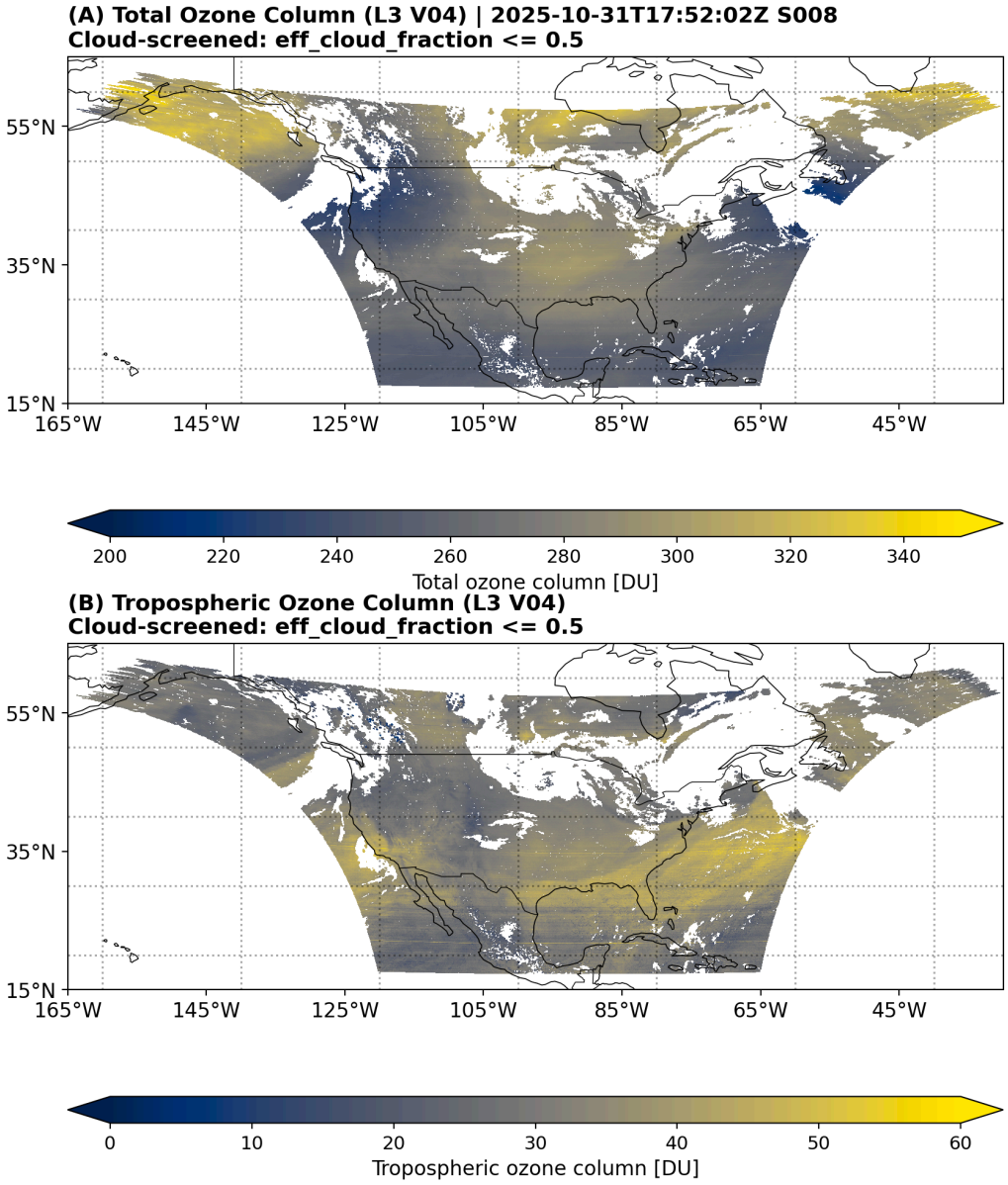

Figure 1.3. (A) *Total column ozone and (B) tropospheric column ozone retrieved using TEMPO spectra observed on October 31, 2025, scan 8 at 17:52 (UTC). In this figure, observations with an effective cloud fraction higher than 0.5 have been masked to avoid misinterpretation.*

Ozone is a gas composed of three atoms of oxygen that is naturally present in our atmosphere. About 90% of the total is in the stratosphere, centered at about 20–30 km, with the remaining 10% in the troposphere. Ozone has a profound influence on the atmosphere and life on Earth. The ozone layer in the stratosphere acts as a protector of the Earth's life from harmful solar UV radiation that can cause skin cancer and immune system suppression. Ozone in the troposphere is the primary precursor of the Hydroxyl (OH) radical that controls the tropospheric oxidizing capacity (Crutzen, 1988; Thompson, 1992). As an important greenhouse gas, ozone in the Upper

Troposphere and Lower Stratosphere (UTLS) plays an important role in the tropospheric energy budget (Fishman et al., 1979; Lacis et al., 1990; Cooper et al., 2002; Worden et al., 2008; Joiner et al., 2009). Near the surface, ozone is a major pollutant and toxic to biota (Reich & Amundson, 1985; Chameides et al., 1994). Due to its key roles in different parts of the atmosphere, monitoring its vertical distribution globally is essential to understand atmospheric processes, track stratospheric ozone depletion and its recovery, monitor tropospheric pollution, improve surface UV forecasting, and estimate its climate forcing.

2. Context/Background

2.1. BUV/Visible Measurements for Ozone Profile Retrievals and Physical Principles

Space-borne observations of ozone profiles and total ozone from nadir-viewing Backscatter Ultraviolet (BUV) radiances have been routinely performed since 1978 with the Solar Backscatter Ultraviolet (SBUV) and SBUV-2 instruments flown on the National Aeronautics and Space Administration (NASA) and the National Oceanic and Atmospheric Administration (NOAA) satellites. Because these instruments measure BUV radiances only at 12 discrete wavelength bands in the range of 256–340 nm, the information on ozone vertical distribution is limited mostly to 20–50 km (Bhartia et al., 1996). Chance et al. (1997) conducted a theoretical study to show that the retrieval of vertical ozone profiles can be extended down to the troposphere with BUV spectrum in the Hartley and Huggins bands and VIS spectrum in the Chappuis bands (Figures 2.1 and 2.2). Our theoretical study shows that combining UV with the visible spectrum can significantly enhance retrieval sensitivity to ozone near the surface and help distinguish boundary layer ozone from free tropospheric ozone (Natraj et al., 2011; Cai et al., 2012), which is why we have a VIS band in the TEMPO instrument (Figure 2.2).

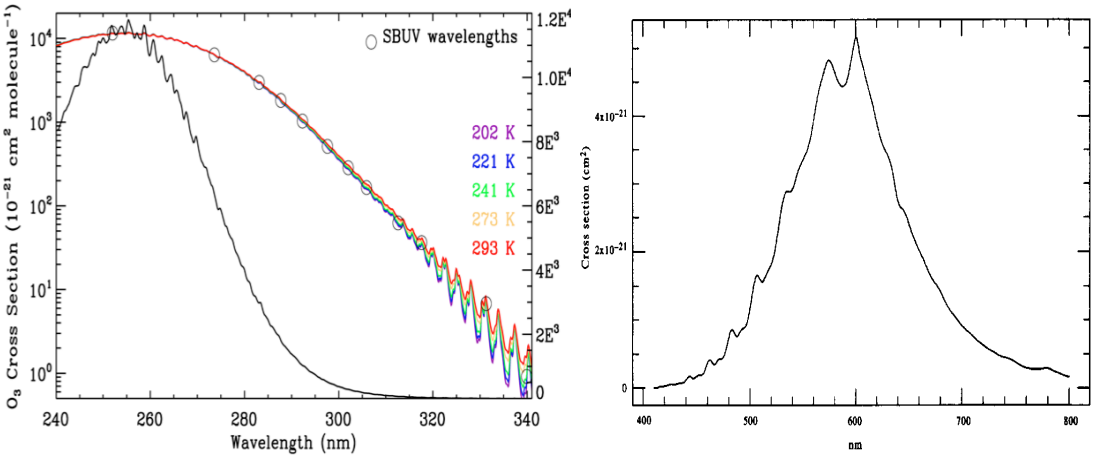

Figure 2.1. *Ozone absorption cross sections at five different temperatures in the UV (left) and VIS (right) wavelengths.*

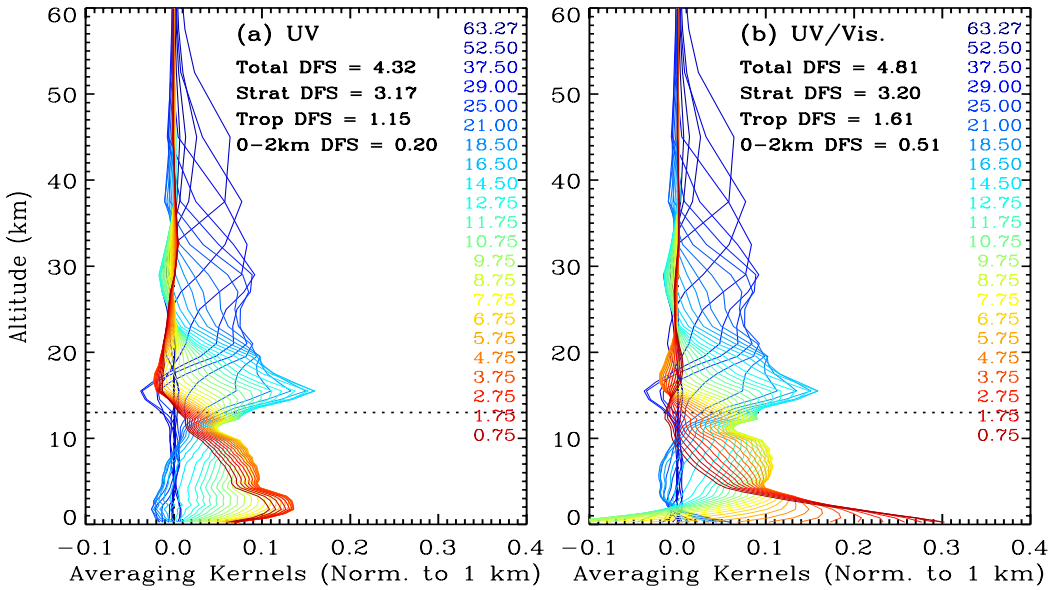

Figure 2.2. *Comparison of ozone retrieval averaging kernels using (a) UV only (290-345 nm) and (b) joint UV and VIS (540-650 nm). These examples are for a solar zenith angle of 25°, a viewing zenith angle of 45°, a relative azimuth angle of 86°, a TEMPO signal-to-noise ratio with 4 pixels coadded, and clear-sky conditions with a vegetation surface.*

BUV ozone profile and tropospheric column ozone retrievals have been demonstrated by several groups (Liu et al., 2005; Meijer et al., 2006, and references therein). After GOME and SCIAMACHY, BUV measurements have been included in subsequent similar LEO instruments such as OMI, GOME-2, OMPS, TROPOMI, and Sentinel-5/Ultraviolet-Visible-Near-infrared Shortwave-infrared Sounder (UVNS), as well as in geostationary instruments like GEMS, TEMPO, and Sentinel-4 UVN. VIS band measurements, including the Chappuis bands, have been included in the LEO instruments GOME, SCIAMACHY, and GOME-2. But measurements are split into two different channels at the peak of the Chappuis bands, making the use of VIS wavelengths to improve retrievals more difficult, mostly due to the exclusion of the Chappuis absorption peak and to potential radiometric calibration inconsistencies between the two channels. Currently, adding VIS to UV measurements to improve tropospheric ozone retrievals has been demonstrated in early neural network-based studies using SCIAMACHY data (Sellitto et al., 2012a, 2012b). Furthermore, the broader concept of integrating multiple independent spectral bands, utilizing soft calibration to radiometrically match them, has now been successfully established in the operational TROPOMI ozone profile retrieval (Di Pede et al., 2026; Keppens et al., 2024). For the V04 TEMPO Ozone Profile (TEMPO O3PROF) product, we applied the UV-only O3PROF retrieval algorithm and plan to add the visible band once sufficient retrieval accuracy is demonstrated.

In the Hartley and Huggins bands of the UV region, photons backscattered to space by the Earth's atmosphere and surface are mainly attenuated by the Rayleigh scattering and ozone absorption in a clean atmosphere. The magnitude of ozone absorption cross section decreases

dramatically by ~5 orders of magnitude in the wavelength range 270–340 nm, while the Rayleigh scattering varies inversely with wavelength ($\propto \lambda^{-4}$). In the Hartley bands (< ~300 nm), the incident light is mostly absorbed through the stratosphere. Figure 2.3 shows the normalized mean path length and its vertical gradient. At ~270 nm, photons can only penetrate to ~40 km. At ~295 nm, photons can penetrate to depths of ~20 km. At longer wavelengths in the Huggins bands (> ~305 nm), photons can penetrate deeper into the lower atmosphere. At wavelengths > 330 nm, sensitivity to ozone decreases across all layers due to reduced ozone absorption. Therefore, the penetration of photons into the atmosphere is dependent on the wavelength, providing vertical discrimination of ozone in the atmosphere. In addition, temperature-dependent ozone absorption in the Huggins bands provides additional vertical discrimination of ozone in the troposphere(Chance et al., 1997). In Figure 2.4, the sensitivity of normalized radiances to the ozone profile is plotted. Similarly, we can see that below 310 nm, the peak position of the sensitivities is well discriminated for altitudes between the 60 km and the ozone layer (~20 km). The sensitivity to tropospheric ozone could be obtained at wavelengths > 305 nm, but becomes weak for all layers at wavelengths > 330 nm. Despite having sensitivity to lower tropospheric ozone from the Huggins band, sensitivity to ozone near the surface and in the lower troposphere is still weak due to strong Rayleigh scattering in the lower troposphere that causes inadequate photon penetration. In the visible, more photons can penetrate to the surface due to weaker Rayleigh scattering. However, because the visible absorption signal is very weak, it is important to account for interferences from surface reflectance, aerosols, and other trace gases to ensure accurate radiometric calibration.

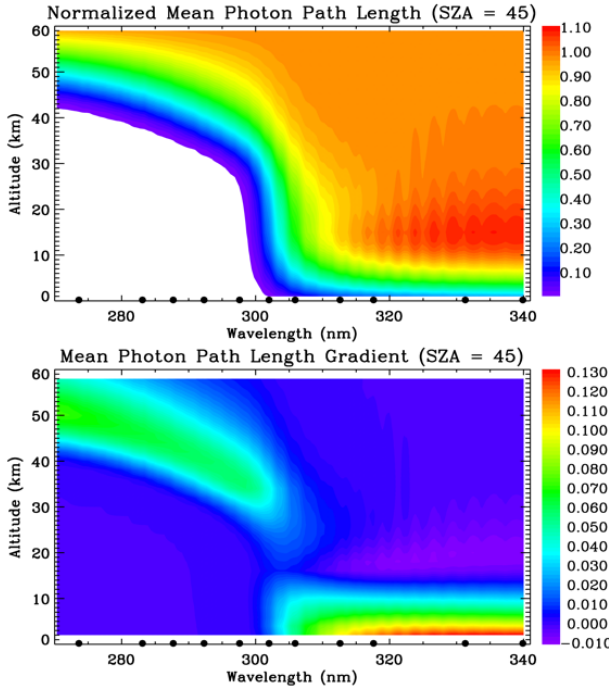

Figure 2.3. *(a) Mean air mass factor normalized to geometric air mass factor as a function of wavelength and altitude in the UV at solar zenith angle 45°, and (b) its vertical gradient that determines ozone vertical sensitivity.*

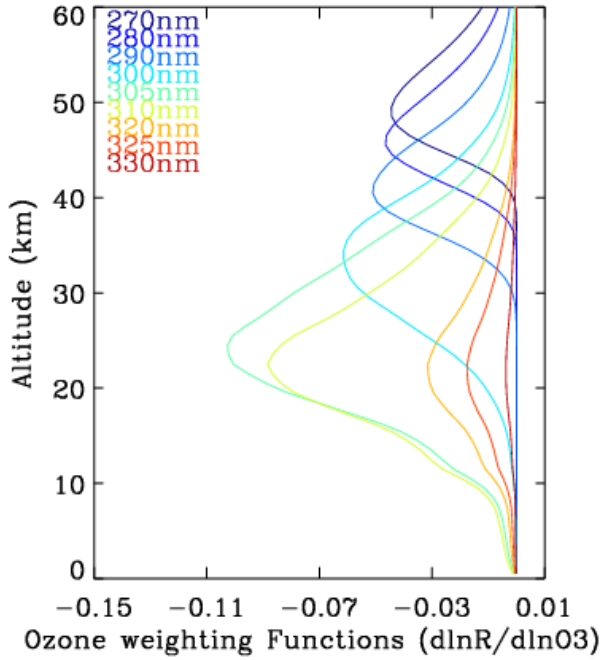

Figure 2.4. *Normalized weighting functions for ozone profile as a function of wavelengths for a typical ozone profile in mid-latitude regions at solar zenith angle 42°, viewing zenith angle 41°, relative azimuth angle 180°, and surface reflectivity 0.06. The x-axis (dlnR/dlnO_3) is dimensionless and represents the relative sensitivity, indicating the fractional change in the simulated radiance due to a fractional change in the ozone concentration at a given altitude.*

2.2. Algorithm Heritage

Our TEMPO ozone profile algorithm is adapted from our UV-only GOME and OMI ozone profile retrieval algorithms as described in detail in Liu et al. (2005, 2010a). Liu et al. (2005) developed an optimal estimation (OE) based algorithm (Rodgers, 2000) to retrieve ozone profiles, including tropospheric ozone, from GOME BUV radiance spectra. They demonstrated that weak tropospheric ozone information can be extracted from GOME measurements by improving the wavelength/radiometric calibrations and forward modeling simulations, reducing fitting residuals in the Huggins bands to 0.1–0.2%. Because the retrieval problem is ill-posed, UV-only GOME and OMI ozone profile retrievals are constrained and stabilized using the monthly- and zonal-mean a priori ozone profile climatology of McPeters et al. (2007), derived from 15 years of ozonesonde and Stratospheric Aerosol and Gas Experiment (SAGE) data, and instrument measurement errors.

This algorithm has also been successfully applied to BUV radiances measured by the OMI (Liu et al., 2010a, 2010b), GOME-2 data (Cai et al., 2012), OMPS (Bak et al., 2017a), and TROPOMI data (Bak et al., 2025; Zhao et al., 2021) for ozone profile retrievals, referred to as the SAO ozone profile retrieval algorithm, and also for retrievals of GOME-2 SO_2 (Nowlan et al., 2011). The SAO algorithm has also been adapted for ozone profile retrievals from BUV measurements by the GEMS instrument (Bak et al., 2013a, 2019a, 2026). GEMS is TEMPO's sister instrument,

also built by Ball Aerospace (now part of BAE System Inc.), and was launched in February 2020 for atmospheric pollution monitoring over Asia (Kim et al., 2020). Its main difference from TEMPO is that it does not have the visible band.

The TEMPO algorithm is adapted from the SAO ozone profile retrieval algorithm. In our OMI retrievals, the spectral regions from OMI UV1 (270–309 nm) and UV2 (312–330 nm) channels are used. Due to differences in channel spatial resolution, two UV2 pixels are co-added across the track. A first-order soft calibration, derived using two days of zonal-mean (latitudinal average) Microwave Limb Sounder (MLS) data (above 215 hPa) and climatological ozone (below 215 hPa) in the tropics, is applied to OMI radiances before the retrieval process, independent of latitude and time. Our OMI retrievals have been subsequently improved over the years (Kim et al., 2013; Bak et al., 2013a, 2016, 2017, 2019b, 2020, 2021a, 2021b) to improve ozone profile climatology using a tropopause-based climatology, radiative transfer calculation for both accuracy and speed based on a combination of Principal Component Analysis (PCA) applied to hyperspectral optical property dataset and look-up tables (LUTs) of radiance corrections, ozone cross sections, high-resolution solar reference, wavelength and slit function characterization, accounting for solar zenith angle (SZA) dependent systematic residuals, and improved meteorological data. Most of these improvements, as well as time-dependent soft calibration and improved meteorological data, are included in our OMI version 2 retrievals (Bak et al., 2024a) and have been adapted with specific optimizations to account for TEMPO's SNR and spatial resolution (e.g., co-adding 4 pixels in N/S direction). To ensure stable convergence and physical accuracy, the prior covariance matrix was refined by adjusting the vertical correlation lengths, thereby minimizing artificial compensation effects. Additionally, soft calibration was applied to mitigate systematic radiometric biases, the details of which are described in the following sections. Based on these adoptions, the current V04 TEMPO O3PROF algorithm performs UV-only retrieval. We plan to incorporate VIS measurements in a future version.

2.3. Algorithm Overview and Implementation

TEMPO data products are generated by the SAO Science Data Processing Center (SDPC) at the SAO and then pushed to NASA's ASDC for public distribution (https://asdc.larc.nasa.gov/project/TEMPO). These products include L1B spectra (calibrated solar irradiance and geolocated Earth-view radiances), Level 2 (L2) trace gases, ozone profile, and cloud products (provided at the native ground pixel footprint for the East-West granules that make up a TEMPO scan, with the exception of the ozone profile, which co-adds 4 pixels in the North-South direction). Furthermore, Level 3 (L3) trace gases, ozone profile, and cloud products, which are L2 data sampled on a regular grid (fixed grid size) for all granules constituting a single East-West scan, are also provided at the ASDC. These L3 products are gridded at 0.02° × 0.02° for NO_2, HCHO, cloud, and total column ozone, and 0.04° × 0.04° for O3PROF.

The SDPC generates the TEMPO products in the following order from Level 0 (raw data): 1) Level 1B; 2) Level 2 clouds; 3) Level 2 trace gases and ozone profile; and 4) Level 3 products. This order is required because the trace gas and ozone profile products are derived from the Level 1B spectra and require the cloud fraction and pressure.

2.4. Product Version

This document describes the TEMPO V04 ozone profile product produced through the SDPC operational processing pipeline. The V04 product was initially released to the public on September 17, 2025. Updates to the TEMPO operational pipeline result in periodic new data releases. The TEMPO ozone profile user guide (Park, et al., 2025, 2026) provides additional information on versioning history, data format, and usage recommendations. Table 2.1 describes the major public data releases and algorithm updates.

Table 2.1. *Product and Science Data Processing Center pipeline versions for public data releases*

Product Version Designation	**Science Data Processing Center Pipeline Version**	**Release Date**	**Significant Algorithm Updates**
V03	4.4	May 24, 2024	First release limited to the validation team
V04	4.7	September 17, 2025	First public release

2.5. Additional Information

Table 2.2. *List of acronyms and abbreviations*

Acronym/Abbreviation	**Definition**
AEROMMA	Atmospheric Emissions and Reactions Observed from Megacities to Marine Areas
AK	Averaging Kernel
AMF	Air Mass Factor
ARC	Ames Research Center
AQS	Air Quality System
ASDC	Atmospheric Science Data Center
ATBD	Algorithm Theoretical Basis Document
BDM	Brion-Daumont-Malicet
BRDF	Bidirectional Reflectance Distribution Function
BTDF	Bidirectional Transmission Distribution Function
BUV	Backscattered Ultraviolet
BW	Birk and Wagner
CCD	Charge-coupled device

CMA	Calibration Mechanism Assembly
CMC	Common Mode Correction
CUPIDS	Coastal Urban Plume Dynamics Study
DEM	Digital Elevation Model
DFS	Degrees of Freedom for the Signal
DSCOVR	Deep Space Climate Observatory
DU	Dobson Unit
EPIC	Earth Polychromatic Imaging Camera
E/W	East/West
EVI	Earth Venture Instrument
FNL	Final
FOR	Field of Regard
FT-IT	Forward Processing for Instrument Teams
FWHM	Full Width at Half Maximum
GEMS	Geostationary Environment Monitoring Spectrometer
GEO	Geostationary Earth Orbit
GEOS	Goddard Earth Observing System
GEOS-CF	GEOS Composition Forecast
GEOS FP-IT	GEOS Forward Processing Instrument Teams
GLER	Geometry-dependent surface Lambert Equivalent Reflectivity
GMAO	Global Modeling and Assimilation Office
GMTED	Global Multi-resolution Terrain Elevation Data
GOME	Global Ozone Monitoring Experiment
GOTHAAM	Greater New York Oxidant Trace Gas Halogen and Aerosol Airborne Mission
GSFC	Goddard Space Flight Center
HITRAN	High-Resolution Transmission Molecular Absorption Database
HEMCO	Harmonized Emissions Component
HSRS	Hybrid Solar Reference Spectrum
HTAP	Hemispheric Transport of Air Pollution
IAGOS	In-service Aircraft for a Global Observing Service
IFOV	Instantaneous Field of View
IGBP	International Geosphere Biosphere Program
ILS	Instrument Line Shapes
IMS	Interactive Multisensor Snow and Ice Mapping System
INR	Image Navigation and Registration
IPA	Independent Pixel Approximation
IS	Intelsat
ISRF	Instrument Spectral Response Functions
L1B	Level 1b

L2	Level 2
L3	Level 3
LaRC	Langley Research Center
LEO	Low Earth Orbit
LER	Lambertian Equivalent Reflectivity
LLM	Labow, Logan, and McPeters
LPS	Linear Polarization Sensitivity
LUT	Look-Up Table
MAX-DOAS	Multi-Axis Differential Optical Absorption Spectroscopy
MEGAN	Model of Emissions of Gases and Aerosols from Nature
ML	McPeters and Labow
MLER	Mixed Lambert Equivalent Reflectivity
MLS	Microwave Limb Sounder
MODIS	Moderate Resolution Imaging Spectroradiometer
MS	Multiple Scattering
N/S	North/South
NASA	National Aeronautics and Space Administration
NCEP	National Centers for Environmental Prediction
NDACC	Network for the Detection of Atmospheric Composition Change
NOAA	National Oceanic and Atmospheric Administration
O3PROF	Ozone Profile
OCP	Cloud Optical Centroid Pressure
OE	Optimal Estimation
OMI	Ozone Monitoring Instrument
OMPS	Ozone Mapping and Profiler Suite
PAs	Pseudo Absorbers
PCA	Principal Component Analysis
PGN	Pandonia Global Network
PI	Principal Investigator
PLRA	Program Level Requirements Appendix
QFED	Quick Fire Emission Database
RETRO	Reanalysis of the Tropospheric chemical composition
RMSE	Root Mean Square Error
RRS	Rotational Raman Scattering
RTM	Radiative Transfer Model
SAGE	Stratospheric Aerosol and Gas Experiment
SAO	Smithsonian Astrophysical Observatory
SBUV	Solar Backscatter Ultraviolet
SCIAMACHY	Scanning Imaging Absorption Spectrometer for Atmospheric Chartography
SCO	Stratospheric Column Ozone

SDPC	Science Data Processing Center
SNR	Signal-to-Noise Ratio
STAQS	Synergistic TEMPO Air Quality Science
Suomi NPP	Suomi National Polar-orbiting Partnership
SZA	Solar Zenith Angle
TB	Tropopause-Based
TCO	Total Column Ozone
TrCO	Tropospheric Column Ozone
TEMPO	Tropospheric Emissions: Monitoring of Pollution
TOA	Top of Atmosphere
TOLNet	Tropospheric Ozone Lidar Network
TROPESS	Tropospheric Ozone and its Precursors from Earth System Sounding
TROPOMI	Tropospheric Monitoring Instrument
TSIS	Total and Spectral Solar Irradiance Sensor
UARS	Upper Atmosphere Research Satellite
US	United States
USGS	United States Geological Survey
UTC	Coordinated Universal Time
UTLS	Upper Troposphere and Lower Stratosphere
UV	Ultraviolet
UVB	Ultraviolet B
V04	Version 4
VCD	Vertical Column Density
VIS	Visible
VLIDORT	Vector Linearized Discrete Ordinate Radiative Transfer
VOC	Volatile Organic Compound
VZA	Viewing Zenith Angle
WRF-Chem	Weather Research and Forecasting - Chemistry

Table 2.3. *List of symbols used in mathematical equations*

Meaning	**Symbol**
A priori covariance matrix	S_a
A priori state vector	X_a
Air mass factor	AMF
Asymmetric parameter	a_w
Averaging kernel matrix	A
Baseline mth-order polynomial	P_b^m
Clear scene reflectivity	R_s
Cloud fraction	f_c

Cloud pressure	p_c
Common mode correction spectrum and corresponding fitted CMC parameter	$\phi_{cmc}\ and\ \alpha_{cmc}$
Contribution function matrix	G
Corrected surface pressure	P_s
Cost function	χ^2
Degradation correction (typically in UV channel)	α_d
Earth's surface gravity acceleration	g
Effective terrain height	z_s
Floor noise	E_{fl}
GLER final value	a_s
GLER value representing snow-free	L_f
GLER value representing snow-covered	L_s
High-resolution solar reference spectrum	$I_{o,hr}$
ILS	s_λ
Measured radiance spectrum	Y
Measured error covariance matrix	S_y
Measurement random error of Y_m	E_m
Measurement vector before adjustment	Y_m
Forward model	F
Offset spectrum and fitted offset parameter	$\phi_{off}\ and\ \alpha_{off}$
Random-noise error covariance matrix	S_n
Relative random error in radiance	E_i
Relative random error in irradiance	E_{i0}
Retrieved state vector	$\hat{X}$
Scaling mth-order polynomial	P_s^m
Shape parameter	k
Simulated normalized radiance	Y_s
Simulated radiance with X	$F(X)$
Simulated spectrum	I_{0s}
Smoothing error covariance	S_s
Snow fraction	s_f
Soft calibration spectrum	ϕ_{soft}
Solar irradiance	I_0
Solar zenith angle	θ_0
Solution error covariance matrix	$\hat{S}$
Surface pressure from GEOS-CF	P_m
Temperature	T

Terrain altitude from GEOS-CF	z_m
TOA radiance	I
Undersampling spectrum and corresponding fitted undersampling coefficient	$\phi_{us,j}\ and\ \alpha_{us,j}$
Weighting function matrix	K
Wavelength	λ

Table 2.4. *List of chemical formulas*

Meaning	**Formula**
Bromine monoxide	BrO
Bromine Oxides (BrO + Br)	BrO_x
Formaldehyde	$HCHO$
Glyoxal	$C_2H_2O_2$
Hydrogen Oxides (OH + HO_2)	HO_X
Iodine monoxide	IO
Nitrogen dioxide	NO_2
Nitrogen Oxides (NO + NO_2)	NO_x
Nitrous acid	HNO_2
Molecular oxygen	O_2
Molecular oxygen collision complex	O_2-O_2
Ozone	O_3
Sulfur dioxide	SO_2
Volatile Organic Compounds	VOC
Water vapor	H_2O

3. Algorithm Description

Figure 3.1 shows a flowchart of the TEMPO O3PROF retrieval algorithm. Ozone profiles are retrieved from TEMPO UV (308–340 nm) radiances using the optimal estimation technique, with extensive online radiative transfer modeling and wavelength- and radiometric-calibrations. The retrievals are constrained by climatological a priori ozone and TEMPO radiance and irradiance errors. The a priori ozone profile error values for the climatological product are derived from the statistical variability of the historical observational data (such as ozonesondes and long-term satellite measurements) used to construct the climatology. The spectroscopic profile retrieval succeeds only when accurate calibration and forward model simulations, good knowledge of measurement errors, and a priori information (profiles and their covariance matrices) are available.

Section 3.1 introduces the optimal estimation technique for our ozone profile retrieval problem. Section 3.2 presents TEMPO measurements used for radiometric and wavelength calibrations. Section 3.3 describes forward model simulation (including radiative transfer model calculations, modeling of the Ring effect, and accounting for other parameters) and inputs in detail. Section 3.4 presents the implementation of the retrieval scheme details for the actual computation of the iterative optimal estimate in the TEMPO algorithm. Finally, an overview of the ozone profile product, including quality flags, is shown in Section 3.5.

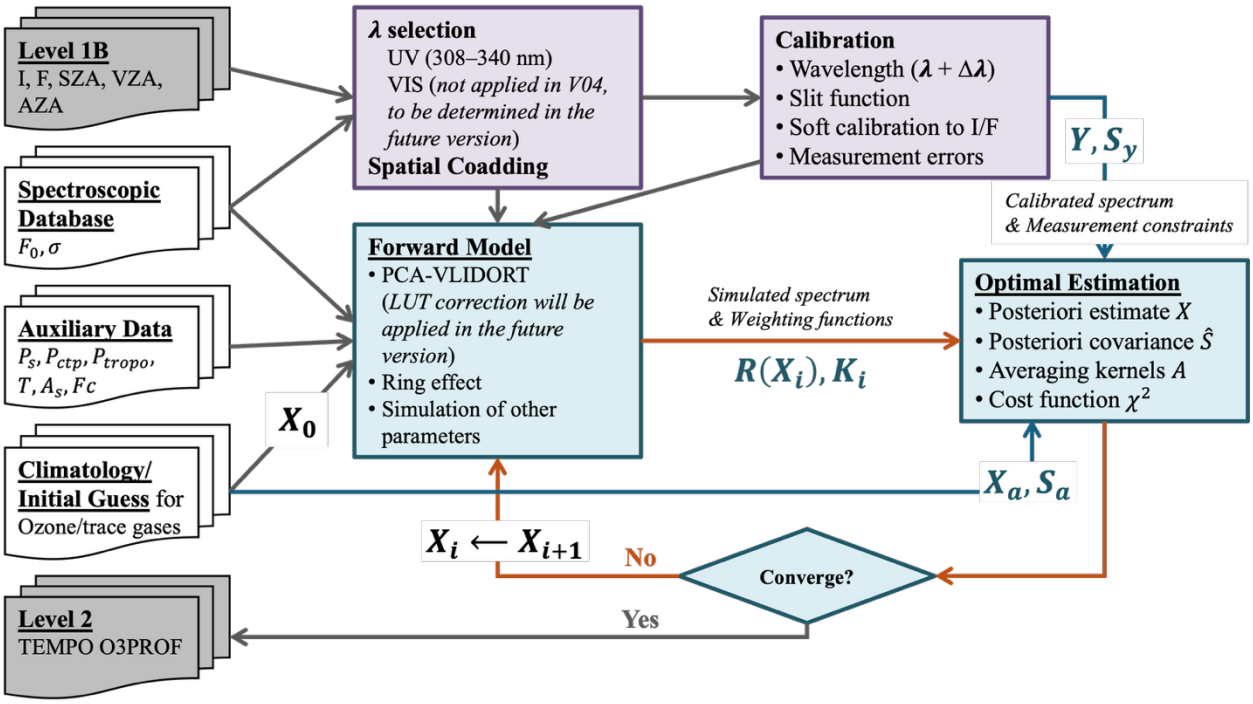

Figure 3.1. *Flowchart of the TEMPO ozone profile retrieval algorithm.*

3.1. Optimal Estimation Inversion Technique

We follow the notation of Rodgers (2000) to describe the optimal estimation formula. The quantities to be retrieved can be represented by the state vector, X consisting of the ozone profile, other geophysical parameters, and spectroscopic parameters that affect the observed radiances and hence the retrieval of the ozone profile. The measurement vector is given by Y. The relationship between X and Y is given by:

$$Y = F(X) \tag{3.1}$$

where F is the forward model and $F(X)$ is the (simulated) radiance with X. The linearization of the forward model with respect to a state vector element is given by:

$$K_{ij} = \partial F_i(X)/\partial X_j \tag{3.2}$$

where K is defined as a weighting function matrix. In retrieval theory, the weighting functions describe the response of the radiance to small deviations of the atmospheric parameters from a given atmospheric state. In mathematical terms, the weighting functions are partial derivatives of the forward model with respect to the atmospheric parameters. The retrieval involves the solution of the inverse problem:

$$X = F^{-1}(Y) \tag{3.3}$$

which is generally ill-posed or under-constrained, because the ozone profile is a continuous function of altitude, whereas TEMPO provides measurements only at a limited number of altitudes. In order to numerically solve the inverse problem, the ozone profile is discretized to a finite number of height levels. The inverse problem is also under-constrained because there are components in the actual ozone profile that do not contribute to the measurements and, consequently, cannot be determined directly from the retrieval. Thus, additional information is needed to retrieve a physically reasonable solution. The ozone profile algorithm normally uses the climatological a priori knowledge combined from long-term global ozonesonde measurements in the troposphere and lower stratosphere, and satellite measurements in the stratosphere. For the V04 TEMPO algorithm, the combined a priori knowledge was used based on Tropopause-Based (TB) climatology (Bak et al., 2013b) and the Goddard Earth Observing System Composition Forecast (GEOS-CF) version 2.

The optimal estimation method solves the non-linear inversion by simultaneously and iteratively minimizing the differences between measured and simulated radiances and between retrieved ($\hat{X}$) and a priori state (X_a) vectors, constrained by the measurement error covariance matrix (S_y) and the a priori covariance matrix (S_a), respectively. The cost function χ^2 can be written:

$$\chi^2 = \left\| S_y^{-\frac{1}{2}} \left\{ K_i\left(\hat{X}_{i+1} - \hat{X}_i\right) - \left[Y - F(\hat{X}_i)\right] \right\} \right\|_2^2 + \left\| S_a^{-\frac{1}{2}} \left(\hat{X}_{i+1} - X_a\right) \right\|_2^2 \tag{3.4}$$

In the iteration step i+1 the optimal estimation solution $\hat{X}_{i+1}$ is written as:

$$\hat{X}_{i+1} = \hat{X}_i + (K_i^T S_y^{-1} K_i + S_a^{-1})^{-1} \left\{ K_i^T S_y^{-1} \left[Y - F(\hat{X}_i)\right] - S_a^{-1}(\hat{X}_i - X_a) \right\} \tag{3.5}$$

The radiance and irradiance (and the errors) are taken from the L1B data. This algorithm defines the measurement as mainly the logarithm of the ratio of radiance to irradiance (the sun-

normalized radiance) with adjustment due to other parameters not handled in radiative transfer models. The measurement error covariance matrix is mainly based on a random precision estimate in both measured solar irradiance and radiance. The a priori error covariance S_a of ozone is taken from the climatological error constructed using various satellite and ozonesonde datasets (for the V04 TEMPO algorithm, the a priori errors are derived from the variance of long-term ozonesonde and MLS measurements relative to the TB climatology).
The optimal estimation provides a useful tool for the characterization of a retrieved profile and error analysis. The AK matrix, A, which represents the sensitivity of the retrieved state to the true state, is defined as follows:

$$A = \frac{\partial \hat{X}}{\partial X} = (K^T S_y^{-1} K + S_a^{-1})^{-1} K^T S_y^{-1} K = \hat{S} K^T S_y^{-1} K = GK \tag{3.6}$$

The AK matrix allows for robust comparison between measurements from two instruments with different vertical resolutions by smoothing the measurements with much higher vertical resolution with the AKs of the instrument with lower vertical resolution, $X'_{high} = X_a + A(X_{high} - X_a)$ and is therefore called a smoothing function. The FWHM of the AKs is used to characterize the vertical resolution of the retrieval. The diagonal elements of A give the Degrees of Freedom for Signal (DFS) at each layer. The DFS, calculated as the trace of the A, essentially represents the number of independent pieces of information (or independent layers) that can be retrieved from the measurements.

The matrix of contribution functions G may be described as a generalized inverse of K or the sensitivity of the retrieval to the measurement (measurement error), $\partial \hat{X}/\partial Y$. The quality and accuracy of the retrieval can be characterized by the solution error covariance matrix $\hat{S}$. It can be expressed as the sum of the random-noise error covariance matrix, S_n, which describes the error due to measurement noise, and of the smoothing error covariance matrix, S_s, which describes the error caused by the vertical (re)distribution of a priori information:

$$S_n = G S_y G^T \tag{3.7}$$

$$S_s = (A - I) S_a (A - I)^T \tag{3.8}$$

Optimal estimation is performed iteratively, so a convergence criterion has to be set to stop the iteration. The convergence criterion is based on the magnitude of the state vector update, and convergence has been reached when the relative change in the state vector, fit residuals, or cost function is less than some thresholds.

3.2. TEMPO Measurements and Calibrations

TEMPO radiance and solar irradiance measurements, together with their corresponding random measurement errors from L1B data, are used in the ozone profile retrievals. The solar irradiance reference spectrum is typically taken once a week. Because the SNR of the solar irradiance is much higher than that of the radiance, additional temporal averaging of the irradiance is unnecessary. In our OMI ozone profile retrievals, mean solar irradiances derived from three

years of OMI data were used to reduce short-term noise and seasonally varying errors in individual irradiance spectra (Liu et al., 2010a). In contrast, the V04 TEMPO O3PROF retrieval algorithm uses individual solar irradiance measurements.

TEMPO slit functions were characterized pre-launch and parameterized using a super-Gaussian function as a function of cross-track position at 15 wavelengths and then were interpolated to every wavelength. Although the L0-1b processor includes a basic wavelength calibration, on-orbit changes in the Instrument Line Shape (ILS) require further correction. Therefore, an additional wavelength calibration procedure is performed to derive the actual slit functions, thereby improving the wavelength registration for both radiance and solar irradiance. Additional parameters can be included in the main spectral fitting to account for wavelength shifts and Instrument Spectral Response Function (ISRF) changes on a pixel-to-pixel basis (Bak et al., 2019b). Also, empirical radiometric calibration or soft calibration is typically employed for BUV retrievals due to inadequate radiometric calibration or forward model simulations (Liu et al., 2010a; Cai et al., 2012; Bak et al., 2017, 2024; Zhao et al., 2021). Other corrections might be included as Pseudo Absorbers (PAs) in the main fitting to account for instrument undersampling (Chance et al., 2005), offsets from uncorrected straylight, instrument polarization sensitivity, and additional common unknown fitting residuals (Bak et al., 2017a). For the current V04 TEMPO retrievals, we have specifically implemented the soft calibration to mitigate radiometric biases, along with wavelength shift and squeeze fitting on a pixel-to-pixel basis. In addition, the offsets from uncorrected straylight and the 2^{nd}-order polynomial fitting for the surface reflectance were implemented. The detailed methodologies for these specific corrections are described in the following subsections.

3.2.1. TEMPO Measurements

The initial public release of the TEMPO V04 product is based on a UV-only retrieval, in order to optimize the UV-only retrieval algorithm before incorporating the VIS channel into the retrieval. Implementation of the VIS channel requires additional work, including proper treatment of surface reflectivity and mitigation of spectral discontinuities between the UV and VIS channels (Natraj et al., 2011; Zoogman et al., 2017). Accordingly, the retrieval has been optimized to use the spectral range 308-340 nm, which includes most of the tropospheric ozone information in the UV band. Measurements below 308 nm have poor SNR, can contain larger errors, and therefore are not used in the current version. But shorter wavelengths will be added in a future version after improving radiometric calibration. Furthermore, joint UV/visible retrievals are planned to be implemented in a future version with an algorithm and input optimization. The exact spectral range is subject to optimization to deal with issues of calibration, interferences, and/or inadequate modeling.

Normalized radiance, the ratio of measured radiance to measured solar irradiance in L1B data, is used in the ozone profile retrievals. This normalization effectively cancels multiplicative systematic errors originating from common optics between radiance and irradiance (i.e., except

for the transmissive diffuser plate used in measuring solar irradiance). Random measurement noise in both radiance and irradiance is used to define measurement errors initially. The measurement vector is mainly defined as the logarithm of normalized radiance with adjustment due to other parameters not handled in radiative transfer models. So, the measurement vector before adjustment Y_m is:

$$Y_m = ln(\frac{I}{I_0}) \tag{3.9}$$

where I is the radiance and I_0 is the solar irradiance. Correspondingly, the measurement random error of Y_m, i.e., E_m, is the root sum squares of the relative random errors of both radiance and irradiance:

$$E_m = \sqrt{E_i^2 + E_{i0}^2} \tag{3.10}$$

where E_i and E_{i0} are the relative random error (or reciprocal of SNR) in radiance and irradiance, respectively. To minimize random error from solar irradiance and time-dependent systematic error from the diffuser plate, the mean solar irradiance over a certain period may be considered over the weekly measured solar irradiance, if necessary, in the future.

For spatial co-adding, we co-added 4 pixels across-track (i.e., in the N/S direction) to speed up processing. Note that co-adding 4 pixels (resulting in a spatial footprint of approximately 8.0 × 4.75 km^2) still meets the required baseline spatial resolution of < 60 km^2 specified in the Program Level Requirement Appendix (PLRA). When spatial pixels are co-added, radiances are averaged, and viewing geometry is also properly co-added (not simply averaged) for the co-added pixel as if the co-added pixel is directly viewed by the instrument. Irradiances are averaged across-track. The relative random errors would ideally decrease with the square root of the number of co-added pixels (N_c and N_{c0} for radiance and irradiance, respectively), assuming that the averaging introduces no additional error. This assumption may not be strictly valid, however, because differences in wavelength grids among the co-added cross-track pixels, as well as among the along-track pixels included in the average, can introduce additional uncertainties due to thermally induced shifts and scene inhomogeneity (Voors et al., 2006; Noël et al., 2012; Bak et al., 2019b). However, because we only co-added 4 pixels for TEMPO retrievals, the differences in wavelength registration among them are extremely small. In addition, the radiometric errors introduced by this spatial averaging are strictly at the sub-percent level (< 0.2%) and are therefore negligible compared to the significant improvement in the signal-to-noise ratio (Bak et al., 2019b; Liu et al., 2010a).

In practice, we often cannot fit the measurements to the measurement random precision, especially when measurements are co-added due to unknown pseudo-random errors from calibration, forward model simulation, and/or additional adjustment. To avoid the overfitting of measurements, we often have to relax the measurement random errors by introducing a floor noise E_{fl}:

$$E'_m = \max(E_m, E_{fl}) \tag{3.11}$$

Floor noise can be set for different spectral regions. Currently, it is set to 0.15% for all. We tested floor noise values of 0.40%, 0.20%, and 0.15%. As the floor noise was reduced, the total DFS increased from 1.19 to 1.51 and 1.70, indicating enhanced retrieval sensitivity. However, the estimated precision degraded at the same time, the total ozone precision changed from 1.41 dobson unit (DU) to 1.47 DU and 1.49 DU, while the tropospheric ozone precision changed from 2.10 DU to 2.84 DU and 3.03 DU. Based on these results, we selected 0.15% as a practical compromise between maximizing the information content from the satellite measurements and maintaining acceptable retrieval precision. The settings for these floor noises are subject to change to optimize them in future updates. Although using floor noise can stabilize retrievals, it can also reduce the amount of information retrievable from the measurements. The measurement covariance matrix S_y is constructed from E'_m by assuming it as a diagonal matrix, i.e., the off-diagonal elements are set to zero, which means that the measurement errors are assumed to be uncorrelated. Its diagonal elements (one for each wavelength) are the squares of the relative measurement random errors.

3.2.2. Wavelength Calibration

Wavelength calibration is optionally performed for fitting windows in the UV and VIS bands prior to the main ozone retrieval spectral fitting using the well-established cross-correlation technique (Chance, 1998; Liu et al., 2005, 2010a, 2015; Cai et al., 2012; Sun et al., 2017; Bak,et al , 2019b). The ILS parameters and wavelength shifts are determined by nonlinear least-squares fitting of the measured irradiance spectrum to the simulated spectrum using a high-resolution solar reference spectrum. The newly developed high-resolution Total and Spectral Solar Irradiance Sensor (TSIS-1) Hybrid Solar Reference Spectrum (HSRS) (Coddington et al., 2021; Bak et al., 2021b) is chosen over our previous one by Chance & Kurucz (2010), because the radiometric uncertainties of TSIS-1 HSRS are below ~1%, which is much smaller than those from the previous spectrum. Note that this HSRS reference is also used for the convolution of simulated high-resolution radiance to TEMPO resolution and, when necessary, for undersampling correction, which accounts for spectral fitting errors caused by the discrete detector sampling of an instrument line shape that is not fully resolved by the measurement grid. The simulated spectrum I_{0s} can be generically described by the following equation:

$$I_{0s}(\lambda) = \frac{A \int I_{0,hr}(\lambda' + \Delta\lambda)\, s_\lambda d\lambda'}{\int s_\lambda \, d\lambda'} \times P_s^m(\lambda) + P_b^m(\lambda) \tag{3.12}$$

where $I_{o,hr}$ is the high-resolution reference spectrum, s_λ is the ILS, A is the scaling parameter, and $\lambda' + \Delta\lambda$ indicates the process of wavelength calibration/registration (e.g., typically a constant shift, shift and squeeze, or polynomial). P_s^m and P_b^m are the scaling and baseline mth-order polynomials:

$$P^m(\lambda) = \sum_{i=0}^{m} P_i(\lambda - \lambda_{avg})^i \tag{3.13}$$

where P_i represents the respective polynomial coefficients. These two polynomials are not required to be included simultaneously, and their polynomial orders can be different. If the scaling polynomial is included in the fitting, A is fixed to be 1. The ILS is fitted as a generic super-Gaussian function (Beirle et al., 2017), also used in the parameterization of the pre-launch TEMPO ILS:

$$s_\lambda = \exp\left(-\left|\frac{\Delta\lambda}{w + sgn(\Delta\lambda)a_w}\right|^k\right) \tag{3.14}$$

where w is the half-width at 1/e intensity, k is the shape parameter, and a_w is the asymmetric parameter, $\Delta\lambda$ is the wavelength distance from the center of the ILS function, and $sgn()$ is the sign function used to define the two sides of the ILS. If $k = 2$, ILS is a standard Gaussian function, and if $k > 2$, it becomes a flat-top function. If $a_w = 0$, then ILS is symmetric. From the pre-launch ILS, k is closer to 4 in the UV band, and closer to 2.5–3 in the visible band, a_w is closer to 0 as it is quite symmetric. Also, at $k = 2$, w is 0.6 of the ILS FWHM. We determine a single ILS function for each retrieval fitting window and for each cross-track position of the CCD array. The ILS and shift parameters are saved for each cross-track position and applied to all retrievals of that position.

As a default option, we are fitting the ILS with w and k only by fixing a_w to be 0 and applying a constant wavelength shift for each fitting window, with the shift determined from the wavelength calibration using TEMPO measurements. The retrieval also has the option of using the pre-launch ILS instead of a derived ILS. In this case, either the wavelength calibration is skipped or performed, but with the ILS parameters fixed to the average pre-launch parameters over the fitting window. Using real TEMPO data, we optimized the wavelength and ILS calibration options.

However, ILS and shift parameters in radiance could deviate from those derived from solar spectra due to the sensitivity to scene heterogeneity, differences in stray light between radiance and irradiance, and intra-orbit instrumental changes. These might cause some spectral structures in the radiance fitting if not taken into account. Shift parameters between radiance and irradiance, and between radiance and ozone cross sections, have been included in the main spectral fitting on a pixel-to-pixel basis since the initial GOME ozone profile retrieval algorithm. Recently, to account for additional ILS changes from pixel to pixel, we have implemented these spectral errors from ILS parameters as Pseudo Absorbers (PAs), which are derived through the ILS linearization as:

$$\frac{\partial I}{\partial p} = \int I_h \frac{\partial s}{\partial p} d\lambda' \tag{3.14}$$

where $p = w$, k, and a_w represent the specific ILS parameters (i.e., slit width, shape factor, and asymmetry, respectively), and I_h is the simulated high-resolution radiance. These PAs are iteratively adjusted with a zero-order scaling parameter. The description and evaluation of this implementation for OMI ozone profile retrievals is detailed in Bak et al. (2019b). As

demonstrated in Bak et al. (2019b) for OMI ozone profile retrievals, accounting for these slit function errors slightly smooths spikes in the fitting residuals. Comparisons with ozonesondes demonstrate noticeable improvements, particularly in reducing systematic biases in the tropics and midlatitudes (mean tropospheric column ozone biases reduced from -1.4~0.7 to 0.0~0.4 DU) and in reducing the standard deviations of tropospheric ozone column differences at high latitudes.

3.2.3. Radiometric Calibration

In our TEMPO V04 retrievals, an empirical radiometric correction, referred to as soft calibration, is applied to reduce systematic measurement biases in the wavelength range of 293–350 nm for ozone fitting and around 347 nm for the initial surface albedo and cloud fitting. The correction follows the soft calibration concept developed for the OMI algorithm, but the current V04 TEMPO implementation includes dependence only on wavelength and cross-track position. In contrast to the version 2 OMI retrievals, a time-dependent term to account for instrumental degradation is not included at present for TEMPO, although such an extension may be considered in future versions if warranted. Figure 3.2 shows the recently derived TEMPO soft calibration spectra as a function of cross-track (xtrack) position and wavelength for the case of June 2025. It illustrates the existence of some large systematic residuals between measured and simulated radiances. These soft calibration spectra are derived as a systematic component of differences between measured and simulated radiances at tropical clear-sky pixels in summer, where the forward-model calculations are more accurate, to attribute the residuals to measurement biases.

The accuracy of soft calibration depends on the input ozone profiles used in the simulation. For TEMPO, we initially expected to derive soft calibration spectra using GEOS-CF forecast data as inputs to the ozone profile retrievals. However, in the V04 TEMPO retrieval, we utilized the TB climatology (Bak et al., 2013b) for ozone profiles and the National Centers for Environmental Prediction (NCEP) Final (FNL) operational global analysis data for meteorological inputs to derive the TEMPO soft calibration spectra. This decision was made because the high temporal variability captured by the GEOS-CF model, while physically realistic, introduced instability into the derivation of soft calibration spectra. For the purpose of soft calibration, which aims to isolate systematic instrumental biases, a stable reference is preferable to a highly dynamic one. The TB climatology provides a statistically stable mean state that effectively minimizes the influence of transient geophysical variability, thereby yielding more robust and consistent soft calibration results. To smooth out the impact of daily ozone variabilities, 9 scans of measurements in June 2025 are used in deriving the soft spectra after screening out outliers of extreme viewing geometries (SZA and VZA > 60°), cloudy pixels (cloud fraction > 0.2), bright surfaces (surface albedo > 0.1), and abnormally large values of average residuals.

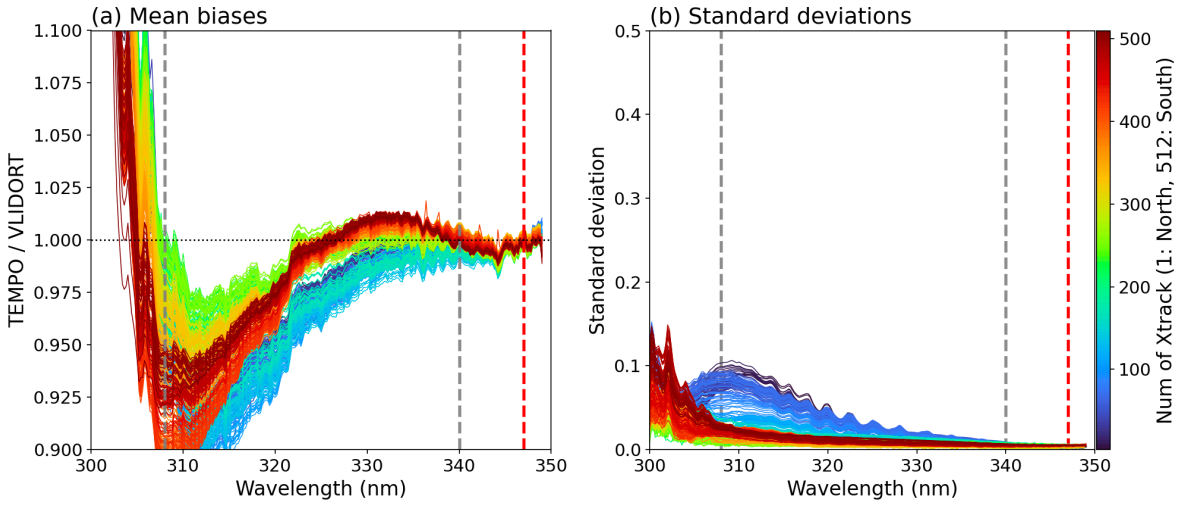

Figure 3.2. *(a) The Soft calibration spectra derived for TEMPO V04 L1b products in June 2025 represent the initial systematic biases between measured and simulated spectra. (b) The standard deviations of the systematic biases represent the uncertainties of soft calibration spectra. The grey and red dashed lines represent the TEMPO spectral fitting window range and 347 nm for initial surface albedo and cloud fitting, respectively.*

The top panel of Figure 3.3 shows the TEMPO retrievals without soft calibrations. The figure illustrates the critical importance of radiometric soft calibration in the TEMPO O3PROF retrieval algorithm. It compares the retrieval results for total column ozone (TCO), tropospheric column ozone (TrCO), and spectral fitting residuals before and after applying soft calibration. The analysis, grounded in methodologies established by previous studies, demonstrates that soft calibration is a prerequisite for improving retrieval accuracy by mitigating residual radiometric calibration in L1B data, thereby ensuring physically valid ozone distributions.

Without soft calibration, the fitting residuals are significantly high (predominantly > 0.2%, shown in red in Figure 3.3(c)). This indicates a substantial discrepancy between the measured and simulated normalized radiances from the TEMPO observation and the Vector Linearized Discrete Ordinate Radiative Transfer (VLIDORT) simulation. In the context of UV backscatter retrievals (e.g., OMI and GEMS), such residuals typically originated from systematic instrument errors, including wavelength shifts, silt function uncertainties, and stray light, rather than geophysical variability. Upon applying soft calibration, the fitting residuals are drastically reduced to below 0.1% (shown in blue in Figure 3.3(f)). This confirms that the soft calibration has successfully mitigated the systematic biases. The most significant improvement is observed in the tropospheric ozone distribution. The previously overestimated values have been corrected to a physically realistic range, revealing detailed spatial patterns consistent with expected climatological distributions.

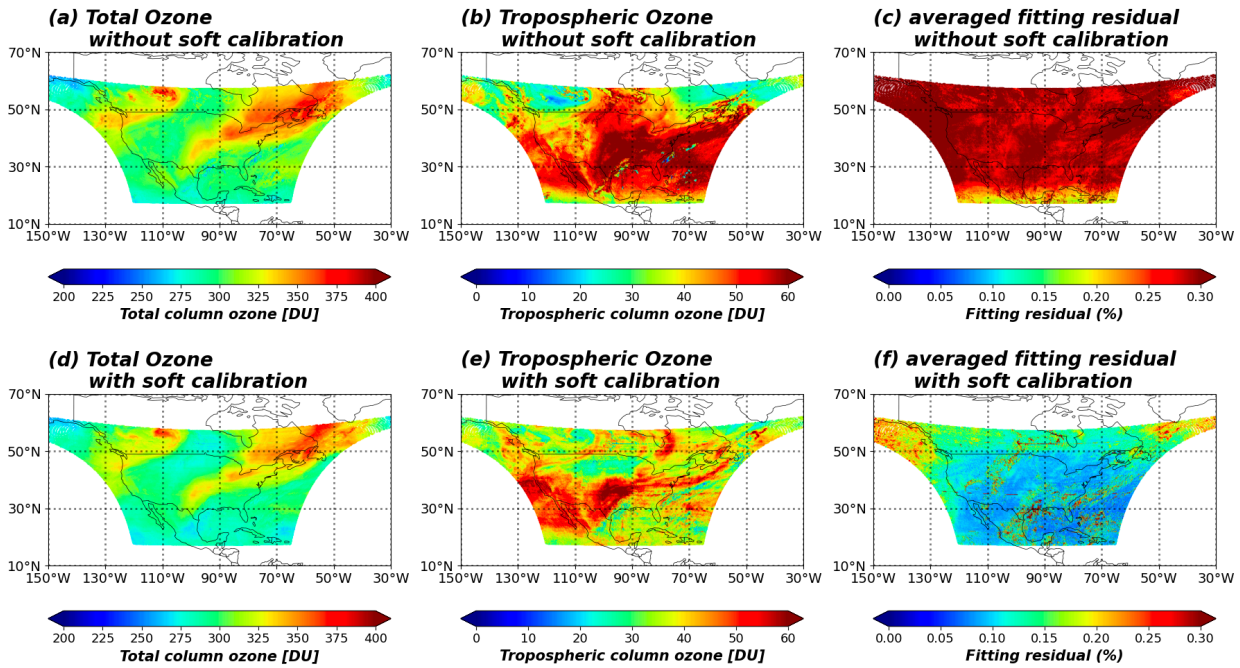

Figure 3.3. *The distribution of total column ozone (a and d) in dobson unit (DU), tropospheric column ozone (b and e) in DU, and spectral fitting residuals (c and f) in percentage (%) from TEMPO measurements on 26 July 2024. The top (a, b, and c) and bottom (d, e, and f) panels show TEMPO retrieval results without and with soft calibration, respectively.*

3.2.4. Solar Irradiance Correction

One of the significant sources of radiometric error identified in TEMPO L1B data is associated with the measured solar irradiance, similar to issues observed in its sister instrument, GEMS. These errors arise primarily because the Bidirectional Transmission Distribution Function (BTDF) of the TEMPO transmissive diffuser plates exhibits a complex dependence on solar viewing geometry that was not fully characterized during pre-launch testing. Post-launch calibration analyses (e.g., Chong et al., 2026) have confirmed that radiometric biases exist and vary seasonally with solar geometry. In the V04 L1B product, however, these biases have been substantially mitigated. Therefore, this specific correction is not applied to the TEMPO O3PROF retrieval algorithm. Nevertheless, the following approach remains available for potential use in future versions, should additional correction of solar irradiance-related biases become necessary:

a. The measured TEMPO solar irradiance would be calibrated against a high-resolution solar reference spectrum. This reference would then be convolved with the derived ILS parameters and wavelength calibration results, as described in Equation (3.12), following Liu et al. (2015):

$$I'_{0m}(\lambda) = (I_{0m}(\lambda) - P_b^m(\lambda))/(A \times P_s^m(\lambda)) \quad (3.16)$$

where I'_{0m} is the corrected TEMPO solar irradiance.

b. Alternatively, a static or time-averaged solar irradiance spectrum could be derived and used. In the future implementation, a high-resolution solar reference (e.g., TSIS-1) would likely be

preferred to minimize the impact of day-to-day diffuser-related artifacts and to ensure consistency with the radiometric calibration described in Sec. 3.2.3.

3.2.5. Common Mode Calibration

From OMI and OMPS ozone profile retrieval studies (Bak et al., 2017, 2024), it has been found that the soft calibration is less effective in eliminating systematic residuals at high SZAs. This implies the existence of a spectral dependence of the radiometric calibration on the signal represented by SZA, which is not accounted for in the soft calibration dependent only on the CCD dimension. The common mode spectrum of the fitting residuals is physically treated as a pseudo absorber, along with a scaling coefficient that is iteratively fitted in each of the fitting windows. Therefore, the scene-dependent radiometric errors could be partly accounted for. This kind of correction is originally used in the spectral fitting process, where a common mode residual could be calculated online for each measurement orbit. However, additional online calculation is not practical for the time-consuming, optimal estimation-based ozone profile retrieval process. Therefore, in our OMI version 2 retrievals, we derive time-independent common mode spectra by averaging three days of fitting residuals (July 13th–15th, 2005) over five solar zenith angle regimes (0°–40°, 40°–60°, 60°–70°, 70°–80°, and 80°–85°) for each cross-track position. Applying Common Mode Correction (CMC) reduces the dependence of fitting residuals on both SZA and cross-track pixels, thereby improving global fitting accuracy. For TEMPO, we initially expected to derive and implement similar CMC spectra from operational TEMPO retrievals. However, this correction was not applied in the current V04 release. Validation comparisons against ground-based lidar measurements demonstrated that the current algorithm provides promising ozone profile results even without the CMC. Therefore, the implementation of CMC has been deferred and is currently reserved as a potential enhancement for future versions to further minimize residual dependencies if necessary.

3.2.6. Other Correction

Several additional corrections will be tested with real TEMPO measurements before applying the CMC in the future version. This includes additional corrections to the effect of instrument linear polarization sensitivity (LPS), undersampling correction, and offset correction. GEMS trace gas retrievals have been shown to be subject to LPS-related errors, causing latitude-dependent biases because the radiance is not corrected for LPS (Choi et al., 2024; Lee et al., 2024). Including LPS as a pseudo-absorber has been shown to effectively reduce the LPS-related errors on trace gas retrievals (Lee et al., 2024). We will test the option of including LPS as a pseudo-absorber to determine whether it improves retrievals. If measurements are not Nyquist-sampled, resampling the radiance and irradiance spectra onto a common wavelength grid can introduce spectral undersampling errors (Chance et al., 2005). Chance (1998) developed an undersampling correction technique using the high-resolution solar reference spectrum to compensate for more than 90% of systematic fitting residuals in GOME BrO fitting. For TEMPO, the retrieval accounts for small wavelength misregistration between the radiance and solar irradiance spectra by applying a wavelength shift correction during spectral fitting. The spectral fitting also

includes a Ring effect term, together with wavelength-dependent polarization correction terms across the fitting window. Additional fitting terms are included to account for residual straylight and dark-current contributions in radiance spectra. The retrieval algorithm additionally allows for optional treatment of slit-function differences between radiance and solar irradiance spectra, degradation-related effects, and residual straylight dark-current contributions in both irradiance and radiance, although these terms are not necessarily activated in the current configuration. The details in Section 3.4.2.

3.3. Forward Model Simulation and Inputs

The forward model is described in detail in Section 3.3.1. It includes the Radiative Transfer Model (RTM) with a look-up table (LUT) of corrections. Forward model inputs include trace gas cross sections (Section 3.3.2), atmospheric model and trace gas profiles (Section 3.3.3), additional climatological ozone profile a priori and a priori errors (Section 3.3.4), surface reflectance (Section 3.3.5), and cloud and surface treatments (Section 3.3.6).

3.3.1. Radiative Transfer Calculation

The RTM is needed for calculating the forward model component, such as top-of-the-atmosphere radiances and Jacobians of radiances with respect to the atmospheric and surface parameters K. The radiance calculation is performed for a Rayleigh atmosphere (no aerosols), with Lambertian Equivalent Reflectivity (LER) assumed for both the surface and clouds. Partial cloudy scenes are modelled based on the Mixed Lambert Equivalent Reflectivity (MLER) model: the scene consists of a clear-sky scene of surface reflectivity R_s, surface pressure P_s, a cloudy scene of cloud reflectivity R_c (typically 0.8), and effective cloud top pressure or cloud optical centroid pressure P_{ctp} based on the Independent Pixel Approximation (IPA):

$$I = I_{clr}(R_s, P_s) \times (1 - f_c) + I_{cld}(R_c, P_{ctp}) \times f_c \tag{3.17}$$

where I, I_{clr} and I_{cld} are the overall, clear, and cloudy scene radiances, respectively, and f_c is the effective cloud fraction.

This RTM, used in the retrievals, is based on the VLIDORT model (Spurr, 2006, 2008). VLIDORT uses the discrete ordinate method to solve the radiative transfer (RT) equation in a multi-layer multi-scattering atmosphere. This code is fully linearized with respect to the specified variables, and the Jacobians are then computed analytically with a single RT call. Both the attenuation of incoming solar radiation and the attenuation of outgoing radiation are treated for a curved atmosphere using the pseudo-spherical assumption. In the discrete ordinate method of VLIDORT, the term “streams” refers to the number of discrete angular directions used to represent the radiation field. In general, increasing the number of streams improves the accuracy of the RT calculation, at the expense of greater computational cost.
VLIDORT calculates the Stokes parameters *I*, *Q*, *U*, and *V* in full-polarization mode or vector-mode, where *I* is the total intensity, *Q* and *U* are the linearly polarized components, and *V* is the circularly polarized component of the radiation field.

However, the vector-mode calculation increases the computational time by a factor of 9 to 16 (if only *I*, *Q*, and *U* are calculated) compared to the scalar-mode calculation (which calculates only *I*), and can introduce significant radiance errors, especially in the UV wavelength range.

To accelerate RT calculations, we use the PCA-based VLIDORT (v2.8) model (Spurr et al., 2013; Bak et al., 2021a) to simulate radiances and weighting functions combined with LUTs to correct for RT approximations, which has been implemented in OMI version 2 ozone profile retrievals (Bak et al., 2021a). To accurately account for the TEMPO spectral resolution, radiances must first be simulated at a much finer spectral resolution (~0.01–0.05 nm) than the native measurement sampling (~0.2 nm), and then convolved with the TEMPO's spectral response. To reduce the computational burden, a few wavelengths are effectively selected (λ_c) for running the RTM and then interpolated to regular high-resolution grids (λ_h) with the radiance adjustment for errors caused by the spectral resolutions as follows:

$$I(\lambda_h) = I(\lambda_c) + \sum_{l=1}^{N} \frac{\partial I(\lambda_c)}{\partial \Delta_l^{gas}} \left(\Delta_l^{gas}(\lambda_h) - \Delta_l^{gas}(\lambda_c) \right) + \frac{\partial I(\lambda_c)}{\partial \Delta_l^{ray}} \left(\Delta_l^{ray}(\lambda_h) - \Delta_l^{ray}(\lambda_c) \right) \quad (3.18)$$

here, $\frac{\partial I}{\partial \Delta_l}$ represents the radiance Jacobian with respect to the optical depth perturbation in layer l ($l = 1$ to N). In Equation (3.18), the gas Jacobian accounts for changes in radiance caused by the spectral variation of the gaseous absorption optical depth, while the ray Jacobian accounts for changes caused by the spectral variation of the molecular Rayleigh-scattering optical depth. These two terms are treated separately because gas absorption and Rayleigh scattering exhibit different wavelength dependences. In the VLIDORT v2.8 forward model, both λ_c and λ_h are set to be finer than intervals previously used. In the PCA approach, multiple-scattering (MS) calculations are performed only for a few representative optical states derived using Empirical Orthogonal Function (EOF) analysis of spectrally binned inherent optical properties that exhibit substantial spectral redundancy. In OMI versions 1 and 2 and in TEMPO forward models, polarization is not part of the direct RT simulation of the entire spectrum, but a polarization correction is applied to speed up the RT. In the OMI version 1 forward model, vector calculations are also performed at 14 wavelengths to compute the scalar-versus-vector differences at those wavelengths, which are then interpolated to all wavelengths. However, residual polarization errors persist, along with other approximation errors arising from using 4 half-streams in the discrete-ordinate radiative transfer calculation (i.e., 4 quadrature directions per hemisphere, or 8 streams in total) and coarse vertical layers (~2.5 km thick). In the OMI version 2 forward model, the number of half-streams was reduced from 4 to 2, thereby improving computational efficiency by approximately a factor of 2. To mitigate increasing RT approximation errors, a LUT-based correction is applied to account for differences in RT variables due to different numbers of streams (2 vs. 6) and vertical layers (24 vs. 72), as well as neglecting the polarization effect. As verified in a companion paper, these updates improve retrieval speed by a factor of ~3.3 and retrieval accuracy (Bak et al., 2021a). In the TEMPO V04 forward model, we adopted the same general strategy as in the OMI version 2 forward model,

except that the LUT-based correction for RT approximation errors was not applied. Table 3.1 summarizes the details of the PCA-VLIDORT model simulation, and Table 3.2 lists the dimensions and nodes of the LUTs for corrections. In the V04 TEMPO O3PROF, the forward model calculations are performed using PCA-VLIDORT with the number of N_{stream} set to 4. In addition, scalar radiative transfer calculations are used for most wavelengths to improve computational efficiency. To account for polarization effects, additional scalar and vector calculations are performed at 9 representative wavelengths distributed across the 308-340 nm, which is the TEMPO V04 spectral fitting window, and the resulting vector-minus-scalar differences are spectrally interpolated to provide a polarization correction across the full spectral fitting window. We created a LUT for the additional correction, but it will be implemented in the future version to further improve forward-model accuracy. For the LUT generating, the SZA and VZA nodes were selected separately because the radiative-transfer correction does not exhibit identical dependence on solar and viewing geometry.

Table 3.1. *TEMPO O3PROF forward model simulation details.*

Option	TEMPO RT implementation details
λ_c	305 nm: 0.3 nm; 540 nm: 0.1 nm | 0.2 nm
λ_h	0.05 nm in UV and 0.02 nm in VIS
RT model	PCA-based VLIDORT v2.8
N_{stream}*	4
N_{stokes}	scalar except for vector and scalar calculation at 9 wavelengths
N_{layer}	24
RT correction	LUT-based correction (will be implemented in the future version)

*The N_{stream} in VLIDORT means half stream.

Table 3.2. *TEMPO O3PROF look-up table of radiative transfer corrections.*

Parameter	# of Nodes	Nodes
Ozone Profiles	22	Tropical latitudes: L200, L250, L300, L350 Middle latitudes: M200, M250, M300, M350, M400, M450, M500, M550 Polar latitudes: H100, H150, H200, H250, H300, H350, H400, H450, H500, H550
Wavelength	788	290.6–742.9 nm, irregular/optimized grid
Solar Zenith Angle (degree)	12	0.01, 16, 31, 44, 55, 64, 71, 76.5, 80.5, 83.5, 86, 88
Viewing Zenith Angle (degree)	13	0.01, 15, 30, 43, 53, 61, 67, 72, 76, 80, 84, 86, 88
Surface/cloud pressure (hPa)	11	100, 200, 300, 400, 500, 600, 700, 800, 900, 1013.25, 1050

Layers (hPa)	25	0.087, 0.17, 0.35, 0.49, 0.70, 0.99, 1.40, 1.98, 2.80, 3.96, 5.60, 7.92, 11.19, 15.83, 22.39, 31.66, 44.78, 63.33, 89.56, 126.66, 179.12, 253.31, 358.24, 506.63, 716.48, 1050

Rotational Raman Scattering (RRS), commonly referred to as the Ring effect, modifies the depth of solar Fraunhofer lines in measured backscattered radiances and therefore needs to be accounted for in the spectral fitting. The Ring spectrum is not calculated directly within the RT calculation; instead, it is obtained directly by modeling the first-order RRS of the direct radiance (Sioris & Evans, 2000) for the same atmosphere used in the retrieval, accounting for the RRS dependence on viewing geometry, atmospheric ozone, and temperature profiles. The Ring spectrum is updated only during the retrieval iteration when the total ozone changes by 20 DU. Because multiple scattering is not considered in this Ring model, a scaling parameter or a 1st-order polynomial is fitted during retrieval for each fitting window to account for greater variation due to multiple scattering. We use the actual TEMPO solar irradiances rather than the high-resolution reference spectrum, without additional convolution to match the TEMPO resolution.

3.3.2. Trace Gas Reference Spectra

Table 3.3 lists the reference spectra for trace gases used and tested in the TEMPO ozone profile algorithm, along with the high-resolution solar reference, Ring effect, and undersampling spectra.

Table 3.3. *Reference spectra to be used and tested in the TEMPO O3PROF algorithm.*

Species/Component	Details
High-resolution solar reference	TSIS-1 HSRS (Coddington et al., 2021)
O_3	BW (Birk & Wagner, 2021)
O_2-O_2	(Finkenzeller & Volkamer, 2022), not used in V04
NO_2	220K (Vandaele et al., 1998)
BrO	228 K (Wilmouth et al., 1999)
HCHO	300 K (Chance & Orphal, 2011)
SO_2	SCIAMACHY FM (Bogumil et al., 2003), not used in V04

For ozone, in the TEMPO retrievals, the recent Birk and Wagner (BW) (Birk & Wagner, 2021) ozone cross-section dataset is used, as Bak et al. (2020) demonstrated the improved performance of ozone profile retrievals through comparison with ozonesonde measurements over the previously recommended Brion, Daumont, and Malicet (BDM) dataset (Daumont et al., 1992; Brion et al., 1993, 1998; Malicet et al., 1995; Liu et al., 2007, 2013). Retrievals with the BW datasets show a significant reduction in standard deviations, by up to 15% in the lower stratosphere and upper troposphere, where atmospheric temperatures are lower than ~200 K, compared to using the BDM dataset. This is due to improved temperature coverage from 193 K to 293 K and better parameterized quadratic temperature-dependent coefficients in the BW

dataset. However, it only covers the spectral range of 244–346 nm and does not cover the visible. Given that the current V04 TEMPO retrievals utilize only the UV spectral window, we have adopted the BW dataset for this version. For future updates incorporating the visible band, we plan to evaluate the optimal cross-section strategy, such as testing the combined use of the BW dataset in the UV and the BDM dataset in the visible (potentially with scaling corrections to match the BW data). For either dataset, we will use the parameterized temperature-dependent quadratic coefficients (C0, C1, C2):

$$C = C_0 + C_1(T - 273.15) + C_2(T - 273.15)^2 \quad (3.19)$$

where T is the atmospheric temperature in K. In the visible, the BDM cross section is measured only at two temperatures at wavelengths up to 650 nm, so only C_0 and C_1 are derived and C_2 is essentially 0, and at wavelengths above ~650 nm, it is measured only at 1 temperature, so C_1 and C_2 are both 0.

For other trace gases included in the current V04 UV retrievals, we utilize the following cross-section datasets. For the oxygen dimer (O_2-O_2), we use the dataset from Finkenzeller & Volkamer (2022). For minor trace gases, we apply cross-sections at fixed temperatures, NO_2 at 220 K (Vandaele et al., 1998), BrO at 228 K (Wilmouth et al., 1999), HCHO at 300 K (Chance & Orphal, 2011), and SO_2 from the SCIAMACHY pre-Flight Model (FM) (Bogumil et al., 2003). The inclusion of other potential absorbers (e.g., liquid water, water vapor from High-Resolution Transmission Molecular Absorption Database (HITRAN) 2020) and modifications to the current cross-section selections (e.g., combining datasets for broader spectral coverage) are reserved for future updates. For O_2-O_2, we have previously selected Thalman & Volkamer (2013) as it covers both UV and visible (323–654 nm) and provides temperature dependence. There is an improved dataset from the same group that only covers 300–500 nm (Finkenzeller & Volkamer, 2022). We will combine the latter one below 500 nm and the former one above 500 nm, possibly with some scaling adjustment for the future version with VIS wavelengths. Temperature- and pressure-dependent O_2 and H_2O cross sections are from the HITRAN 2020 database (Gordon et al., 2022).

Table 3.4. *Ancillary data used in the TEMPO O3PROF algorithm.*

Data type	Details
Cloud-top pressure	TEMPO L2 CLDO4 product (O_2-O_2 fitting)
Cloud fraction	Initially derived from ~347 nm, further fitted
Ozone profiles	GEOS-CF (Keller et al., 2021; Knowland et al., 2022a) v2 + Tropopause-based Climatology (Bak et al., 2013b)
Other trace gases	Chemical model-based climatology
Temperature profiles	GEOS-CF v2
Surface albedo	Geometry-dependent surface Lambertian Equivalent Reflectivity (GLER) (Qin et al., 2019; Fasnacht et al., 2019) v2
Snow/ice fraction	TEMPO L1B, Interactive Multisensor Snow & Ice Mapping System (IMS)

Terrain height	TEMPO L1B, Global Multi-resolution Terrain Elevation Data (GMTED) 2010 (Danielson & Gesch, 2011) with 30 arcs
Surface pressure	GEOS-CF v2 with correction
Tropopause pressure	GEOS-CF v2
Aerosols	None, implicitly included in the cloud and albedo treatment

3.3.3. Atmospheric Model and Trace Gas Profiles

TEMPO O3PROF retrieval algorithm mainly uses atmospheric trace gas profiles from the chemical model-based dataset and meteorological parameters from the GEOS-CF model (Keller et al., 2021; Knowland et al., 2022a) as shown in Table 3.4. GEOS-CF is a chemical forecasting system produced by NASA's Global Modeling and Assimilation Office (GMAO). The GEOS-CF system performs near-real-time hindcasts and 5-day forecasts of atmospheric composition using the offline GEOS-Chem chemical transport model (http://geos-chem.org) integrated into the GMAO GEOS system. Gases and aerosols are simulated at the same resolution as the meteorological fields, with hourly output at a cubed-sphere grid at c360 horizontal resolution, where c360 denotes 360 grid cells along each edge of a cubed-sphere face, corresponding to a nominal horizontal resolution of approximately 25×25 km^2 and 72 vertical layers from the surface to 0.01 hPa. The global five-day forecast is produced daily, beginning at 12:00Z.

Details on the GEOS-CF model and performance of the version 1.0 tropospheric simulation can be found in Keller et al. (2021). The stratospheric component of the GEOS-CF is described and evaluated in Knowland et al., 2022a. While the GEOS-CF forecasting system was at version 1.2 as of December 2022, version 2.0 became available on 4 August 2025 and was implemented as the main GEOS-CF product for the V04 TEMPO product in October 2025. Its current implementation, emission inventories, and outputs are described in Knowland et al. (2022b). GEOS-CF version 1.2 uses gas-phase chemistry simulated with GEOS-Chem version 12.0.1. GEOS-Chem includes detailed HO_x-NO_x-BrO_x-VOC-O_3 tropospheric chemistry (Bey et al., 2001; Parrella et al., 2012; Mao et al., 2013; Marais et al., 2016; Sherwen et al., 2016) of 250 chemical species with coupled stratospheric-tropospheric chemistry (Eastham et al., 2014), with emissions provided by the Harmonized Emissions Component (HEMCO) (Keller et al., 2014). Anthropogenic emissions are from the Hemispheric Transport of Air Pollution (HTAP) (Janssens-Maenhout et al., 2015) and Reanalysis of the Tropospheric chemical composition (RETRO) (Schultz et al., 2008) inventories with updated scaling factors applied (van der Gon et al., 2011; Oda et al., 2018; Liu et al., 2018). Biomass burning emissions are determined from the Quick Fire Emission Database (QFED) (Darmenov & da Silva, 2015) using Moderate Resolution Imaging Spectroradiometer (MODIS) fire data. Biogenic emissions are determined using Model of Emissions of Gases and Aerosols from Nature (MEGAN) v2.1 (Guenther et al., 2012). Additional emissions are included for lightning (Murray et al., 2012), soil (Hudman et al., 2012), NO_x, volcanic SO_2 (Carn, 2019), sea salt aerosols, oceanic emissions of dimethyl sulfide,

acetone, acetaldehyde, iodine, and soil dust (further details can be found in Knowland et al. (2022b)). The hindcast (replay), which serves as the starting point for the next forecast, is run each day to force the meteorology to the GEOS Forward Processing for Instrument Teams (FP-IT) assimilated product (Lucchesi, 2013). GEOS-Chem stratospheric ozone is nudged to ozone from the GEOS FP, which was constrained by assimilating ozone measurements from satellites (Wargan et al., 2015). GEOS FP-IT aerosols are also constrained by satellite measurements of aerosol optical depth (Buchard et al., 2017). GEOS-CF does not currently assimilate any other trace gas or aerosol observations.

In order to minimize large data transfers and archiving, the GMAO produces a smaller TEMPO-specific GEOS-CF product for use in the TEMPO processing pipeline. Upon completion of the daily GEOS-CF forecast, the TEMPO processing pipeline downloads the most recent GEOS-CF TEMPO forecasts for the next day. The GEOS-CF TEMPO product is limited in geography to longitudes -180° to 0° and latitudes 0° to +90°, and contains the vertical mixing ratios of a select trace gases detectable in the UV/VIS (O_3, NO_2, HCHO, SO_2, H_2O, BrO, $C_2H_2O_2$, HNO_2, and Iodine monoxide (IO)) and relevant meteorology (surface pressure, temperature profile, eastward and northward winds components at 2 m above the surface, tropopause pressure, and boundary layer height).

If, for some reason, GEOS-CF forecasts become unavailable, the TEMPO processing pipeline defaults to using a climatology. The climatology consists of monthly averages of the same GEOS-CF trace gases and meteorological parameters provided in the GEOS-CF TEMPO daily forecasts. These monthly averages were created using a long-term dataset of GEOS-CF hindcasts from January 2018 to May 2021 (meteorological fields) and January 2020 to May 2021 (chemical fields). As the GEOS-CF model is updated, the climatologies are expected to be updated. The atmospheric profiles and parameters used in the TEMPO processing are obtained by linearly interpolating between the two monthly climatologies nearest to the observation date. Although this fallback is not expected to be the standard mode of operation, replacing forecast fields with monthly climatological fields can introduce discontinuities in the L2 product because the climatology does not capture the day-to-day and hour-to-hour variability represented by the forecast fields.

GEOS-CF data are interpolated to the TEMPO pixel center. The use of an atmospheric model with larger spatial resolution than the satellite observations can lead to significant errors in the Air Mass Factor (AMF) in areas of inhomogeneous terrain elevation (Boersma et al., 2004; Zhou et al., 2009). In order to correct for terrain height inhomogeneities over the model footprint, the interpolated GEOS-CF surface pressure P_m is further corrected using the effective terrain height z_s for each satellite ground pixel as determined from the GMTED2010 high resolution digital elevation model (DEM) (Danielson & Gesch, 2011). The corrected surface pressure P_s is approximately derived using pressure altitude from:

$$P_s = P_m + 1013.25 \times (10^{-\frac{z_s}{16}} - 10^{-\frac{z_m}{16}}) \quad (3.20)$$

where z_m is the terrain altitude from the model. The GEOS-CF model layers are defined on a terrain-following hybrid sigma-pressure coordinate with 72 model layers. In this coordinate system, the vertical grid follows the terrain near the surface and gradually transitions to a pure pressure coordinate aloft. The pressure at each layer boundary is determined from the corrected surface pressure, P_s, together with a set of fixed layer-dependent coefficients, a_i and b_i. The bottom boundary of a layer is defined as:

$$P_i = a_i + P_s \cdot b_i \quad (3.21)$$

and with the top of the layer defined as:

$$P_{i+1} = a_{i+1} + P_s \cdot b_{i+1} \quad (3.22)$$

The surface pressure and temperature profiles are used to derive the altitude grid through the hydrostatic equation and to compute air number density profiles (Fu et al., 2013). Trace gas partial column density profiles used in the retrievals are computed from the corresponding mixing ratio profiles. In addition, the GEOS-CF tropopause pressure is used to modify the TEMPO O3PROF calculation pressure grid by replacing the grid level nearest to the tropopause and redistributing the layers between the surface and tropopause in logarithmic pressure space, as described in Section 3.4. This adjustment allows the retrieval grid to better represent variability in tropopause height. The altitude grid is interpolated to the O3PROF calculation grid, and the partial air number density and trace gas column densities are also interpolated to the O3PROF calculation grid using the cumulative density profiles so that the air mass and individual trace gas mass are conserved after the interpolation.

3.3.4. Ozone Profile Climatology

Unlike other minor trace gas profiles, which are completely obtained from chemical model-based climatology data, ozone profiles are combined from GEOS-CF and ozone profile TB climatology, which includes both a priori ozone profiles and a priori error used to constrain and stabilize the retrievals. TEMPO O3PROF algorithm can use three kinds of ozone profile climatologies to define the a priori ozone profile: the Labow, Logan, McPeters (LLM) ozone climatology (McPeters et al., 2007), the McPeters and Labow (ML) ozone climatology (McPeters & Labow, 2012), and the TB ozone climatology (Bak et al., 2013b).

The LLM climatology consists of monthly mean ozone profiles and their standard deviations for 18 10° latitude bands. It was compiled from ozonesonde data (1988–2001) for the troposphere and lower stratosphere, and from Stratospheric Aerosol and Gas Experiment 2 (SAGE 2; 1988–2002) and Upper Atmospheric Research Satellite (UARS) MLS (1991–1999) data for the stratosphere. To construct continuous vertical profiles, sonde and SAGE 2 measurements were merged over 10–18 km, while sonde and MLS measurements were merged over 20–28 km. The ML climatology is an updated version of the LLM climatology, derived from Aura MLS V3.3 (2004–2010) and ozonesonde data (1988–2010). The TB climatology was constructed from ozonesonde ozone and temperature profiles (1983–2008) and extended above the sonde burst

altitude (~35 km) to 0.005 hPa using an existing ozone climatology. This upper extension was taken from the LLM climatology. The monthly averages and their 1σ standard deviations were calculated in 18 10° latitude bins using the ozone profiles relative to the tropopause. So, using the TB climatology also requires an estimate of the tropopause height as an extra parameter in addition to latitude and time.

The a priori error covariance S_a of ozone is taken from the climatological a priori error constructed using various satellite and ozonesonde datasets as described above. The diagonal elements of S_a are the variances of the corresponding elements. The off-diagonal element between layers *i* and *j* is derived by assuming a correlation length l of 6 km:

$$S_a(i,j) = \sqrt{S_a(i,i)S_a(j,j)}\, e^{-\left(\frac{|z_i - z_j|}{l}\right)^2} \tag{3.23}$$

An optimal estimation-based ozone retrieval can be significantly affected by the quality of a priori data, particularly when measurement information is insufficient, especially near the boundary layer or the tropopause, where the vertical resolution of nadir-viewing satellite observations is inherently limited. In the OMI version1 algorithm, the a priori ozone information was taken from the LLM climatology. The OMI version 2 algorithm uses the TB instead. Bak et al. (2013b) demonstrated significant OMI retrieval improvements in comparison with ozonesondes due to a much better representation of the sharp gradients of ozone vertical structures near the tropopause with much smaller a priori error in the extratropics. Figure 3.4 compares tropospheric ozone retrievals on 01 February 2007 with LLM and TB, respectively. The most noticeable difference is identified in the northern region of Eurasia where abnormally high concentrations are retrieved when LLM is used as a priori. This retrieval issue was also mentioned in comparing OMI version 1 with other satellite products, data assimilation, and chemical transport model calculation (Gaudel et al., 2018; Ziemke et al., 2014), showing unexplained large positive biases in TrCO during high-latitude winter. It is clearly seen that the abnormal feature of the retrieved high ozone is closely correlated with the high LLM a priori (Fig. 3.4(b)) resulting from abnormally high tropopause height (Fig. 3.4(c)). LLM can represent the typical vertical profiles whose ozone pause is located at ~8 km over high latitudes during the winter. Therefore, with the presence of the abnormally high tropopause height, the lower stratospheric layers of LLM profiles can be misrepresented as a priori in the upper troposphere, which likely causes large positive biases of OMI version 1 ozone retrievals in the troposphere. However, an ozone profile taken from the TB climatology is re-distributed according to the daily tropopause.

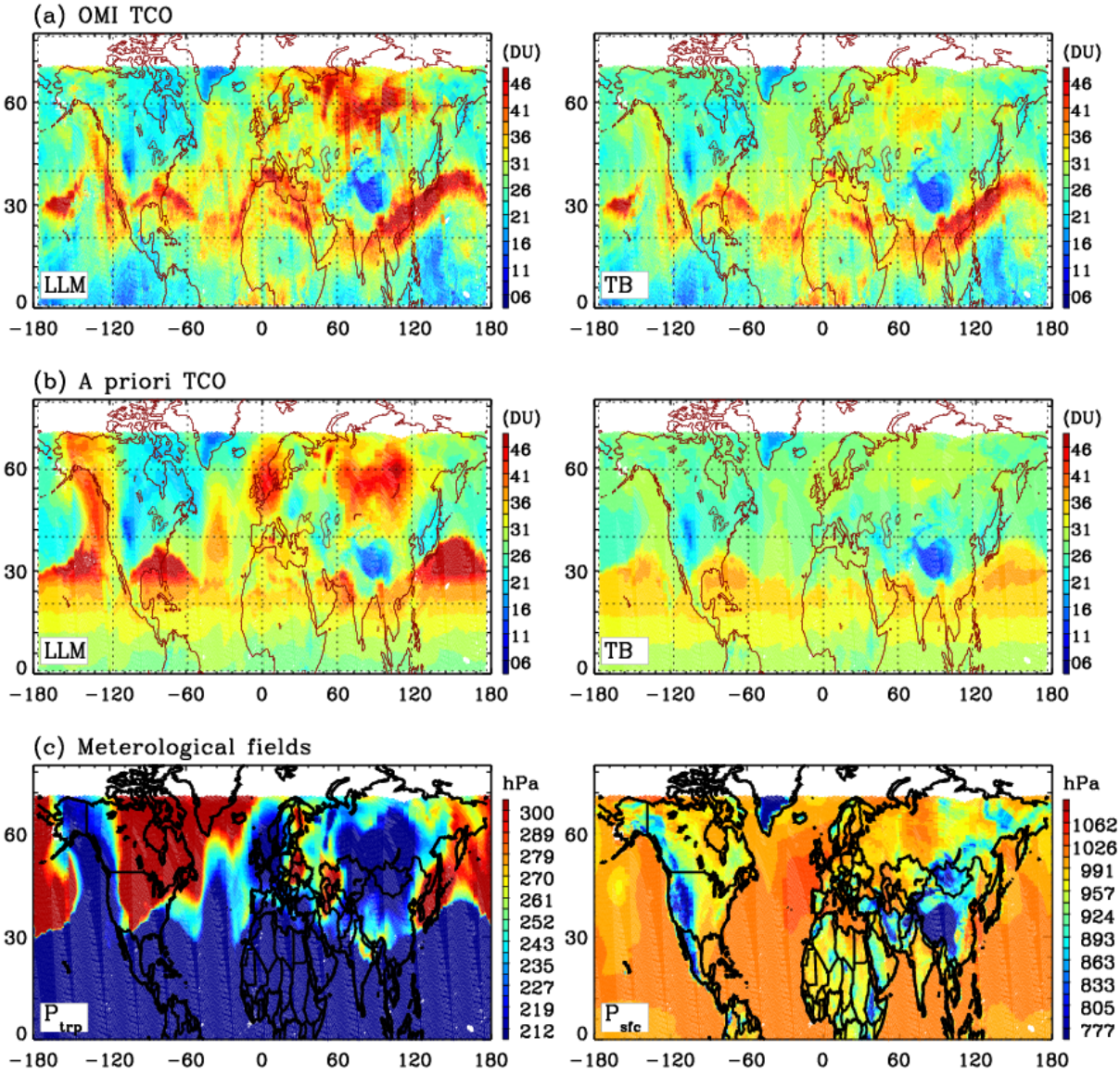

Figure 3.4. *Comparison of (a) OMI tropospheric column ozone (TrCO) and (b) the a priori TrCO taken from the LLM (left) and Tropopause-Based (TB) (right) climatologies, respectively, in the Northern hemisphere on 01 February 2007. (c) tropopause (P_t) and surface (P_s) pressure fields are presented in the bottom panels.*

For implemented this TB climatology in the V04 TEMPO O3PROF retrieval, we tested the integration of GEOS-CF v2 with the TB climatology to optimize the a priori profile using the preliminary V04 TEMPO O3PROF retrievals. As illustrated in Figure 3.5, we evaluated a total of six different a priori profiles. In Figure 3.6, the TEMPO retrieval and its a priori are indicated by the solid and dashed red lines, respectively. For comparison, the Tropospheric Ozone Lidar Network (TOLNet) measurements smoothed with TEMPO averaging kernels and the raw TOLNet data are shown as the solid and dashed black lines, respectively. The shading around each line represents the 1σ standard deviation. In addition, the TOLNet lidars were extended above the troposphere with co-located ozonesonde observations. As shown in Figure 3.6,

comparisons against ground-based TOLNet lidar measurements revealed that the combination that utilizes the TB climatology specifically for the UTLS region and GEOS-CF v2 for the remaining layers demonstrated the highest agreement and lowest biases (in Figure 3.6 for validation results). Based on these findings, this specific combination was adopted for the V04 TEMPO O3PROF algorithm.

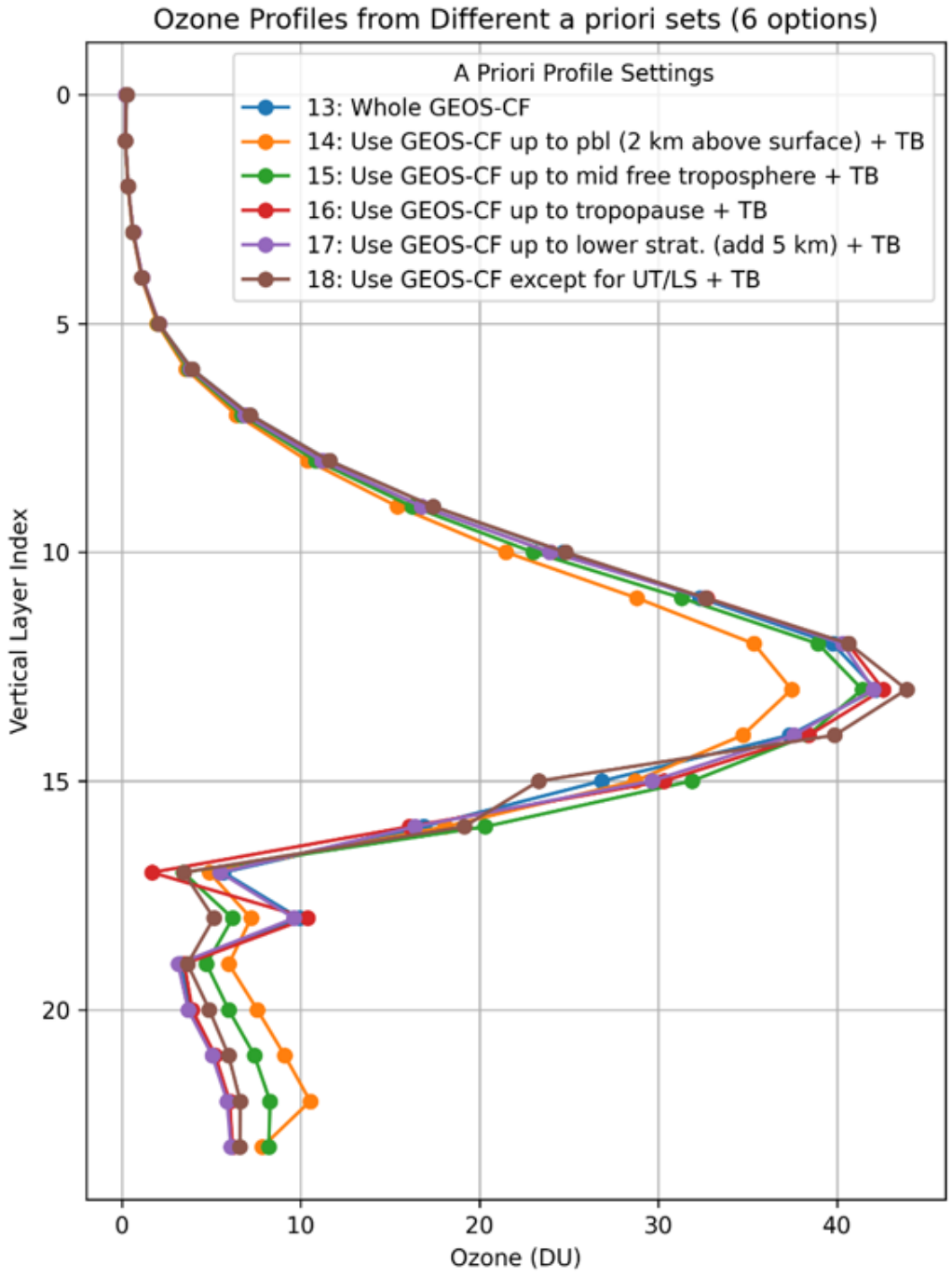

Figure 3.5. *Six combinations of the a priori profiles using GEOS-CF v2 and TB climatology.*

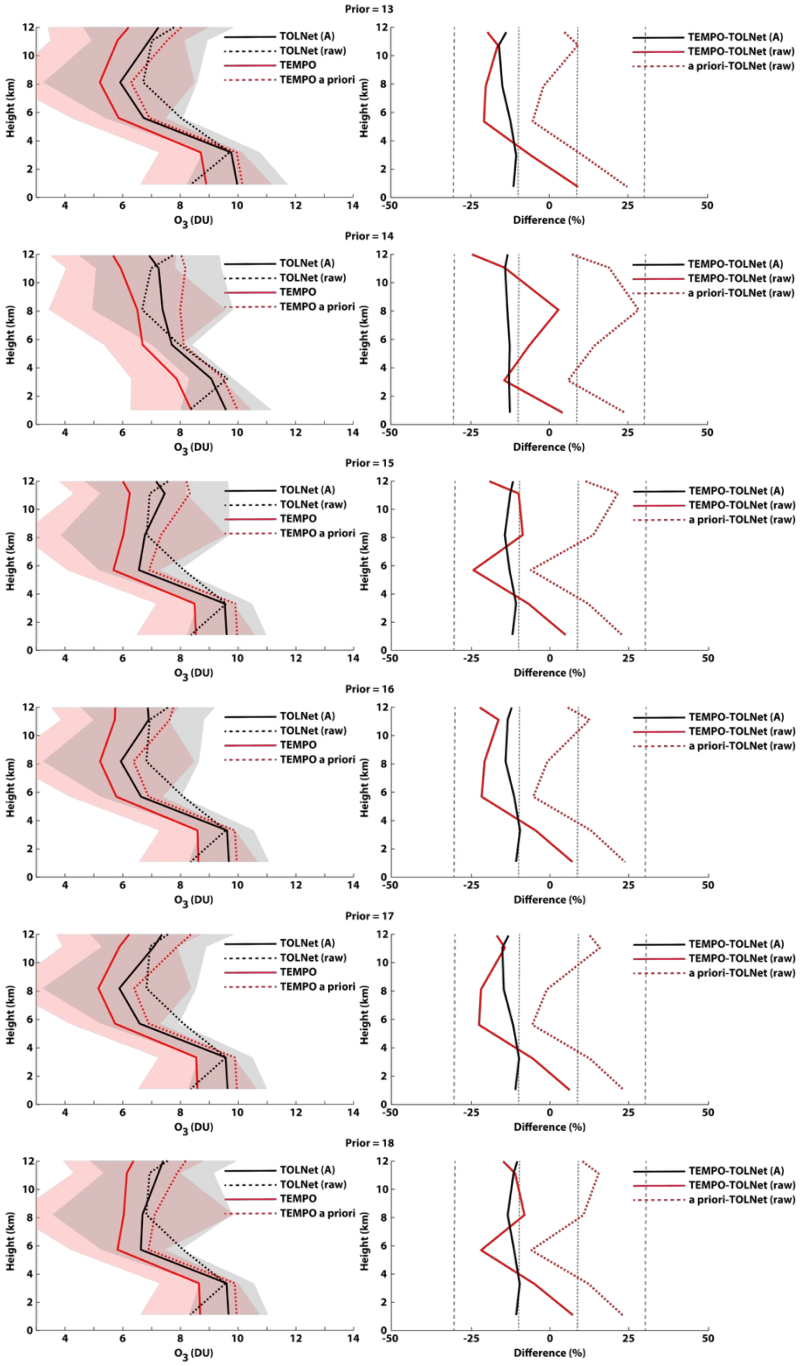

Figure 3.6. *Validation of preliminary TEMPO V04 O3PROF tropospheric retrievals against Tropospheric Ozone Lidar Network (TOLNet) ground-based lidar observations, using six different a priori profiles inputs. TEMPO and TEMPO a priori denote the retrieved TEMPO ozone profile and the corresponding a priori profile used in retrieval, respectively. TOLNet(raw) and TOLNet(A) denote the original ozone profile measured by the TOLNet lidar and the TOLNet profile smoothed with the TEMPO averaging kernels, respectively. Shaded regions indicate the standard deviation of the profiles, representing temporal variability during the matched observation period.*

3.3.5. Surface Reflectance

For each TEMPO observation, an associated Geometry-dependent surface Lambertian Equivalent Reflectivity (GLER) (Fasnacht et al., 2019; Qin et al., 2019) is calculated at a particular wavelength, which differs between land and water. The land/water mask in the L1B data is from the MODIS land/water mask, produced at ~1 km resolution. In addition, over land, L1B data contains yearly updates on land cover classification from the MODIS Land Cover Type product MCD12Q1 using the International Geosphere Biosphere Program (IGBP) type 1 classification scheme that identifies 17 land cover classes with 500 m spatial resolution (Friedl et al., 2002, 2010). This surface cover information might be useful in determining the surface albedo spectrum.

Over land, the GLER value is obtained from two climatologies, one representing snow-free (L_f) and snow-covered (L_s) scenes. Using information from the 1-km Interactive Multisensor Snow and Ice Mapping System (IMS) product (US National Ice Center, 2008), the final GLER value (a_s) is the result of weighting GLERs by the snow fraction s_f:

$$a_s = \left(1 - s_f\right) \cdot L_f + s_f \cdot L_{fs} \tag{3.24}$$

Twenty years (2000–2020) of MODIS Bidirectional Reflectance Distribution Function (BRDF) retrievals were used to generate GLER climatologies. The MCD43C1 (Schaaf & Wang, 2015a) and MCD43C2 (Schaaf & Wang, 2015b) products are used for snow-covered and snow-free scenes, respectively. With the derived BRDF climatologies, a set of monthly GLER LUTs were derived following the approach of Qin et al. (2019). The land GLER LUTs have a resolution of 0.05° × 0.05°, extending from 15°W to 167°W and from 14°N to 73°N. The LUTs represent the diurnal variation of the GLER by storing values at each location every 30 minutes. The final GLER value is obtained by linear interpolation to TEMPO's time of day, month, latitude, and longitude.

Over water, the absence of reliable sea ice BRDF information simplifies the calculation. In this case, a single GLER is derived from a single set of LUTs constructed using the Cox-Munk slope distribution (Cox & Munk, 1954) as described in Fasnacht et al. (2019). The water GLER LUTs are parameterized as a function of the wind speed, the time of the day, and the location. They have a resolution of 1° × 1°, extending from 15°W to 167°W and from 14°N to 73°N.

Both sets of LUTs, land and water, are derived initially at the four MODIS wavelengths over land (469, 555, 645, and 859 nm) and at 8 wavelengths over water (340, 354, 388, 440, 469, 555, 645, and 859 nm). The data is then interpolated to a total of 19 wavelengths (340, 354, 367, 388, 425, 440, 466, 494, 526, 555, 564, 614, 640, 659, 670, 685, 712, 758, and 865 nm) taking advantage of a probabilistic model (factor analysis) that estimates the BRDF at a given wavelength using BRDF observations from the four MODIS BRDF bands (Chan Miller et al., 2019). This model is trained on reflectance spectra from the United States Geological Survey (USGS) spectral library (Kokaly et al., 2017) and SCIAMACHY LER (Tilstra et al., 2017) at a

much coarser resolution of ~5° × 5° following the methodology described by Zoogman et al. (2016). The BRDF at a given wavelength is given by:

$$a_{s0}(\lambda) = a_{sm}(\lambda) + \sum_{i=0}^{m} c_i a_{fi}(\lambda) \tag{3.25}$$

where $a_{fi}(\lambda)$ is the derived i^{th} factor or EOF from training, and $a_{sm}(\lambda)$ is the mean surface albedo spectrum at each coarser grid cell. c_i is the derived coefficient for each factor or EOF for the high-resolution grid cell (e.g., 0.05° × 0.05°) by matching the GLER values at those 4 MODIS wavelengths over land and at the 8 wavelengths over water. The GLER is pre-generated at 15/11 other wavelengths over land/water: 340, 354, 367, 388, 425, 440, 494, 526, 564, 614, 640, 670, 685, 712, and 758 nm.

In the V04 TEMPO O3PROF retrieval, we implemented this GLER and evaluated its performance by comparing it with the OMI LER (OMLER) climatology. As illustrated in Figure 3.7, the comparison shows that the choice of surface reflectance database has minimal impact on the retrieved ozone amounts, and that the total and tropospheric ozone columns differ only slightly between the GLER- and OMLER-based retrievals, with negligible biases. However, the average fitting residuals are lower with GLER than with OMLER (right-bottom panel in Figure 3.7).

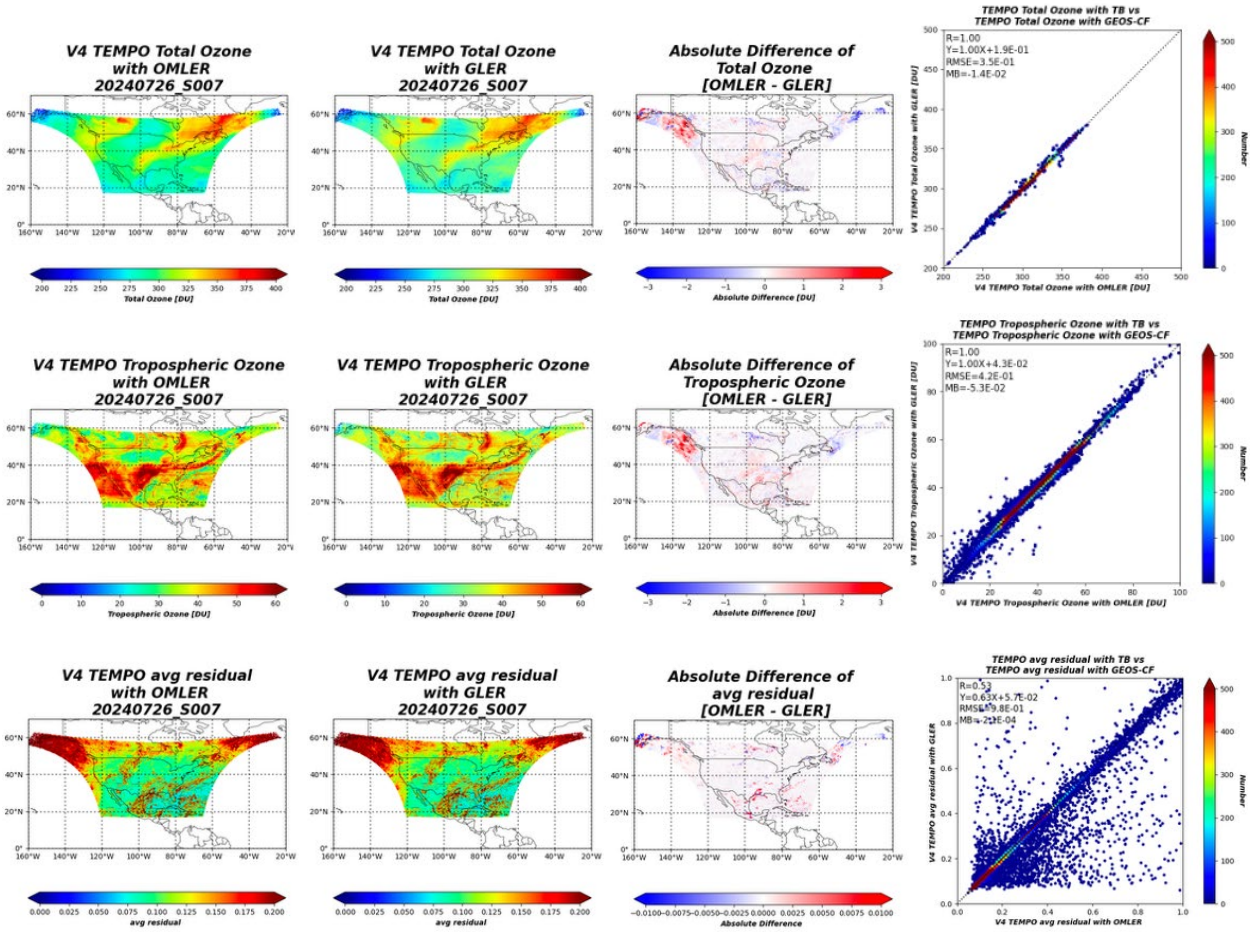

Figure 3.7. *Comparison of TEMPO V04 O3PROF retrievals using OMLER and GLER for the scan S007 on July 26, 2024. The rows represent (top) total ozone column, (middle) tropospheric ozone column, and (bottom) average fitting residuals. Each row displays the spatial distribution for OMLER (first column), GLER (second column), their absolute difference (OMLER - GLER) (third column), and a scatter plot comparison (fourth column). The comparison shows that, although the choice of surface reflectance database has a negligible impact on retrieved ozone amounts, the use of GLER reduces fitting residuals.*

3.3.6. Cloud and Surface Treatments

Cloud information is taken from the cloud Optical Centroid Pressure (OCP) of the TEMPO L2 CLDO4 product (O_2-O_2 fitting) (Wang et al., 2025). Only cloud pressure values that meet all recommended quality flags are used. For the V04 TEMPO O3PROF retrieval, pixels without good-quality OCP values are filled in using spatial interpolation on a granule basis. An initial f_c is determined from the radiance at ~347 nm using Equation (3.26), where the measured radiance I_m, the clear-sky radiance $I_{clr}(R_s, P_s)$, and the cloudy radiance $I_{cld}\left(R_c, P_{ctp}\right)$ are specified from the known surface albedo (R_s), surface pressure (P_s), cloud albedo (R_c), and cloud optical centroid pressure (P_{ctp}):

$$f_c = (I_m - I_{clr}(R_s, P_s))/(I_{cld}\left(R_c, P_{ctp}\right) - I_{clr}(R_s, P_s)) \quad (3.26)$$

If f_c is ≤ 0.01, it is set to 0.00. We assume no cloud is present and use the LER model to derive the clear-scene reflectivity R_s. If f_c is ≥ 0.99, it is set to 1.00. We assume a 100% cloud cover and then derive cloud reflectivity R_c using the LER model. This modification ensures that both clear- and cloudy-sky radiance are calculated in the RT calculation when we start the main retrieval. The f_c is then further iteratively fitted in the retrievals. Currently, a single f_c is fitted for the entire retrieval. We plan to add the capability to fit f_c for each fitting window separately, as the effective cloud fraction, by definition, should not be the same for different spectral regions due to wavelength-dependent surface albedo and Rayleigh scattering.

In the UV, surface albedo is initialized from the GLER climatology at 340 nm, and a zero or 1st-order surface albedo polynomial is fitted for the UV channel. But in the V04 TEMPO O3PROF retrieval algorithm, we applied a 2nd-order surface albedo polynomial to fit the UV channel based on the fitting residual. In the visible, a surface albedo spectrum $a_{s0}(\lambda)$ is also initialized from the GLER climatology from the probabilistic model following Equation 3.25. A selected number (≤ 4) of surface albedo EOFs a_{fi} is further fitted with coefficients c_i in the retrievals:

$$a_s(\lambda) = a_{so}(\lambda) + \sum_{i=0}^{m} c_i a_{fi}(\lambda) \quad (3.27)$$

In the presence of a water or snow/ice surface, the USGS water/snow surface albedo spectrum is included as one of the EOF spectra. If the surface is completely covered by water or snow, then the water/snow albedo spectrum is considered as the only surface albedo EOF.

In our retrievals, aerosols are not explicitly modeled in the retrievals. Surface pressure is taken from modeled meteorological data, and cloud parameters are prescribed from the TEMPO L2

CLDO4 product; however, residual uncertainties in these inputs, together with small biases in the absolute TEMPO radiances, may still introduce spectral mismatches. We thus fit wavelength-dependent surface albedo values (a second-order polynomial for UV) and effective cloud fractions as tuning parameters to partially or implicitly account for aerosol scattering effects.

3.4. Additional Retrieval Scheme and Implementation Details

3.4.1. Retrieval Grid

The ozone profile is retrieved in partial ozone columns (DU) for a 24-layer (25 edge levels) atmosphere. The vertical grid varies from pixel to pixel in the lower stratosphere and troposphere but is fixed at higher altitudes. The 25 pressure levels are first defined as $P_i = 2^{-i/2}$ atm for i = 0 to 23, where 1 atm = 1013.25 hPa. The uppermost level is set to $P_{24} = 2^{-13.5}$ atm (0.087 hPa), with ozone and air number density above this level included in the top layer. This pressure grid is then modified: the thermal tropopause pressure from GEOS-CF data is used to replace the level closest to it, the first level (I = 0) is set to the corrected GEOS-CF surface pressure, and the second level is set to 2 km above the surface, and layers between that level and the tropopause are distributed equally in logarithmic pressure. Each layer is thus ~2.50 km thick, except for the top layer. There are 4 to 7 layers in the troposphere, depending on the height of the tropopause. The primary purpose of adjusting the model layering to tropopause height is to derive Stratospheric Column Ozone (SCO) and TrCO, and their corresponding errors, which can be integrated from the profile and error covariance matrix. The actual value of the tropopause pressure has a negligible effect on the retrieved TCO and on values at layers not affected by the layer adjustment. TrCO and SCO can be re-calculated from the retrievals through interpolation if a different tropopause is available. The setting of the first layer to 2 km above the surface is to retrieve 0–2 km ozone, one of the TEMPO requirements for ozone. So that 0–2 km ozone column above the surface and its corresponding errors are stored in the first layer of the retrieved profile and error profiles.

Note that the vertical grid used for RT calculation (or the RT grid) is different from the retrieval grid. The algorithm allows each retrieval layer to be divided into a specified number of finer RT layers, which is typically set to 1. In this case, the RT layering is nearly identical to the retrieval layering except for the top retrieval layer, which is further divided into three RT layers because of its much greater thickness. As a result, the RT grid contains 26 layers. Jacobians computed on the RT grid are then vertically integrated and mapped onto the retrieval grid before the inversion.

3.4.2. State Vector and A Priori

Table 3.5 shows the typical list of fitting variables. The retrieval variables in the state vector include ozone partial columns at 24 layers, other trace gases (O_2-O_2, NO_2, BrO, HCHO, and SO_2), surface albedo terms (typically a first-order polynomial in UV but we used second order polynomial in UV for V04 TEMPO retrieval), cloud fraction, a scaling parameter for the Ring effect in each fitting window, radiance/irradiance wavelength shift, radiance/O_3 cross section

wavelength shift, slit width pseudo absorber coefficient for each fitting window, shape factor pseudo absorber coefficient for each fitting window, common mode scaling parameter, degradation factor in UV, offset in UV, and fitting of undersampling spectra. Some of the fitting variables are optional. Most other minor trace gases are not required, except O_2, O_4, and H_2O. Undersampling correction is not needed as TEMPO has ~3 samples per FWHM, similar to OMI. The simultaneous fitting of surface albedo and effective cloud fraction with ozone greatly improves the fitting residuals because these parameters account for aerosol, cloud, and surface pressure effects, but reduces the DFS for tropospheric ozone, which is significantly correlated with higher-order surface albedo terms. The Ring spectrum fitting is added in the UV, but it is probably less important in the visible due to much smaller Rayleigh scattering. The UV degradation and offset parameters are optional and intended to account for possible degradation, inconsistent radiometric calibration between the UV and visible bands, or offsets due to uncorrected stray light for future update.

Table 3.5. *List of fitting variables, a priori values, and a priori errors. All the variables other than ozone are assumed to be uncorrelated with each other.*

Fitting variables	# Variables	A priori	A priori error
Ozone at each layer (used in V04)	24	Climatology & GEOS-CF	Climatology
O_2-O_2 scaling (not used in V04)	1	derived	30%
O_2 scaling (not used in V04)	1	derived	30%
H_2O scaling (not used in V04)	1	GEOS-CF	100%
NO_2 scaling (used in V04)	1	GEOS-CF	100%
BrO scaling (used in V04)	1	GEOS-CF	100%
HCHO scaling (used in V04)	1	GEOS-CF	100%
SO_2 scaling (not used in V04)	1	GEOS-CF	100%
Surface albedo (UV) (used in V04)	1	GLER Climatology	0.05
2^{nd}-order λ-dependent term in surface albedo (UV) (used in V04)	1	0.0	0.01
Surface albedo EOF scaling (not used in V04)	4	0.0	2
Cloud fraction (used in V04)	1	derived @ 347 nm	0.05
Ring scaling parameters (used in V04)	2 (1/window)	-2.0	1
Radiance/irradiance wavelength shifts (used in V04)	2 (1/window)	0.0	0.02 nm
Radiance/O_3 cross section wavelength shifts (used in V04)	2 (1/window)	0.0	0.02 nm
Slit width PA coefficient	2 (1/window)	0.0	0.3 nm

(used in V04)			
Shape factor PA coefficient (not used in V04)	2 (1/window)	0.0	0.3
Degradation factor (not used in V04)	1 (UV)	0.0	0.1
Common mode scaling parameter (not used in V04)	2 (1/window)	0.0	1.0
Offset (used in V04)	1 (UV)	0.0	0.03
Undersampling (not used in V04)	2	1.0	0.5

In TEMPO V04 retrievals, the selection of these parameters is based on their impact on fitting residuals, their cross-correlation with ozone variables, and comparisons with correlative ozone observations. We included variables that can reduce fitting residuals and improve comparisons with correlative observations, while avoiding variables strongly correlated with ozone. Of all the non-ozone parameters, the degradation correction parameter, the higher-order wavelength-dependent surface albedo term in UV, and the radiance/O_3 wavelength shifts can have noticeable correlation with ozone variables.

Table 3.5 also shows the corresponding a priori values and a priori errors. The a priori values and errors other than ozone are empirically chosen. We can derive an a priori vector X_a from the ozone profile climatology as described in Section 3.2.4. As variables other than ozone are assumed to be uncorrelated with each other, we can easily extend the a priori covariance matrix S_a diagonal to other than ozone elements after constructing the a priori ozone covariance matrix according to Equation 3.23. Most of the initial values of the state vectors are the same as the a priori values except for ozone variables, which can be the same or different, as discussed in Section 3.2.4 when the retrieval starts.

3.4.3. Measurement and Simulation Adjustment

Not all variables can be directly modeled in the radiative transfer simulation. Some variables are adjusted from the measurement Y_m as mentioned in Section 3.2, as follows:

$$Y'_m(\lambda) = \ln\left(\frac{\frac{I(\lambda)}{\phi_{soft}(\lambda)} + \alpha_{off}\phi_{off}(\lambda)}{I_0(\lambda+\Delta\lambda)\times\exp(\alpha_d) + \sum_{j=1}^{2}\alpha_{us,j}\phi_{us,j}(\lambda)}\right)\times(1-\alpha_{cmc}\phi_{cmc}(\lambda)) \qquad (3.28)$$

where $\Delta\lambda$ indicates wavelength shifts between radiance and irradiance, α_d is the degradation correction (typically in UV channel), $\phi_{us,j}$ is the undersampling spectrum and $\alpha_{us,j}$ corresponding fitted undersampling coefficient, ϕ_{soft} is the soft calibration spectrum, ϕ_{off} is the offset spectrum (e.g., related to radiometric calibration coefficient) and α_{off} is the fitted offset parameter, ϕ_{cmc} is the CMC spectrum (in each fitting window) and α_{cmc} the corresponding fitted CMC parameter. Instrument LPS-induced errors in radiances may also be additionally fitted in Equation 3.28. For other variables, it makes more sense to adjust them from the simulated normalized radiance Y_s as follows:

$$Y_s'(\lambda) = Y_s(\lambda)\exp\left(-\sum_j \alpha_{tr,j}\phi_{tr,j}(\lambda) - \sum_j \alpha_{ring,j}\phi_{ring,j}(\lambda) - \sum_j \alpha_{o3shi,j}\phi_{o3shi,j}(\lambda) - \sum_j \alpha_{ils,j}\phi_{ils,j}(\lambda)\right) \quad (3.29)$$

where ϕ_{tr} is the trace gas not directly modeled in the RTM, α_{tr} is the corresponding fitted trace gas column, ϕ_{ring} is the ring spectrum, α_{ring} is the corresponding Ring scaling parameter, ϕ_{o3shi} is the radiance/O_3 cross section wavelength shift spectrum, α_{o3shi} is the corresponding fitted radiance/O_3 wavelength shift, ϕ_{ils} is the ILS pseudo absorption spectrum (for slit width w, shape k, asymmetric factor a_w), and α_{ils} is the corresponding fitted slit parameters. Strictly speaking, all these parameters can also be reversely adjusted in Equation 3.28 without really affecting the retrievals, because we are essentially fitting the difference between adjusted measurement and simulation ΔY. In addition to accounting for these variables, we also need to calculate their corresponding Jacobians. Most of the Jacobians are derived analytically from Equations 3.28 and 3.29 and from the VLIDORT (Spurr, 2006). Jacobians for parameters whose derivatives are not straightforward to express analytically are calculated using finite-difference perturbations, as commonly done in retrieval applications (e.g., Sun et al., 2022). The measurement error is still E_m' as shown in Equation 3.11, and the measurement error covariance matrix S_y is assumed to be a diagonal matrix with diagonal elements equal to the square of the measurement error.

3.4.4. Retrieval Convergence and Termination

With the adjusted measurement and simulation, the measurement error covariance matrix (S_y), the calculated Jacobians (or *K* matrix), and the a priori and its covariance matrix (S_a) defined, the optimal estimation-based inversion can be performed according to Equation 3.5 to update the state vector. Optimal estimation is performed iteratively, so a convergence criterion must be set to stop the iteration once the algorithm finds the optimal solution. The convergence criterion is based on the magnitude of the state vector update and the change in the cost function (Equation 3.4), and convergence is reached when the relative change in the state vector, fit residuals, or cost function is less than a defined threshold. Retrievals are considered to have converged when the change in retrieved ozone at each layer is less than 1%, or when the relative change in the cost function is less than 1%, either between successive iterations or between the values evaluated before and after the state vector update. The retrieval exits if the number of iterations reaches 10 and the retrieval is flagged as "not converged". In addition, the retrieval exits if it encounters a "NaN" value in the adjusted measurement/simulation or calculated Jacobian, and the retrieval is flagged. Furthermore, if the retrieved ozone or trace gases or surface albedo becomes negative, which can cause problems in the RTM simulation as VLIDORT cannot handle negative surface albedo or total negative absorption, the algorithm will set the ozone/albedo to some small positive values and adjust radiance with respect to the albedo and ozone change using Jacobians so that the retrieval can proceed and may sometimes change the presence of negative values. Retrievals with negative ozone values at the last iteration are

flagged. With UV only, retrievals typically converge within 3–5 iterations. When a previous retrieval is used as the initial value for the next adjacent pixel, most retrievals can converge in 2–3 iterations. In UV/VIS retrievals (future version), the weaker ozone absorption signal and surface interference from surface albedo can make the inversion less stable and more difficult to converge. Since the convergence criteria for UV/VIS retrievals are subject to future updates, detailed discussion is beyond the scope of this V04 UV-only ATBD.

3.4.5. Retrieval Error Estimation

As we noted in Section 3.1, the OE provides useful tools for error analysis. The optimal estimate $\hat{X}$ can be regained from a posteriori solution of Equation 3.5 with $X_i = X_{true}$.

$$\hat{X} \approx X_{true} + (A - I)(X_{true} - X_a) + G\varepsilon \tag{3.30}$$

The second term of Equation 3.30 is the smoothing error. The last term is the retrieval random error. The retrieval output includes estimates of total error (or solution error), smoothing error, and random error of the state vector, which are the square root of the diagonal elements of $\widehat{S}$, S_n, and S_s, respectively. The retrieval output also includes the retrieval random error covariance matrix S_n and retrieval A. S_s can be re-calculated via Equation 3.8. Retrieval errors due to systematic measurement error, forward-model simulation error, or uncertainty in forward-model inputs can be estimated using optimal estimation theory. So, the systematic retrieval error, and thus the retrieval accuracy, are not included in the retrieval output as measurement/forward model simulation error, and forward model parameter error is not readily available. In practice, one relies on independent validation to assess the retrieval bias or accuracy using correlative measurements (e.g., TOLNet, ozonesonde).

3.4.6. Retrieval Splitting and Merging

Because the retrieval requires online RT calculations at many spectral points within the spectral fitting window, the computation is highly time-consuming. To reduce processing time, each granule is divided into multiple blocks. Even with 4 pixels coadded in the N/S direction, the granule still contains 512 cross-track (xtrack) positions. It is therefore split into ~50 blocks, each containing about ~1200 coadded pixels, and each block is processed on a separate CPU core. The results from all blocks are then merged after processing.

3.5. TEMPO Ozone Profile Product

3.5.1. Retrieval Output

The TEMPO V04 L2 O3PROF product file is saved in NetCDF-4 format. In addition to geolocation fields, it contains the retrieved ozone profile in terms of partial ozone columns including 0–2 km ozone column above the surface, a priori ozone profile and a prior error, total, stratospheric, and tropospheric ozone columns (TCO, SCO, and TrCO), other retrieved auxiliary parameters, random-noise and total retrieval errors for all of the retrieved and derived quantities, the retrieval AKs for the ozone profile, and the correlation matrix. Each file contains a single granule (~6 mins) of data. In each granule, TEMPO measurements cover approximately ~130 East/West (E/W) mirror steps with a North/South (N/S) cross-track of ~2K spatial pixels but

coadded to 512 cross-track pixels in the O3PROF product. Therefore, the spatial resolution at the center of the field of regard is 4.75 km (E/W) × 8 km (N/S).

The partial ozone column $O_{3,i}$ can be converted to mean mixing ratio $O_{3,i}$ (ppbv) at each layer using the following formula (assuming ozone is well mixed in that layer):

$$O_{3,i}(\text{ppbv}) = 1.251 \times O_{3,i}(\text{DU})/(P_{i+1} - P_i) \times 1013.25 \times (\frac{\text{R}}{\text{R} + Z_{mid,i}})^2 \quad (3.31)$$

where P_{i+1}, P_i are the pressures in hPa at the two levels bounding layer i, R is the radius of the earth assuming sphericity, and $Z_{mid,i}$ is the center altitude of that layer. This formula is accurate to better than 1%. Similarly, TrCO can be converted to the mean mixing ratio by using the tropopause and surface pressure. Using mixing ratios has certain advantages over using TrCOs by reducing variability due solely to variations in the vertical grid from the tropopause and surface pressure, and in the 0–2 km layer above the surface.

3.5.2. Retrieval Quality Control and Diagnostics

The retrieval output contains several variables that describe retrieval quality control and diagnostics, in addition to the retrieval AK and derived DFS for the total, stratospheric, and tropospheric columns, or at each layer, and retrieval error estimates. These quality control variables are: (a) Retrieval exit status, (b) Fitting root mean square of the residuals with respect to measurement error (fitting RMS) or to radiance (fitting RES) for both fitting windows and for each fitting window, (c) effective cloud fraction and cloud-top pressure, (d) solar zenith angle. Table 3.6 shows all the possible values of return exit status and corresponding meanings. Retrieval with exit status ≥ 1 and ≤ 99 is recommended. To quantify the performance of the spectral fitting, the mean fitting residuals are calculated for UV spectral fitting window in the form of the root mean square of spectral differences relative to the measured spectrum and the measured error as follows:

$$RES = \sqrt{\frac{1}{N}\sum_1^N ((I_m - I_s)/I_m)^2} \times 100\ (\%) \quad (3.32)$$

$$RMS = \sqrt{\frac{1}{N}\sum_1^N ((Y'_m - Y'_s)/E'_m)^2} \quad (3.33)$$

where I_m and I_s represent measured radiance or normalized radiance spectrum, and simulated radiance or normalized radiance spectrum, respectively, with N the number of wavelengths in the UV spectral fitting window. The *RES* of the fitting residuals needs to be better than 0.2–0.3% in the Huggins band (310–340 nm) for reliable retrievals of tropospheric ozone. The *RMS* describes both the quality of the spectral fit and the stability of regularization. The ideal RMS value is 1. If RMS $\ll$ 1, either the fitting is overfitted or the measurement errors are overestimated. On the other hand, if RMS $\gg$ 1, either the fitting is underfitted or the measurement errors are underestimated.

Table 3.6. *Definition of retrieval exit status.*

Value	Description
-6	Failure due to NaN values
-5	Failure due to RTM simulation and I/F spectrum calculation
-4	Failure due to Ring simulation
-3	Failure due to out of bounds of state vectors
-2	Failure due to setting atmospheric profile
-1	Failure due to setting cloud fraction or surface albedo
0	Not converge[+]
1	Fit residuals changes less than convergence constant[*]
2	Cost function changes less than convergence constant
3	1+2
4	Ozone parameters change less than convergence constant
5	1 +4
6	2+4
7	4+2+1
+100	Negative ozone values occur in the last iteration

[+]The number of allowed iterations is 10.
[*]Relative threshold value (10^{-2}) is used.

3.6. Algorithm Input Variables

Table 3.7. *Algorithm input variables*

Name	Long Name	Unit
product/cloud_fraction	effective cloud fraction from file TEMPO_CLDO4_L2	unitless
product/cloud_pressure	cloud pressure from file TEMPO_CLDO4_L2	hPa
band_290_490_nm/irradiance	irradiance from file TEMPO_IRR_L1	photons/s/cm^2/nm
band_290_490_nm/pixel_quality_flag	pixel quality flag from file TEMPO_IRR_L1	unitless
band_290_490_nm/sf_asym	slit function asymmetry parameter from file TEMPO_IRR_L1 (not currently applied in v4)	unitless
band_290_490_nm/sf_hw1e	slit function half-width at 1/e parameter from file TEMPO_IRR_L1 (not currently applied in v4)	nm
band_290_490_nm/sf_shape	slit function shape parameter from file TEMPO_IRR_L1 (not currently applied in v4)	unitless
band_290_490_nm/wavecal_params	wavelength calibration parameters from file TEMPO_IRR_L1	nm
band_290_490_nm/ground_pixel_quality_flag	ground pixel quality flag from file TEMPO_RAD_L1	unitless
band_290_490_nm/inr_quality_flag	INR quality flag from file TEMPO_RAD_L1	unitless
band_290_490_nm/latitude	latitude from file TEMPO_RAD_L1	degrees_north
band_290_490_nm/latitude_bounds	latitude bounds (NE,NW,SW,SE) from file TEMPO_RAD_L1	degrees_north
band_290_490_nm/longitude	longitude from file TEMPO_RAD_L1	degrees_east
band_290_490_nm/longitude_bounds	longitude bounds	degrees_east

	(NE,NW,SW,SE) from file TEMPO_RAD_L1	
band_290_490_nm/pixel_quality_flag	pixel quality flag from file TEMPO_RAD_L1	unitless
band_290_490_nm/radiance	radiance from file TEMPO_RAD_L1	photons/s/cm^2/nm/sr
band_290_490_nm/snow_ice_fraction	snow ice fraction from file TEMPO_RAD_L1	unitless
band_290_490_nm/solar_azimuth_angle	solar azimuth angle from file TEMPO_RAD_L1	degrees
band_290_490_nm/solar_zenith_angle	solar zenith angle from file TEMPO_RAD_L1	degrees
band_290_490_nm/terrain_height	area-weighted mean terrain height from file TEMPO_RAD_L1	m
band_290_490_nm/viewing_azimuth_angle	viewing azimuth angle from file TEMPO_RAD_L1	degrees
band_290_490_nm/viewing_zenith_angle	viewing zenith angle from file TEMPO_RAD_L1	degrees
band_290_490_nm/wavecal_params	wavelength calibration parameters from file TEMPO_RAD_L1	nm
earth_sun_distance	Earth-sun distance from file TEMPO_RAD_L1	m
mirror_step	scan mirror position index from file TEMPO_RAD_L1	unitless
time	exposure start time from file TEMPO_RAD_L1	seconds since 1980-01-06T00:00:00Z
O3	Ozone (O3, MW = 48.00 g mol-1) volume mixing ratio dry air from file GEOS-CF	mol/mol
PHIS	surface geopotential height from file GEOS-CF	m^2/s^2
PS	surface pressure from file GEOS-CF	Pa
T	air temperature from file	K

	GEOS-CF	
TROPPB	tropopause pressure based on blended estimate from file GEOS-CF	Pa
U2M	2-meter eastward wind from file GEOS-CF	m/s
V2M	2-meter northward wind from file GEOS-CF	m/s
lat	latitude from file GEOS-CF	degrees_north
lon	longitude from file GEOS-CF	degrees_east
Ap	Eta a coefficients from GEOS-Chem_72_layer_vertical_grid.nc	unitless
Bp	Eta b coefficients from GEOS-Chem_72_layer_vertical_grid.nc	unitless
alb	albedo from GLER land/snow/ocean files	unitless
doy	day of year from GLER land/snow/ocean files	unitless
hour	hour from GLER land/snow/ocean files	hour
lat	latitude from GLER land/snow/ocean files	degrees_north
lon	longitude from GLER land/snow/ocean files	degrees_east
qf	quality flag from GLER land/snow/ocean files	unitless

3.7. Algorithm Output Variables

Table 3.8. *Algorithm output variables*

Name	Long Name	Unit
geolocation/latitude	pixel center latitude	degrees_north
geolocation/latitude_bounds	pixel corner latitude	degrees_north
geolocation/longitude	pixel center longitude	degrees_east
geolocation/longitude_bounds	pixel corner longitude	degrees_east
geolocation/relative_azimuth_angle	relative azimuth angle	degrees

	at pixel center	
geolocation/solar_zenith_angle	solar zenith angle at pixel center	degrees
geolocation/time	radiance exposure start time	seconds since 1980-01-06T00:00:00Z
geolocation/viewing_zenith_angle	viewing zenith angle at pixel center	degrees
product/nongas_param	non-gas parameter retrieved values	non-gas parameter units
product/nongas_param_error	non-gas parameter solution error	non-gas parameter units
product/nongas_param_precision	non-gas parameter precision	non-gas parameter units
product/other_gas_column	other gas retrieved vertical column density	molecules/cm^2
product/other_gas_column_error	other gas retrieved vertical column density solution error	molecules/cm^2
product/other_gas_column_precision	other gas retrieved vertical column density precision	molecules/cm^2
product/main_data_quality_flag	main data quality flag	unitless
product/ozone_profile	retrieved ozone profile	Dobson Unit
product/ozone_profile_error	retrieved ozone profile solution error	Dobson Unit
product/ozone_profile_precision	retrieved ozone profile precision	Dobson Unit
product/stratosphere_ozone_column	stratospheric ozone column	Dobson Unit
product/stratosphere_ozone_error	stratospheric ozone column solution error	Dobson Unit
product/stratosphere_ozone_precision	stratospheric ozone column precision	Dobson Unit
product/total_ozone_column	total ozone column	Dobson Unit
product/total_ozone_error	total ozone column solution error	Dobson Unit
product/total_ozone_precision	total ozone column precision	Dobson Unit
product/troposphere_ozone_column	troposphere ozone column	Dobson Unit
product/troposphere_ozone_error	troposphere ozone column solution error	Dobson Unit
product/troposphere_ozone_precision	troposphere ozone column precision	Dobson Unit
qa_statistics/avg_residuals	average fitting residuals	percent

qa_statistics/exit_status	retrieval exit status (0=not converged, 1-99 converged, 100-110 converged but with negative ozone value)	unitless
qa_statistics/fit_RMS	ratio of fitting residual to measurement error	unitless
qa_statistics/num_iterations	number of iterations	unitless
support_data/aerosol_index	UV aerosol index	unitless
support_data/cloud_flag	cloud flag	unitless
support_data/correlation_upper_triangular_matrix	correlation matrix (upper matrix) (scale factor = 10000)	unitless
support_data/eff_cloud_fraction	effective cloud fraction	unitless
support_data/eff_cloud_pressure	effective cloud pressure	hPa
support_data/grint_probability	glint probability	unitless
support_data/ground_pixel_quality_flag	ground pixel quality flag	unitless
support_data /nongas_param_apriori	non-gas parameter a priori	non-gas parameter units
support_data /nongas_param_apriori_error	non-gas parameter a priori error	non-gas parameter units
support_data /nongas_param_names	names of non-gas fitted parameters	unitless
support_data /nongas_param_units	units of non-gas fitted parameters	unitless
support_data /num_wavelengths_in_fit	number of wavelengths used in fitting	unitless
support_data /num_wavelengths_in_fit_windows	number of wavelengths in each fitting window	unitless
support_data /other_gas_apriori_column	other gas a priori column density	molecules/cm^2
support_data /other_gas_apriori_error	other gas a priori column density error	molecules/cm^2
support_data /other_gas_names	names of other fitted gases	unitless
support_data /ozone_apriori_profile	a priori ozone profile	Dobson Unit
support_data /ozone_apriori_profile_error	a priori ozone profile error	Dobson Unit
support_data /ozone_averaging_kernel	ozone profile averaging kernels (scale factor = 10000)	unitless
support_data/ozone_degree_of_freedom	ozone degree of freedom for signal	unitless
support_data/ozone_information_content	ozone information content	unitless
support_data/ozone_profile_altitude	altitude of each retrieval layer	km

support_data/ozone_profile_altitude_bounds	altitude of each retrieval layer boundary	km
support_data/ozone_profile_pressure	pressure of each retrieval layer	hPa
support_data/ozone_profile_pressure_bounds	pressure of each retrieval layer boundary	hPa
support_data/ozone_profile_temperature	temperature of each retrieval layer	K
support_data/surface_albedo	surface albedo	unitless
support_data/tropopause_index	tropopause index	unitless
mirror_step	scan mirror position index	unitless
xtrack	pixel index along slit	unitless

4. Product Usage Constraints

4.1. Data Filtering

Users of the TEMPO ozone profile product should, at a minimum, apply data filtering based on the variables in the "qa_statistics" group and cloud fraction. The "quality_flag" variable is not provided in the TEMPO L2 O3PROF product. Therefore, to use the highest quality of data, the user should filter out the low-quality data using the variable as follows:

(1) "eff_cloud_fraction" in the support_data group,
(2) "solar_zenith_angle" and "viewing_zenith_angle" in the geolocation group,
(3) "fit_RMS", "avg_residual", and "retrieval_exit_status" in the qa_statistics group.

The most recommended filtering (do not use) criteria is as follows:

(1) "eff_cloud_fraction" is greater than 0.5.
(2) "solar_zenith_angle" and "viewing_zenith_angle" are greater than 80 degrees.
(3) "fit_RMS" is greater than 3, "avg_residual" is greater than 0.3, and "retrieval_exit_status" is less than 1 or greater than 99.

Note that Level 3 products (gridded data for the entire scan) are pre-filtered, and the different filtering recommendations apply to Level 3.

Because the meaning of the "qa_statistics" variables could change after averaging pixels, we can't provide the "qa_statistics" group in the Level 3 product. Therefore, the TEMPO L3 O3PROF product applied data filtering with "fit_RMS", "avg_residual", and "retrieval_exit_status" as described above before producing the TEMPO L3 O3PROF product. Additional filtering with "eff_cloud_fraction", "solar_zenith_angle", and "viewing_zenith_angle" could be applied for better quality.
Further details on data usage, known issues and file structure may be found in the TEMPO Ozone Profile Level 2 and 3 Data Products User Guide (Park et al., 2025).

5. Performance Assessment

5.1. Validation Methods

The TEMPO ozone profile validation plan and methods are described in the Level 2 Science Data Product Validation Plan (TEMPO Validation Team and TEMPO Ad-hoc Working Group, 2023). The validation plan outlines a validation approach to meet the Program Level Requirements Appendix (PLRA) baseline requirement for TEMPO ozone profile validation and to extend the validation in a best effort approach to leverage measurement and modeling assets over the TEMPO baseline mission. This includes the use of ground-based and satellite observations for routine validation, as well as dedicated and episodic field missions. The TEMPO validation plan defines three levels of product maturity:

1. **Beta**: Product is minimally validated but may contain significant errors. Publication of studies that use these data is discouraged.
2. **Provisional**: Product performance has been demonstrated through a large, but still (seasonally or otherwise) limited number of independent measurements. Product is potentially ready for operational users and may be suitable for scientific publication.
3. **Full**: Product performance has been demonstrated over a large and wide range of representative conditions, with comprehensive documentation of product performance, including known anomalies and their remediation strategies. Products are ready for systematic use and covering the full range of scientific and application use and publication.

Some correlative datasets that can be used for routine assessment of TEMPO total, tropospheric, 0–2 km column ozone, and ozone profile are included in Table 5.1.

Table 5.1. *Datasets for routine assessment of TEMPO ozone profile*

Dataset	Description	Website
PGN	Network of Pandora spectrometers (total column ozone and MAX-DOAS geometry for profile, diurnal variation)	http://pandonia-global-network.org
TOLNet	Lidar stations over the TEMPO FOR (tropospheric and 0–2 km ozone, diurnal variation)	https://tolnet.larc.nasa.gov
Dobson/Brewer	Total ozone, diurnal	https://woudc.org/
ozonesonde	11 stations in TEMPO FOR with 8 actives (ozone profile)	https://ndacc.larc.nasa.gov
IAGOS	In-service Aircraft for a Global Observing System (tropospheric ozone profiles near airports)	https://www.iagos.org
HSRL-2	Airborne lidar during field missions	https://www-

		air.larc.nasa.gov/missions/
Airborne in-situ	In-situ spirals during field missions (tropospheric ozone, 0–2 km ozone)	https://www-air.larc.nasa.gov/missions/
UAH SeaRey	Airborne in-situ (0–2 km ozone)	https://www.nsstc.uah.edu/atmchem/
EPIC/DSCOVR	From L1 orbit (Total ozone, tropospheric ozone, diurnal)	https://asdc.larc.nasa.gov/project/DSCOVR
LEO	TROPOMI, OMI, GOME-2, OMPS-NM, OMPS-NPP, OMPS-LP, TROPRESS (TRopospheric Ozone and its Precursors from Earth System Sounding), and MLS	Data archives for those satellite instruments

Satellite-based measurements provide ample cross-validation opportunities with large spatial coverage and similar spatial resolution, but only at one time per day from LEO or hourly from the Lagrange-1 point Earth Polychromatic Imaging Camera (EPIC)/Deep Space Climate Observatory (DSCOVR). Minimizing errors due to spatiotemporal collocation and sampling makes it easier to conduct comparisons as a function of various geophysical parameters such as cloud fraction and cloud-height, surface albedo, and viewing geometry. In particular, satellite-based instruments provided a tool to perform immediate validation during pre-beta assessments with a rich legacy of prior validation. To validate TEMPO products, preference will be given to use of publicly available and carefully validated satellite data products. Before release to the science team for further involvement and validation, we conducted an initial assessment of the TEMPO O3PROF product using limited qualitative comparisons with correlative products. In this assessment, we examined the spatiotemporal distribution of the retrievals to confirm that they were reasonable and did not show very large biases or pronounced spatiotemporally dependent anomalies. Based on our initial assessment, spatial comparisons with other LEO satellite products, including EPIC, TROPOMI, and OMI, showed that TEMPO O3PROF reproduced day-to-day spatial patterns with high consistency with low bias in TCO column ozone. Comparisons with TOLNet ground-based lidar observations for the 0–2 km and TrCO showed an overall good agreement, with systematic biases of about –10%. In addition, comparisons of the 0–2 km subcolumn with HSRL-2 airborne lidar observations over Chicago and New York City showed high correlations exceeding 0.65 and demonstrated that the temporal variability was well captured.

For higher-level validation, careful quantitative intercomparison and analysis will be conducted. The intercomparisons will focus on geographic regions of interest representative of different scenarios within TEMPO's domain. The goal is to explore retrieval performance as a function of geophysical parameters and observation geometries. To conduct map intercomparisons over the TEMPO domain, our O3PROF product will be compared with available LEO and DSCOVR-EPIC datasets. To facilitate such intercomparisons, we will rely on LEO and EPIC level 3

products, if readily available, or if not, then by calculating a TEMPO average within each LEO and EPIC observation boundary. TEMPO measurements will be interpolated to the same overpass time as LEO and EPIC measurements. L2 products from TEMPO and other satellite measurements will also be used when performing close comparisons as a function of geophysical parameters such as cloud fraction, cloud top pressure, surface albedo, ozone column, and viewing geometry, or when comparing retrievals also with similar viewing geometry.

In addition to satellite observations, available ground-based lidar instruments from TOLNet in the TEMPO FOR can be used to validate 0–2 km and tropospheric ozone and their diurnal variation. The Pandonia Global Network (PGN), with more than 60 Pandora instruments over the TEMPO FOR, and with ~20 to be added by the end of 2023, can be used to validate total ozone and its diurnal variation. Pandora can operate in sky-light mode or Multi-Axis Differential Optical Absorption Spectroscopy (MAX-DOAS) mode, and measure ozone profile in the lower troposphere, and can also be used to validate 0–2 km ozone and its diurnal variation. Prior to the routine operation of TOLNet and PGN networks, ozonesonde, Dobson, and Brewer observations have been the main ground-based measurements used to validate ozone profiles and tropospheric and total ozone for our TEMPO O3PROF measurements. There are 11 ozonesonde stations, with 8 active (weekly launches), and many Dobson and Brewer stations in the TEMPO FOR. We will continue to use those measurements to validate our TEMPO products.

In-service Aircraft for a Global Observing Service (IAGOS) measures tropospheric ozone profiles at 52 airports in the TEMPO FOR and can be used to validate tropospheric and 0–2 km ozone. The University of Alabama in Huntsville (UAH) SeaRey aircraft can sample in-situ ozone near the surface within 1 or a few TEMPO pixels and can be used to validate 0–2 km ozone. Airborne measurements can be taken during various field missions. Multiple field campaigns that include airborne in situ and remote sensing instruments are planned to occur during the TEMPO baseline mission. If they overlap with TEMPO operations, these will provide valuable data for ozone validation. These campaigns include NASA's Synergistic TEMPO Air Quality Science (STAQS), NOAA's Atmospheric Emissions and Reactions Observed from Megacities to Marine Areas (AEROMMA), NOAA's Coastal Urban Plume Dynamics Study (CUPIDS), and NOAA's Greater New York Oxidant Trace gas Halogen and Aerosol Airborne Mission (GOTHAAM), all in Summer 2023. These datasets can be used to evaluate and validate the reprocessed V04 TEMPO O3PROF. In-situ spirals of ozone profile and High Spectral Resolution LIDAR-2 (HSRL-2) of ozone profiles can be used to validate collocated tropospheric and 0–2 km ozone.

5.2. Uncertainties

Uncertainties in the comparisons arise from spatiotemporal sampling mismatches, spatiotemporal smoothing mismatches, and uncertainty in the coincident column derived from correlative measurements. Sampling mismatches arise because TEMPO and the correlative observations are

not perfectly matched in location and time due to differences in footprint size, spatial and temporal offsets. Smoothing mismatches arise because TEMPO ozone retrievals have finite horizontal footprint and limited vertical resolution, characterized by their retrieval sensitivity and averaging kernels, whereas correlative measurements may have much finer spatial or vertical resolution. Consequently, part of the observed difference may reflect representativeness of error rather than retrieval error. Additional uncertainty is introduced when constructing coincident columns from correlative data, particularly where interpolation, extrapolation, or assumptions about unmeasured layers are required. The magnitude of these uncertainties varies among the correlative datasets and is described in the Validation Plan (TEMPO Validation Team, 2023) and the relevant references.

5.3. Verification of Science Requirements

The main baseline science requirements for TEMPO are defined in the TEMPO Program Level Requirements Appendix (PLRA). It specifies the precision requirements within the required temporal visit for TCO, TrCO, 0–2 km column ozone, tropospheric NO_2, and tropospheric HCHO for retrievals under clear-sky conditions, with solar zenith angles less than 70°, with spatial resolutions ≤ 60 km^2 at the center of FOR. The first 3 requirements apply to the O3PROF product. Specifically, they are less than 10 ppbv within 1-hour revisit for tropospheric O_3, less than 10 ppbv within 2-hour revisit under selected scenes for 0–2 km column ozone, and within 3% within 1-hour for TCO.

The TEMPO O3PROF L2 product provides the solution error and precision for the retrieved ozone profile and for the derived total, tropospheric, and stratospheric column ozone hourly at the spatial resolution of 38 km^2 at the center of FOR. We use the solution error (root square sum of precision and smoothing errors) for comparison with the precision requirements accounting for the limited vertical sensitivity of the retrievals. We assume these errors are random (or pseudo-random) so that the error is inversely proportional to the square root of temporal revisit and the spatial resolution. Therefore, we can calculate the equivalent error at the required temporal visit and spatial resolution for comparison against the requirement.

Figure 5.1 shows the distribution of solution errors for TCO, TRCO, and 0–2 km column ozone from all scans (S001–S018) on July 10, 2025. The red vertical line indicates the mission precision requirement. The TCO error is the error at 38 km^2 without adjustment for spatial resolution as it has already met the requirements for 100% of the pixels. The error of TrCO is equivalently adjusted for 60 km^2 spatial resolution, and the error of 0–2 km column ozone is equivalently adjusted for 60 km^2 spatial resolution and 2-hour temporal visit. The TrCO error meets the requirement for nearly 100% of the pixels. The 0-2 km column ozone error meets the requirement for 88% of the pixels but the requirement is for selected scenes. We checked the performance in different seasons and the performances are similar. The results indicate that the

TCO, TrCO, and 0–2 km column ozone all satisfy the mission science precision requirements.

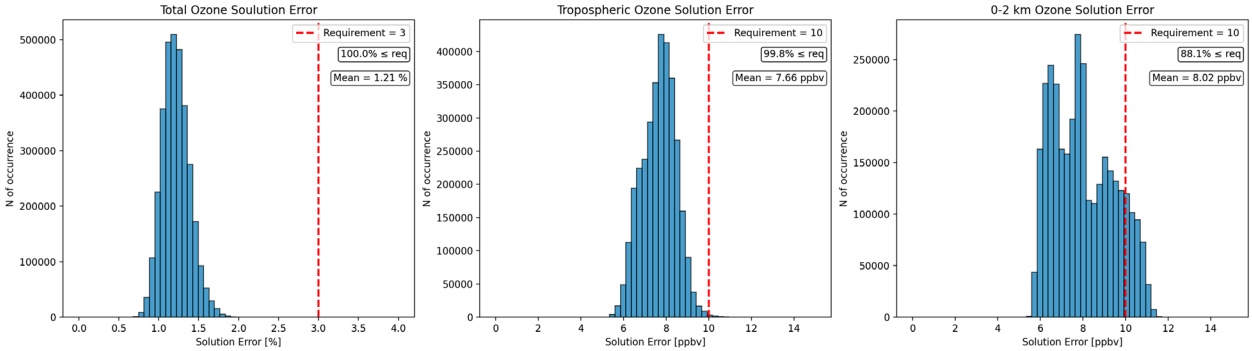

Figure 5.1. *Histogram of TEMPO total, tropospheric, and 0–2 km column ozone solution error included in the Level 2 files for all scans (S001–S018) on July 10, 2025. The data only used with specific filtering conditions (solar zenith angle (less than or equal to 70°), viewing zenith angle (less than or equal to 70°), cloud fraction (less than or equal to 0.1), exit status (less than or equal to 99 and greater than or equal to 1), fit RMS (less than or equal to 3), and fit residual (less than or equal to 0.3).*

5.4. Validation and Evaluation

It is important to note that the validation and inter-comparison results presented in the following sections are based on the preliminary version of the TEMPO O3PROF V04 product (referred to as *V04). This dataset was generated during the initial calibration and validation (Cal/Val) phase prior to the final operational release. While the core retrieval algorithm and physics remain consistent, minor discrepancies may exist between the preliminary data used herein and the officially released V04 TEMPO O3PROF products due to subsequent updates in configuration parameters. Therefore, the results should be interpreted as a representative assessment of the algorithm's performance, acknowledging that slight numerical deviations may be present in the final public dataset.

5.4.1. Evaluation of TEMPO Ozone Profile using Independent Satellite Retrievals

To evaluate the performance of the *V04 TEMPO O3PROF algorithm, a spatial inter-comparison was conducted using concurrent measurements from the EPIC (EPIC high-resolution observations provided by Jerry R. Ziemke from NASA GSFC), TROPOMI (TROPOMI research product generated based on a research algorithm developed by Juseon Bak using the SAO algorithm (Bak et al., 2025b)), and OMI (OMI version 2 product provided by Juseon Bak (Bak et al., 2024a)) sensors. Figure 5.2 presents the spatial distribution of total column ozone (top row) and tropospheric column ozone (bottom row) over the TEMPO domain on July 26, 2024 (S007). As shown in the top panels, the total column ozone retrieved from TEMPO agrees well with the reference sensors, though it exhibits a low bias relative to the others. The TEMPO O3PROF product accurately captures the large-scale latitudinal gradients, ranging from lower concentrations in the sub-tropics to higher values at northern latitudes. Furthermore, synoptic-

scale meteorological features, particularly the dynamical patterns associated with pressure systems over the northern United States and Canada, are resolved with morphological structures that agree well with the high-resolution TROPOMI data and the synoptic perspective of EPIC.

The bottom panels show comparisons for tropospheric column ozone. Despite the inherent challenges in tropospheric column ozone retrieval, TEMPO O3PROF exhibits strong spatial coherence with the validation datasets. Notably, the regional enhancement band observed across the central and eastern United States, indicated by values between 30 and 50 DU, is consistently detected by all sensors. TEMPO effectively reproduces the fine-scale spatial heterogeneity observed in TROPOMI while providing continuous coverage across the observation domain, thereby avoiding the orbital gaps and row anomalies present in the OMI record. Consequently, these qualitative comparisons validate the TEMPO O3PROF algorithm's ability to monitor both total and tropospheric ozone distributions reliably.

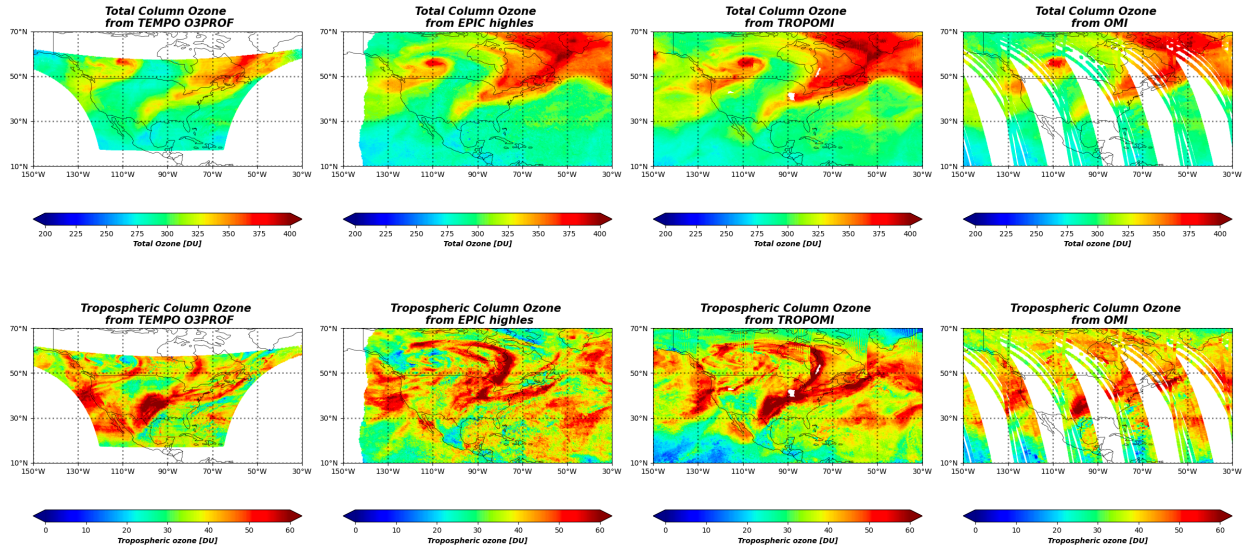

Figure 5.2. *Spatial comparison of total column ozone (top row) and tropospheric column ozone (bottom row) over North America. The panels display retrieval results from the TEMPO O3PROF (*V04), the EPIC high-resolution (provided by Jerry R. Ziemky from NASA GSFC), TROPOMI research algorithm (provided by Juseon Bak from Pusan National University), and OMI v2 (provided by Juseon Bak from Pusan National University) from left to right. The color scales represent ozone column density in Dobson Units [DU].*

5.4.2. Evaluation of TEMPO Ozone Profile using ground-based TOLNet observation

To evaluate the accuracy of the ozone vertical profile from the TEMPO O3PROF product in the troposphere, we compared it (conducted by Matthew Johnson from NASA Ames Research Center) with high-resolution vertical ozone profiles from TOLNet. Since satellite sensors generally have more limited vertical resolution than ground-based lidar measurements, direct comparisons can be affected by differences in vertical smoothing between two different observations. Therefore, following the standard method used in previous studies, we applied the

TEMPO averaging kernels (AK) to the high-resolution TOLNet data (Rodgers & Connor, 2003). This creates a smoothed reference profile (labeled as TOLNet (A) in Figure 5.3). This step allows for a fair and valid comparison between the two datasets.

Figure 5.3 shows the mean vertical ozone profiles in the troposphere (0–12 km) using the 862-colocated dataset at Chicago and New York City during the ground observation campaign period (August 2–15, 2023). As shown in the left panel, the TEMPO retrieval (red solid line) generally follows the vertical structure of the smoothed TOLNet observations (black solid line). The coefficient of determination (R^2) improves significantly from 0.17 against raw data to 0.63 against the smoothed profiles. Regarding the bias, the product shows a systematic underestimation with a Normalized Mean Bias (NMB) of -10.9% (Bias = -0.89 DU). Although TEMPO tends to retrieve lower absolute ozone values, the strong correlation confirms that the O3PROF product reliably detects the vertical shapes and variability of ozone profiles.

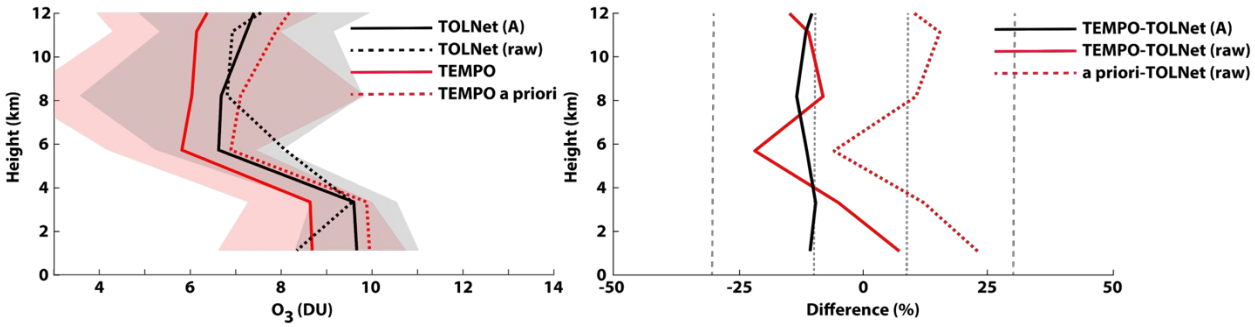

Figure 5.3. *Validation of TEMPO ozone vertical profiles against ground-based TOLNet Lidar observations. (Left) Comparison of mean vertical ozone profiles (0–12 km) derived from the co-located dataset. The red solid line represents the TEMPO retrieval, and the red dashed line is the TEMPO a priori profile. The ground-based references are shown as the raw TOLNet data (black dotted line) and the smoothed TOLNet data convolved with TEMPO averaging kernels (black solid line). The shaded regions indicate the standard deviation of the variability. (Right) Vertical distribution of the relative mean difference (%). The black solid line indicates the bias relative to the smoothed TOLNet profile (TEMPO - TOLNet(A)). In contrast, the red solid and dashed lines show the differences between TEMPO and raw Lidar data and a priori and raw Lidar data, respectively.*

5.4.3. Evaluation of TEMPO Ozone Profile using air-borne HSRL-2 observation

To validate the TEMPO O3PROF product in the lower troposphere, specifically for 0–2 km column ozone, we utilized (conducted by Laura Judd and Mary Angelique Demetillo from NASA LaRC) airborne measurements from HSRL-2. The validation campaign focused on the complex urban environments of Chicago and New York City during August 2023. This comparison is particularly critical as retrieving near-surface ozone from space is challenging due to reduced sensitivity and surface interferences. The analysis focuses on the 0–2 km sub-column ozone mixing ratios to assess TEMPO's capability to resolve near-surface pollution variability.

Figure 5.4 shows the temporal evolution of mean ozone concentrations (0–2 km) for TEMPO, HSRL-2, and ground-based in-situ monitors. The TEMPO retrieval (black line) generally captures the diurnal variability and magnitude of ozone pollution events observed by both the HSRL-2 (orange line) and ground stations (blue line). However, notable discrepancies are observed during specific time windows. While potential factors such as sampling gradients or marine layer effects are annotated in the figure, further investigation with an expanded dataset is required to better understand and definitively characterize these discrepancies. Despite these challenges, TEMPO successfully follows the overall temporal trends of ozone enhancement and depletion. However, it should also be noted that the V04 TEMPO 0–2 km ozone DFS is generally very low, typically below 0.3, indicating limited measurement sensitivity in the surface layer. Therefore, the apparent agreements in the 0–2 km time series should be interpreted with caution, as part of the variability may reflect a priori influence rather than direct observational constraint.

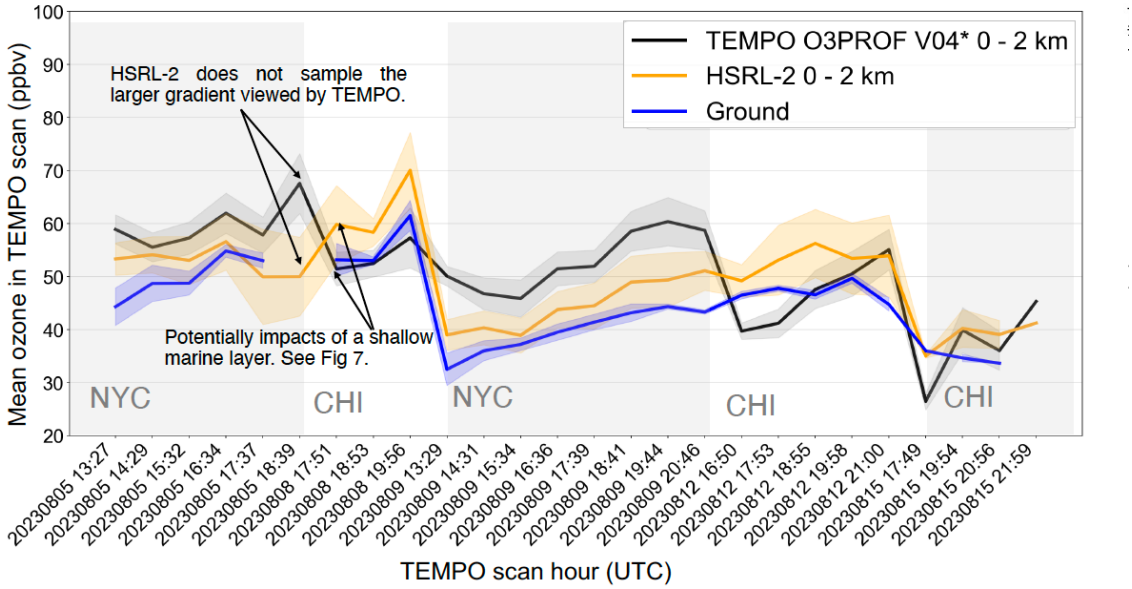

Figure 5.4. *Validation of TEMPO 0–2 km ozone sub-columns against air-borne HSRL-2 and ground-based in-situ measurements. Time series comparison of mean ozone mixing ratios (ppbv) in the 0–2 km layer during the campaign period (August 2023). The plot compares TEMPO O3PROF V04* (black), HSRL-2 (orange), and ground-based in-situ observations (blue). Shaded areas represent the variability (standard deviation).*

A quantitative assessment of the retrieval accuracy is presented in the scatter plots in Figure 5.5. The correlation analysis indicates a consistent retrieval performance across different urban domains, with Pearson correlation coefficients (R) of 0.68 for Chicago and 0.67 for New York City. Interestingly, the bias exhibits regional dependence; the Chicago domain shows a negative bias (Mean Bias = -6.02 ppb, NMB = -11.48%), whereas the New York City domain indicates a positive bias (Mean Bias = 6.91 ppb, NMB = 14.54%). These opposing biases imply that local

factors, such as surface albedo heterogeneity, aerosol loading, or a priori constraints specific to each region, may influence the baseline accuracy of the 0–2 km retrieval. Nevertheless, the consistent correlation confirms TEMPO's potential for monitoring boundary layer ozone dynamics.

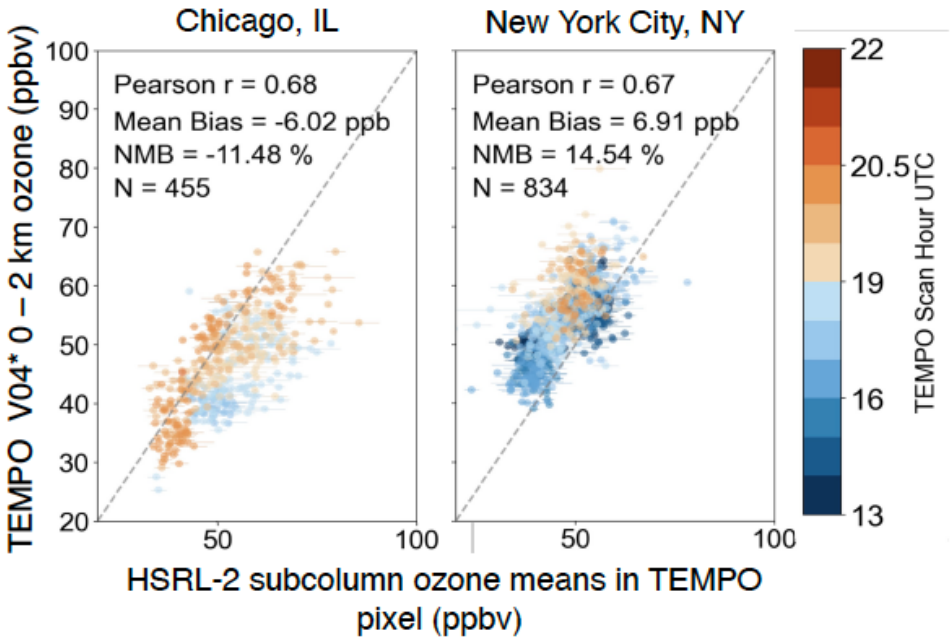

Figure 5.5. *Validation of TEMPO 0–2 km ozone sub-columns against air-borne HSRL-2 measurements. Scatter plots of TEMPO versus HSRL-2 0–2 km ozone for Chicago (left) and New York City (right). The color scale indicates the TEMPO scan hour (UTC). Statistical metrics, including Pearson correlation (R), Mean Bias, and Normalized Mean Bias (NMB), are provided for each domain.*

6. Algorithm Implementation

6.1. Algorithm Availability

The TEMPO ozone profile algorithm has been integrated into the TEMPO Science Data Processing Center (SDPC) pipeline at the Smithsonian Astrophysical Observatory. SDPC v4.7 is used to produce the version 4 data that was publicly released on 17 September 2025.

6.2. Input Data Access

URL	Description
(Rodgers & Connor, 2003)	TEMPO Level 1B Irradiance Product
https://dx.doi.org/10.5067/IS-40e/TEMPO/RAD_L1.004	TEMPO Level 1B Radiance Product
https://dx.doi.org/10.5067/10.5067/IS-40e/TEMPO/CLDO4_L2.004	TEMPO Level 2 Cloud Product

6.3. Output Data Access

URL	Description
https://doi.org/10.5067/IS-40e/TEMPO/O3PROF_L2.004	TEMPO Level 2 O3PROF Product
https://doi.org/10.5067/IS-40e/TEMPO/O3PROF_L3.004	TEMPO Level 3 (gridded) O3PROF Product

6.4. Important Related URLs

URL	Description
https://tempo.si.edu	Smithsonian Institution project homepage
https://asdc.larc.nasa.gov/project/TEMPO	ASDC project homepage

Contact Details

Junsung Park	
Roles	Writing – original draft & Writing – review & editing & Corresponding Author
Affiliation	Center for Astrophysics | Harvard & Smithsonian
Email	Joonsung. park@cfa.harvard.edu
URL	https://www.cfa.harvard.edu/people/junsung-park
UUID	https://orcid.org/0000-0002-5343-4246

Xiong Liu	
Roles	Writing – original draft, Writing – review & editing & Funding acquisition
Affiliation	Center for Astrophysics | Harvard & Smithsonian
Email	xliu@cfa.harvard.edu
URL	https://lweb.cfa.harvard.edu/~xliu/
UUID	https://orcid.org/0000-0003-2939-574X

Juseon Bak	
Roles	Writing – original draft, Writing – review
Affiliation	Pusan National University
Email	juseonbak@pusan.ac.kr
URL	
UUID	https://orcid.org/0000-0002-0421-671X

References

Bak, J., Kim, J. H., Spurr, R. J. D., Liu, X., & Newchurch, M. J. (2012). Sensitivity study of ozone retrieval from UV measurements on geostationary platforms. *Remote Sensing of Environment*, *118*, 309–319. https://doi.org/10.1016/j.rse.2011.11.010

Bak, J., Kim, J. H., Liu, X., Chance, K., & Kim, J. (2013a). Evaluation of ozone profile and tropospheric ozone retrievals from GEMS and OMI spectra. *Atmospheric Measurement Techniques*, *6*(2), 239–249. https://doi.org/10.5194/amt-6-239-2013

Bak, J., Liu, X., Wei, J. C., Pan, L. L., Chance, K., & Kim, J. H. (2013b). Improvement of OMI ozone profile retrievals in the upper troposphere and lower stratosphere by the use of a tropopause-based ozone profile climatology. *Atmospheric Measurement Techniques*, *6*(9), 2239–2254. https://doi.org/10.5194/amt-6-2239-2013

Bak, J., Liu, X., Kim, J. H., Deland, M. T., & Chance, K. (2016). Improvement of OMI ozone profile retrievals by simultaneously fitting polarmesospheric clouds. *Atmospheric Measurement Techniques*, *9*(9), 4521–4531. https://doi.org/10.5194/amt-9-4521-2016

Bak, J., Liu, X., Kim, J.-H., Haffner, D. P., Chance, K., Yang, K., & Sun, K. (2017). Characterization and correction of OMPS nadir mapper measurements for ozone profile retrievals. *Atmospheric Measurement Techniques*, *10*(11), 4373–4388. https://doi.org/10.5194/amt-10-4373-2017

Bak, J., Baek, K.-H., Kim, J.-H., Liu, X., Kim, J., & Chance, K. (2019a). Cross-evaluation of GEMS tropospheric ozone retrieval performance using OMI data and the use of an ozonesonde dataset over East Asia for validation. *Atmospheric Measurement Techniques*, *12*(9), 5201–5215. https://doi.org/10.5194/amt-12-5201-2019

Bak, J., Liu, X., Sun, K., Chance, K., & Kim, J.-H. (2019b). Linearization of the effect of slit function changes for improving Ozone Monitoring Instrument ozone profile retrievals. *Atmospheric Measurement Techniques*, *12*(7), 3777–3788. https://doi.org/10.5194/amt-12-3777-2019

Bak, J., Liu, X., Birk, M., Wagner, G., Gordon, I. E., & Chance, K. (2020). Impact of using a new ultraviolet ozone absorption cross-section dataset on OMI ozone profile retrievals. *Atmospheric Measurement Techniques*, *13*(11), 5845–5854. https://doi.org/10.5194/amt-13-5845-2020

Bak, J., Liu, X., Spurr, R., Yang, K., Nowlan, C. R., Miller, C. C., Abad, G. G., & Chance, K. (2021a). Radiative transfer acceleration based on the principal component analysis and lookup table of corrections: Optimization and application to UV ozone profile retrievals. *Atmospheric Measurement Techniques*, *14*(4), 2659–2672. https://doi.org/10.5194/amt-14-2659-2021

Bak, J., Coddington, O., Liu, X., Chance, K., Lee, H.-J., Jeon, W., Kim, J.-H., & Kim, C.-H. (2021b). Impact of Using a New High-Resolution Solar Reference Spectrum on OMI Ozone Profile Retrievals. *Remote Sensing*, *14*(1), 37. https://doi.org/10.3390/rs14010037

Bak, J., Liu, X., Yang, K., Gonzalez Abad, G., O'Sullivan, E., Chance, K., & Kim, C.-H. (2024). An improved OMI ozone profile research product version 2.0 with collection 4 L1b data and algorithm updates. *Atmospheric Measurement Techniques*, *17*(7), 1891–1911. https://doi.org/10.5194/amt-17-1891-2024

Bak, J., Liu, X., Abad, G. G., & Yang, K. (2025). An Extension of Ozone Profile Retrievals from TROPOMI Based on the SAO2024 Algorithm. *Remote Sensing*, *17*(5), 779. https://doi.org/10.3390/rs17050779

Bak, J., Keppens, A., Choi, D., Hong, S., Kim, J.-H., Kim, C.-H., Lee, H.-J., Jeon, W., Kim, J., Koo, J.-H., Kim, J., Baek, K., Yang, K., Liu, X., Abad, G. G., Heue, K.-P., Lambert, J.-C., Jung, Y., Hong, H., & Lee, W.-J. (2026). GEMS ozone profile retrieval: Impact and validation of version 3.0 improvements. *Atmospheric Measurement Techniques*, *19*(1), 119–134. https://doi.org/10.5194/amt-19-119-2026

Beirle, S., Lampel, J., Lerot, C., Sihler, H., & Wagner, T. (2017). Parameterizing the instrumental spectral response function and its changes by a super-Gaussian and its derivatives. *Atmospheric Measurement Techniques*, *10*(2), 581–598. https://doi.org/10.5194/amt-10-581-2017

Bey, I., Jacob, D. J., Yantosca, R. M., Logan, J. A., Field, B. D., Fiore, A. M., Li, Q., Liu, H. Y., Mickley, L. J., & Schultz, M. G. (2001). Global modeling of tropospheric chemistry with assimilated meteorology: Model description and evaluation. *Journal of Geophysical Research: Atmospheres*, *106*(D19), 23073–23095. https://doi.org/10.1029/2001JD000807

Bhartia, P. K., McPeters, R. D., Mateer, C. L., Flynn, L. E., & Wellemeyer, C. (1996). Algorithm for the estimation of vertical ozone profiles from the backscattered ultraviolet technique. *Journal of Geophysical Research: Atmospheres*, *101*(D13), 18793–18806. https://doi.org/10.1029/96JD01165

Boersma, K. F., Eskes, H. J., & Brinksma, E. J. (2004). Error analysis for tropospheric NO_2 retrieval from space. *Journal of Geophysical Research: Atmospheres*, *109*(D4), 2003JD003962. https://doi.org/10.1029/2003JD003962

Bogumil, K., Orphal, J., Homann, T., Voigt, S., Spietz, P., Fleischmann, O. C., Vogel, A., Hartmann, M., Kromminga, H., Bovensmann, H., Frerick, J., & Burrows, J. P. (2003). Measurements of molecular absorption spectra with the SCIAMACHY pre-flight model: Instrument characterization and reference data for atmospheric remote-sensing in the 230–2380 nm region. *Journal of Photochemistry and Photobiology A: Chemistry*, *157*(2–3), 167–184. https://doi.org/10.1016S1010-6030(03)00062-5

Bovensmann, H., Burrows, J. P., Buchwitz, M., Frerick, J., Noël, S., Rozanov, V. V., Chance, K. V., & Goede, A. P. H. (1999). SCIAMACHY: Mission Objectives and Measurement Modes. *Journal of the Atmospheric Sciences*, *56*(2), 127–150. https://doi.org/10.1175/1520-0469(1999)056%253C0127:SMOAMM%253E2.0.CO;2

Brion, J., Chakir, A., Daumont, D., Malicet, J., & Parisse, C. (1993). High-resolution laboratory absorption cross section of O3. Temperature effect. *Chemical Physics Letters*, *213*(5–6), 610–612. https://doi.org/10.1016/0009-2614(93)89169-I

Brion, J., Chakir, A., Charbonnier, J., Daumont, D., Parisse, C., & Malicet, J. (1998). Absorption Spectra Measurements for the Ozone Molecule in the 350–830 nm Region. *Journal of Atmospheric Chemistry*, *30*(2), 291–299. https://doi.org/10.1023/A:1006036924364

Buchard, V., Randles, C. A., Da Silva, A. M., Darmenov, A., Colarco, P. R., Govindaraju, R., Ferrare, R., Hair, J., Beyersdorf, A. J., Ziemba, L. D., & Yu, H. (2017). The MERRA-2 Aerosol Reanalysis, 1980 Onward. Part II: Evaluation and Case Studies. *Journal of Climate*, *30*(17), 6851–6872. https://doi.org/10.1175/JCLI-D-16-0613.1

Burrows, J. P., Weber, M., Buchwitz, M., Rozanov, V., Ladstätter-Weißenmayer, A., Richter, A., DeBeek, R., Hoogen, R., Bramstedt, K., Eichmann, K.-U., Eisinger, M., & Perner, D. (1999). The Global Ozone Monitoring Experiment (GOME): Mission Concept and First Scientific Results. *Journal of the Atmospheric Sciences*, *56*(2), 151–175. https://doi.org/10.1175/1520-0469(1999)056%253C0151:TGOMEG%253E2.0.CO;2

Cai, Z., Liu, Y., Liu, X., Chance, K., Nowlan, C. R., Lang, R., Munro, R., & Suleiman, R. (2012). Characterization and correction of Global Ozone Monitoring Experiment 2 ultraviolet measurements and application to ozone profile retrievals. *Journal of Geophysical Research: Atmospheres*, *117*(D7), 2011JD017096. https://doi.org/10.1029/2011JD017096

Carn, S. (2019). *Multi-Satellite Volcanic Sulfur Dioxide L4 Long-Term Global Database V3* [Dataset]. NASA Goddard Earth Sciences Data and Information Services Center. https://doi.org/10.5067/MEASURES/SO2/DATA404

Chameides, W. L., Kasibhatla, P. S., Yienger, J., & Levy, H. (1994). Growth of Continental-Scale Metro-Agro-Plexes, Regional Ozone Pollution, and World Food Production. *Science*, *264*(5155), 74–77. https://doi.org/10.1126/science.264.5155.74

Chan Miller, C., Nowlan, C. R., Bak, J., Liu, X., Gonzalez Abad, G., Zoogman, P., & Chance, K. (2019). *A probabilistic model of surface reflectance for atmospheric retrieval algorithms from the UV to SWIR*. *2019*, A13J-2935. https://ui.adsabs.harvard.edu/abs/2019AGUFM.A13J2935C

Chance, K. (1998). Analysis of BrO measurements from the Global Ozone Monitoring Experiment. *Geophysical Research Letters*, *25*(17), 3335–3338. https://doi.org/10.1029/98GL52359

Chance, K., Kurosu, T. P., & Sioris, C. E. (2005). Undersampling correction for array detector-based satellite spectrometers. *Applied Optics*, *44*(7), 1296. https://doi.org/10.1364/AO.44.001296

Chance, K., & Kurucz, R. L. (2010). An improved high-resolution solar reference spectrum for earth's atmosphere measurements in the ultraviolet, visible, and near infrared. *Journal of Quantitative Spectroscopy and Radiative Transfer*, *111*(9), 1289–1295. https://doi.org/10.1016/j.jqsrt.2010.01.036

Chance, K., & Orphal, J. (2011). Revised ultraviolet absorption cross sections of H2CO for the HITRAN database. *Journal of Quantitative Spectroscopy and Radiative Transfer*, *112*(9), 1509–1510. https://doi.org/10.1016/j.jqsrt.2011.02.002

Chance, K. V., Burrows, J. P., Perner, D., & Schneider, W. (1997). Satellite measurements of atmospheric ozone profiles, including tropospheric ozone, from ultraviolet/visible measurements in the nadir geometry: A potential method to retrieve tropospheric ozone. *Journal of Quantitative Spectroscopy and Radiative Transfer*, *57*(4), 467–476. https://doi.org/10.1016/S0022-4073(96)00157-4

Choi, H., Liu, X., Jeong, U., Chong, H., Kim, J., Ahn, M. H., Ko, D. H., Lee, D.-W., Moon, K.-J., & Lee, K.-M. (2024). Geostationary Environment Monitoring Spectrometer (GEMS) polarization characteristics and correction algorithm. *Atmospheric Measurement Techniques*, *17*(1), 145–164. https://doi.org/10.5194/amt-17-145-2024

Chong, H., Liu, X., Houck, J. C., Flittner, D. E., Carr, J. L., Hou, W., Davis, J. E., Suleiman, R., Chance, K. V., Mishra, N., Miller, C. C., Abad, G. G., Baker, B., Lasnik, J., Nicks, D., Bak, J., Nowlan, C. R., Wang, H., Park, J., Jean, F., Carpenter, L. (2026). Algorithm theoretical basis for version 3 TEMPO level 0–1 processor. Algorithm theoretical basis for Version 3 TEMPO Level 0-1 processor. *Earth and Space Science, 13(2), p.e2025EA004516.* https://doi.org/10.1029/2025EA004516

Coddington, O. M., Richard, E. C., Harber, D., Pilewskie, P., Woods, T. N., Chance, K., Liu, X., & Sun, K. (2021). The TSIS-1 Hybrid Solar Reference Spectrum. *Geophysical Research Letters*, *48*(12), e2020GL091709. https://doi.org/10.1029/2020GL091709

Cooper, R. N., Houghton, J. T., McCarthy, J. J., & Metz, B. (2002). Climate Change 2001: The Scientific Basis. *Foreign Affairs*, *81*(1), 208. https://doi.org/10.2307/20033020

Cox, C., & Munk, W. (1954). Measurement of the Roughness of the Sea Surface from Photographs of the Sun's Glitter. *Journal of the Optical Society of America*, *44*(11), 838. https://doi.org/10.1364/JOSA.44.000838

Crutzen, P. J. (1988). Tropospheric Ozone: An Overview. In I. S. A. Isaksen (Ed.), *Tropospheric Ozone* (pp. 3–32). Springer Netherlands. https://doi.org/10.1007/978-94-009-2913-5_1

Danielson, J. J., & Gesch, D. B. (2011). Global multi-resolution terrain elevation data 2010 (GMTED2010). In *Open-File Report* (Nos. 2011–1073). U.S. Geological Survey. https://doi.org/10.3133/ofr20111073

Darmenov, A. S., & da Silva, A. M. (2015). *The Quick Fire Emissions Dataset (QFED):Documentation of Versions 2.1, 2.2 and 2.4*. *38*. https://ntrs.nasa.gov/api/citations/20180005253/downloads/20180005253.pdf

Daumont, D., Brion, J., Charbonnier, J., & Malicet, J. (1992). Ozone UV spectroscopy I: Absorption cross-sections at room temperature. *Journal of Atmospheric Chemistry*, *15*(2), 145–155. https://doi.org/10.1007/BF00053756

Di Pede, S., Loots, E., Ludewig, A., Van Der Plas, E., Van Amelrooy, E., Van Hoek, M., Sneep, M., Ter Linden, M., Keppens, A., & Veefkind, J. P. (2026). Characterization and improvements of the UV radiometric calibration for the TROPOMI operational ozone profile retrieval algorithm. *Atmospheric Measurement Techniques*, *19*(5), 1875–1899. https://doi.org/10.5194/amt-19-1875-2026

Eastham, S. D., Weisenstein, D. K., & Barrett, S. R. H. (2014). Development and evaluation of the unified tropospheric–stratospheric chemistry extension (UCX) for the global chemistry-transport model GEOS-Chem. *Atmospheric Environment*, *89*, 52–63. https://doi.org/10.1016/j.atmosenv.2014.02.001

Fasnacht, Z., Vasilkov, A., Haffner, D., Qin, W., Joiner, J., Krotkov, N., Sayer, A. M., & Spurr, R. (2019). A geometry-dependent surface Lambertian-equivalent reflectivity product for UV–Vis retrievals – Part 2: Evaluation over open ocean. *Atmospheric Measurement Techniques*, *12*(12), 6749–6769. https://doi.org/10.5194/amt-12-6749-2019

Finkenzeller, H., & Volkamer, R. (2022). O2–O2 CIA in the gas phase: Cross-section of weak bands, and continuum absorption between 297–500 nm. *Journal of Quantitative Spectroscopy and Radiative Transfer*, *279*, 108063. https://doi.org/10.1016/j.jqsrt.2021.108063

Fishman, J., Ramanathan, V., Crutzen, P. J., & Liu, S. C. (1979). Tropospheric ozone and climate. *Nature*, *282*(5741), 818–820. https://doi.org/10.1038/282818a0

Flynn, L., Long, C., Wu, X., Evans, R., Beck, C. T., Petropavlovskikh, I., McConville, G., Yu, W., Zhang, Z., Niu, J., Beach, E., Hao, Y., Pan, C., Sen, B., Novicki, M., Zhou, S., & Seftor, C. (2014). Performance of the Ozone Mapping and Profiler Suite (OMPS) products. *Journal of Geophysical Research: Atmospheres*, *119*, 6181–6195. https://doi.org/10.1002/2013JD020467

Friedl, M. A., McIver, D. K., Hodges, J. C. F., Zhang, X. Y., Muchoney, D., Strahler, A. H., Woodcock, C. E., Gopal, S., Schneider, A., Cooper, A., Baccini, A., Gao, F., & Schaaf, C. (2002). Global land cover mapping from MODIS: Algorithms and early results. *Remote Sensing of Environment*, *83*(1–2), 287–302. https://doi.org/10.1016/S0034-4257(02)00078-0

Friedl, M. A., Sulla-Menashe, D., Tan, B., Schneider, A., Ramankutty, N., Sibley, A., & Huang, X. (2010). MODIS Collection 5 global land cover: Algorithm refinements and characterization of new datasets. *Remote Sensing of Environment*, *114*(1), 168–182. https://doi.org/10.1016/j.rse.2009.08.016

Fu, D., Worden, J. R., Liu, X., Kulawik, S. S., Bowman, K. W., & Natraj, V. (2013). Characterization of ozone profiles derived from Aura TES and OMI radiances. *Atmospheric Chemistry and Physics*, *13*(6), 3445–3462. https://doi.org/10.5194/acp-13-3445-2013

Gaudel, A., Cooper, O. R., Ancellet, G., Barret, B., Boynard, A., Burrows, J. P., Clerbaux, C., Coheur, P.-F., Cuesta, J., Cuevas, E., Doniki, S., Dufour, G., Ebojie, F., Foret, G., Garcia, O., Granados-Muñoz, M. J., Hannigan, J. W., Hase, F., Hassler, B., … Ziemke, J. (2018). Tropospheric Ozone Assessment Report: Present-day distribution and trends of tropospheric ozone relevant to climate and global atmospheric chemistry model evaluation. *Elementa: Science of the Anthropocene*, *6*, 39. https://doi.org/10.1525/elementa.291

Gordon, I. E., Rothman, L. S., Hargreaves, R. J., Hashemi, R., Karlovets, E. V., Skinner, F. M., Conway, E. K., Hill, C., Kochanov, R. V., Tan, Y., Wcisło, P., Finenko, A. A., Nelson, K., Bernath, P. F., Birk, M., Boudon, V., Campargue, A., Chance, K. V., Coustenis, A., … Yurchenko, S. N. (2022). The HITRAN2020 molecular spectroscopic database. *Journal of Quantitative Spectroscopy and Radiative Transfer*, *277*, 107949. https://doi.org/10.1016/j.jqsrt.2021.107949

Guenther, A. B., Jiang, X., Heald, C. L., Sakulyanontvittaya, T., Duhl, T., Emmons, L. K., & Wang, X. (2012). The Model of Emissions of Gases and Aerosols from Nature version 2.1 (MEGAN2.1): An extended and updated framework for modeling biogenic emissions. *Geoscientific Model Development*, *5*(6), 1471–1492. https://doi.org/10.5194/gmd-5-1471-2012

Hudman, R. C., Moore, N. E., Mebust, A. K., Martin, R. V., Russell, A. R., Valin, L. C., & Cohen, R. C. (2012). Steps towards a mechanistic model of global soil nitric oxide emissions: Implementation and space based-constraints. *Atmospheric Chemistry and Physics*, *12*(16), 7779–7795. https://doi.org/10.5194/acp-12-7779-2012

Janssens-Maenhout, G., Crippa, M., Guizzardi, D., Dentener, F., Muntean, M., Pouliot, G., Keating, T., Zhang, Q., Kurokawa, J., Wankmüller, R., Denier Van Der Gon, H., Kuenen, J. J. P., Klimont, Z., Frost, G., Darras, S., Koffi, B., & Li, M. (2015). HTAP_v2.2: A mosaic of regional and global emission grid maps for 2008 and 2010 to study hemispheric transport of air pollution. *Atmospheric Chemistry and Physics*, *15*(19), 11411–11432. https://doi.org/10.5194/acp-15-11411-2015

Joiner, J., Schoeberl, M. R., Vasilkov, A. P., Oreopoulos, L., Platnick, S., Livesey, N. J., & Levelt, P. F. (2009). Accurate satellite-derived estimates of the tropospheric ozone impact on the global radiation budget. *Atmospheric Chemistry and Physics*, *9*(13), 4447–4465. https://doi.org/10.5194/acp-9-4447-2009

Keller, C. A., Long, M. S., Yantosca, R. M., Da Silva, A. M., Pawson, S., & Jacob, D. J. (2014). HEMCO v1.0: A versatile, ESMF-compliant component for calculating emissions in atmospheric models. *Geoscientific Model Development*, *7*(4), 1409–1417. https://doi.org/10.5194/gmd-7-1409-2014

Keller, C. A., Knowland, K. E., Duncan, B. N., Liu, J., Anderson, D. C., Das, S., Lucchesi, R. A., Lundgren, E. W., Nicely, J. M., Nielsen, E., Ott, L. E., Saunders, E., Strode, S. A.,

Wales, P. A., Jacob, D. J., & Pawson, S. (2021). Description of the NASA GEOS Composition Forecast Modeling System GEOS-CF v1.0. *Journal of Advances in Modeling Earth Systems*, *13*(4), e2020MS002413. https://doi.org/10.1029/2020MS002413

Keppens, A., Di Pede, S., Hubert, D., Lambert, J.-C., Veefkind, P., Sneep, M., De Haan, J., Ter Linden, M., Leblanc, T., Compernolle, S., Verhoelst, T., Granville, J., Nath, O., Fjæraa, A. M., Boyd, I., Niemeijer, S., Van Malderen, R., Smit, H. G. J., Duflot, V., … Zehner, C. (2024). 5 years of Sentinel-5P TROPOMI operational ozone profiling and geophysical validation using ozonesonde and lidar ground-based networks. *Atmospheric Measurement Techniques*, *17*(13), 3969–3993. https://doi.org/10.5194/amt-17-3969-2024

Kim, J., Jeong, U., Ahn, M.-H., Kim, J. H., Park, R. J., Lee, H., Song, C. H., Choi, Y.-S., Lee, K.-H., Yoo, J.-M., Jeong, M.-J., Park, S. K., Lee, K.-M., Song, C.-K., Kim, S.-W., Kim, Y. J., Kim, S.-W., Kim, M., Go, S., … Choi, Y. (2020). New Era of Air Quality Monitoring from Space: Geostationary Environment Monitoring Spectrometer (GEMS). *Bulletin of the American Meteorological Society*, *101*(1), E1–E22. https://doi.org/10.1175/BAMS-D-18-0013.1

Kim, P. S., Jacob, D. J., Liu, X., Warner, J. X., Yang, K., Chance, K., Thouret, V., & Nedelec, P. (2013). Global ozone–CO correlations from OMI and AIRS: Constraints on tropospheric ozone sources. *Atmospheric Chemistry and Physics*, *13*(18), 9321–9335. https://doi.org/10.5194/acp-13-9321-2013

Knowland, K. E., Keller, C. A., Wales, P. A., Wargan, K., Coy, L., Johnson, M. S., Liu, J., Lucchesi, R. A., Eastham, S. D., Fleming, E., Liang, Q., Leblanc, T., Livesey, N. J., Walker, K. A., Ott, L. E., & Pawson, S. (2022a). NASA GEOS Composition Forecast Modeling System GEOS-CF v1.0: Stratospheric Composition. *Journal of Advances in Modeling Earth Systems*, *14*(6), e2021MS002852. https://doi.org/10.1029/2021MS002852

Knowland, K. E., Keller, C. A., & Lucchesi, R. (2022b). *File Specification for GEOS-CF Products*. GMAO Office Note No. 17 (Version 1.3). https://gmao.gsfc.nasa.gov/pubs/office_notes

Kokaly, R. F., Clark, R. N., Swayze, G. A., Livo, K. E., Hoefen, T. M., Pearson, N. C., Wise, R. A., Benzel, W., Lowers, H. A., Driscoll, R. L., & Klein, A. J. (2017). USGS Spectral Library Version 7. In *Data Series* (No. 1035). U.S. Geological Survey. https://doi.org/10.3133/ds1035

Lacis, A. A., Wuebbles, D. J., & Logan, J. A. (1990). Radiative forcing of climate by changes in the vertical distribution of ozone. *Journal of Geophysical Research: Atmospheres*, *95*(D7), 9971–9981. https://doi.org/10.1029/JD095iD07p09971

Lee, G. T., Park, R. J., Kwon, H.-A., Ha, E. S., Lee, S. D., Shin, S., Ahn, M.-H., Kang, M., Choi, Y.-S., Kim, G., Lee, D.-W., Kim, D.-R., Hong, H., Langerock, B., Vigouroux, C., Lerot, C., Hendrick, F., Pinardi, G., De Smedt, I., … Kim, J. (2024). First evaluation of the GEMS formaldehyde product against TROPOMI and ground-based column measurements during the in-orbit test period. *Atmospheric Chemistry and Physics*, *24*(8), 4733–4749. https://doi.org/10.5194/acp-24-4733-2024

Levelt, P. F., Oord, G. H. J. V. D., Dobber, M. R., Mälkki, A., Visser, H., Vries, J. D., Stammes, P., Lundell, J. O. V., & Saari, H. (2006). The Ozone Monitoring Instrument. *IEEE Trans. Geosci. Remote Sens.*, *44*(5), 1093–1101.

Liu, X., Chance, K., Sioris, C. E., Spurr, R. J. D., Kurosu, T. P., Martin, R. V., & Newchurch, M. J. (2005). Ozone profile and tropospheric ozone retrievals from the Global Ozone Monitoring Experiment: Algorithm description and validation. *Journal of Geophysical Research: Atmospheres*, *110*(D20), 2005JD006240. https://doi.org/10.1029/2005JD006240

Liu, X., Chance, K., Sioris, C. E., & Kurosu, T. P. (2007). Impact of using different ozone cross sections on ozone profile retrievals from Global Ozone Monitoring Experiment (GOME) ultraviolet measurements. *Atmospheric Chemistry and Physics*, *7*(13), 3571–3578. https://doi.org/10.5194/acp-7-3571-2007

Liu, X., Bhartia, P. K., Chance, K., Spurr, R. J. D., & Kurosu, T. P. (2010a). Ozone profile retrievals from the Ozone Monitoring Instrument. *Atmospheric Chemistry and Physics*, *10*(5), 2521–2537. https://doi.org/10.5194/acp-10-2521-2010

Liu, X., Bhartia, P. K., Chance, K., Froidevaux, L., Spurr, R. J. D., & Kurosu, T. P. (2010b). Validation of Ozone Monitoring Instrument (OMI) ozone profiles and stratospheric ozone columns with Microwave Limb Sounder (MLS) measurements. *Atmospheric Chemistry and Physics*, *10*(5), 2539–2549. https://doi.org/10.5194/acp-10-2539-2010

Liu, C., Liu, X., & Chance, K. (2013). The impact of using different ozone cross sections on ozone profile retrievals from OMI UV measurements. *Journal of Quantitative Spectroscopy and Radiative Transfer*, *130*, 365–372. https://doi.org/10.1016/j.jqsrt.2013.06.006

Liu, C., Liu, X., Kowalewski, M. G., Janz, S. J., González Abad, G., Pickering, K. E., Chance, K., & Lamsal, L. N. (2015). Characterization and verification of ACAM slit functions for trace-gas retrievals during the 2011 DISCOVER-AQ flight campaign. *Atmospheric Measurement Techniques*, *8*(2), 751–759. https://doi.org/10.5194/amt-8-751-2015

Liu, F., Choi, S., Li, C., Fioletov, V. E., McLinden, C. A., Joiner, J., Krotkov, N. A., Bian, H., Janssens-Maenhout, G., Darmenov, A. S., & Da Silva, A. M. (2018). A new global anthropogenic SO_2 emission inventory for the last decade: A mosaic of satellite-derived and bottom-up emissions. *Atmospheric Chemistry and Physics*, *18*(22), 16571–16586. https://doi.org/10.5194/acp-18-16571-2018

Lucchesi, R. (2013, June 11). *File Specification for GEOS-5 FP (Forward Processing)*. https://ntrs.nasa.gov/citations/20150001437

M. Birk & G. Wagner. (2021). *ESA SEOM-IAS – Measurement and ACS database O3 UV region* (Version II) [Dataset]. Zenodo. https://doi.org/10.5281/ZENODO.4423918

Malicet, J., Daumont, D., Charbonnier, J., Parisse, C., Chakir, A., & Brion, J. (1995). Ozone UV spectroscopy. II. Absorption cross-sections and temperature dependence. *Journal of Atmospheric Chemistry*, *21*(3), 263–273. https://doi.org/10.1007/BF00696758

Mao, J., Paulot, F., Jacob, D. J., Cohen, R. C., Crounse, J. D., Wennberg, P. O., Keller, C. A., Hudman, R. C., Barkley, M. P., & Horowitz, L. W. (2013). Ozone and organic nitrates over the eastern United States: Sensitivity to isoprene chemistry. *Journal of Geophysical Research: Atmospheres*, *118*(19). https://doi.org/10.1002/jgrd.50817

Marais, E. A., Jacob, D. J., Jimenez, J. L., Campuzano-Jost, P., Day, D. A., Hu, W., Krechmer, J., Zhu, L., Kim, P. S., Miller, C. C., Fisher, J. A., Travis, K., Yu, K., Hanisco, T. F., Wolfe, G. M., Arkinson, H. L., Pye, H. O. T., Froyd, K. D., Liao, J., & McNeill, V. F. (2016). Aqueous-phase mechanism for secondary organic aerosol formation from isoprene: Application to the southeast United States and co-benefit of SO_2 emission

controls. *Atmospheric Chemistry and Physics*, *16*(3), 1603–1618. https://doi.org/10.5194/acp-16-1603-2016

McPeters, R. D., Labow, G. J., & Logan, J. A. (2007). Ozone climatological profiles for satellite retrieval algorithms. *Journal of Geophysical Research: Atmospheres*, *112*(D5), 2005JD006823. https://doi.org/10.1029/2005JD006823

McPeters, R. D., & Labow, G. J. (2012). Climatology 2011: An MLS and sonde derived ozone climatology for satellite retrieval algorithms. *Journal of Geophysical Research: Atmospheres*, *117*(D10), 2011JD017006. https://doi.org/10.1029/2011JD017006

Meijer, Y. J., Swart, D. P. J., Baier, F., Bhartia, P. K., Bodeker, G. E., Casadio, S., Chance, K., Del Frate, F., Erbertseder, T., Felder, M. D., Flynn, L. E., Godin-Beekmann, S., Hansen, G., Hasekamp, O. P., Kaifel, A., Kelder, H. M., Kerridge, B. J., Lambert, J. -C., Landgraf, J., … Zehner, C. (2006). Evaluation of Global Ozone Monitoring Experiment (GOME) ozone profiles from nine different algorithms. *Journal of Geophysical Research: Atmospheres*, *111*(D21), 2005JD006778. https://doi.org/10.1029/2005JD006778

Munro, R., Lang, R., Klaes, D., Poli, G., Retscher, C., Lindstrot, R., Huckle, R., Lacan, A., Grzegorski, M., Holdak, A., Kokhanovsky, A., Livschitz, J., & Eisinger, M. (2016). The GOME-2 instrument on the Metop series of satellites: Instrument design, calibration, and level 1 data processing—An overview. *Atmospheric Measurement Techniques*, *9*(3), 1279–1301. https://doi.org/10.5194/amt-9-1279-2016

Murray, L. T., Jacob, D. J., Logan, J. A., Hudman, R. C., & Koshak, W. J. (2012). Optimized regional and interannual variability of lightning in a global chemical transport model constrained by LIS/OTD satellite data. *Journal of Geophysical Research: Atmospheres*, *117*(D20), 2012JD017934. https://doi.org/10.1029/2012JD017934

Natraj, V., Liu, X., Kulawik, S., Chance, K., Chatfield, R., Edwards, D. P., Eldering, A., Francis, G., Kurosu, T., Pickering, K., Spurr, R., & Worden, H. (2011). Multi-spectral sensitivity studies for the retrieval of tropospheric and lowermost tropospheric ozone from simulated clear-sky GEO-CAPE measurements. *Atmospheric Environment*, *45*(39), 7151–7165. https://doi.org/10.1016/j.atmosenv.2011.09.014

Noël, S., Bramstedt, K., Bovensmann, H., Gerilowski, K., Burrows, J. P., Standfuss, C., Dufour, E., & Veihelmann, B. (2012). Quantification and mitigation of the impact of scene inhomogeneity on Sentinel-4 UVN UV-VIS retrievals. *Atmospheric Measurement Techniques*, *5*(6), 1319–1331. https://doi.org/10.5194/amt-5-1319-2012

Nowlan, C. R., Liu, X., Chance, K., Cai, Z., Kurosu, T. P., Lee, C., & Martin, R. V. (2011). Retrievals of sulfur dioxide from the Global Ozone Monitoring Experiment 2 (GOME-2) using an optimal estimation approach: Algorithm and initial validation. *Journal of Geophysical Research*, *116*(D18), D18301. https://doi.org/10.1029/2011JD015808

Oda, T., Maksyutov, S., & Andres, R. J. (2018). The Open-source Data Inventory for Anthropogenic CO_2 , version 2016 (ODIAC2016): A global monthly fossil fuel CO_2 gridded emissions data product for tracer transport simulations and surface flux inversions. *Earth System Science Data*, *10*(1), 87–107. https://doi.org/10.5194/essd-10-87-2018

Park, J., Liu, X., Houck, J., & Chance, K. (2025). *Ozone Profile Level 2 and 3 Data products: User Guide V2.0*. https://doi.org/10.5067/DOC/TEMPO/O3PROF_L2-3USERGUIDE_V2.0

Park, J., Liu, X., Houck, J., & Chance, K. (2026). *Ozone Profile Level 2 and 3 Data products: User Guide V2.1*. https://doi.org/10.5067/DOC/TEMPO/O3PROF_L2-3USERGUIDE_V2.1

Parrella, J. P., Jacob, D. J., Liang, Q., Zhang, Y., Mickley, L. J., Miller, B., Evans, M. J., Yang, X., Pyle, J. A., Theys, N., & Van Roozendael, M. (2012). Tropospheric bromine chemistry: Implications for present and pre-industrial ozone and mercury. *Atmospheric Chemistry and Physics*, *12*(15), 6723–6740. https://doi.org/10.5194/acp-12-6723-2012

Pope, R. M., & Fry, E. S. (1997). Absorption spectrum (380–700 nm) of pure water II Integrating cavity measurements. *Applied Optics*, *36*(33), 8710. https://doi.org/10.1364/AO.36.008710

Qin, W., Fasnacht, Z., Haffner, D., Vasilkov, A., Joiner, J., Krotkov, N., Fisher, B., & Spurr, R. (2019). A geometry-dependent surface Lambertian-equivalent reflectivity product for UV–Vis retrievals – Part 1: Evaluation over land surfaces using measurements from OMI at 466 nm. *Atmospheric Measurement Techniques*, *12*(7), 3997–4017. https://doi.org/10.5194/amt-12-3997-2019

Reich, P. B., & Amundson, R. G. (1985). Ambient Levels of Ozone Reduce Net Photosynthesis in Tree and Crop Species. *Science*, *230*(4725), 566–570. https://doi.org/10.1126/science.230.4725.566

Rodgers, C. D. (2000). *Inverse Methods for Atmospheric Sounding: Theory and Practice* (Vol. 2). WORLD SCIENTIFIC. https://doi.org/10.1142/3171

Rodgers, C. D., & Connor, B. J. (2003). Intercomparison of remote sounding instruments. *Journal of Geophysical Research: Atmospheres*, *108*(D3), 2002JD002299. https://doi.org/10.1029/2002JD002299

Schaaf, C., & Wang, Z. (2015a). *MCD43C1 MODIS/Terra+Aqua BRDF/AlbedoModel Parameters Daily L3 Global 0.05Deg CMG V006* [Dataset]. NASA Land Processes Distributed Active Archive Center. https://doi.org/10.5067/MODIS/MCD43C1.006

Schaaf, C., & Wang, Z. (2015b). *MCD43C2 MODIS/Terra+Aqua BRDF/Albedo Snow-free Model Parameters Daily L3 Global 0.05Deg CMG V006* [Dataset]. NASA Land Processes Distributed Active Archive Center. https://doi.org/10.5067/MODIS/MCD43C2.006

Schultz, M. G., Heil, A., Hoelzemann, J. J., Spessa, A., Thonicke, K., Goldammer, J. G., Held, A. C., Pereira, J. M. C., & Van Het Bolscher, M. (2008). Global wildland fire emissions from 1960 to 2000. *Global Biogeochemical Cycles*, *22*(2), 2007GB003031. https://doi.org/10.1029/2007GB003031

Sellitto, P., Del Frate, F., Solimini, D., & Casadio, S. (2012). Tropospheric Ozone Column Retrieval From ESA-Envisat SCIAMACHY Nadir UV/VIS Radiance Measurements by Means of a Neural Network Algorithm. *IEEE Transactions on Geoscience and Remote Sensing*, *50*(3), 998–1011. https://doi.org/10.1109/TGRS.2011.2163198

Sellitto, P., Di Noia, A., Del Frate, F., Burini, A., Casadio, S., & Solimini, D. (2012). On the role of visible radiation in ozone profile retrieval from nadir UV/VIS satellite measurements: An experiment with neural network algorithms inverting SCIAMACHY data. *Journal of Quantitative Spectroscopy and Radiative Transfer*, *113*(12), 1429–1436. https://doi.org/10.1016/j.jqsrt.2012.04.007

Sherwen, T., Schmidt, J. A., Evans, M. J., Carpenter, L. J., Großmann, K., Eastham, S. D., Jacob, D. J., Dix, B., Koenig, T. K., Sinreich, R., Ortega, I., Volkamer, R., Saiz-Lopez, A., Prados-Roman, C., Mahajan, A. S., & Ordóñez, C. (2016). Global impacts of

tropospheric halogens (Cl, Br, I) on oxidants and composition in GEOS-Chem. *Atmospheric Chemistry and Physics*, *16*(18), 12239–12271. https://doi.org/10.5194/acp-16-12239-2016

Sioris, C. E., & Evans, W. F. J. (2000). Impact of rotational Raman scattering in the O_2 *A* band. *Geophysical Research Letters*, *27*(24), 4085–4088. https://doi.org/10.1029/2000GL012231

Spurr, R. J. D. (2006). VLIDORT: A linearized pseudo-spherical vector discrete ordinate radiative transfer code for forward model and retrieval studies in multilayer multiple scattering media. *Journal of Quantitative Spectroscopy and Radiative Transfer*, *102*(2), 316–342. https://doi.org/10.1016/j.jqsrt.2006.05.005

Spurr, R. (2008). LIDORT and VLIDORT: Linearized pseudo-spherical scalar and vector discrete ordinate radiative transfer models for use in remote sensing retrieval problems. In A. A. Kokhanovsky (Ed.), *Light Scattering Reviews 3: Light Scattering and Reflection* (pp. 229–275). Springer. https://doi.org/10.1007/978-3-540-48546-9_7

Spurr, R., Natraj, V., Lerot, C., Van Roozendael, M., & Loyola, D. (2013). Linearization of the Principal Component Analysis method for radiative transfer acceleration: Application to retrieval algorithms and sensitivity studies. *Journal of Quantitative Spectroscopy and Radiative Transfer*, *125*, 1–17. https://doi.org/10.1016/j.jqsrt.2013.04.002

Sun, K., Liu, X., Huang, G., González Abad, G., Cai, Z., Chance, K., & Yang, K. (2017). Deriving the slit functions from OMI solar observations and its implications for ozone-profile retrieval. *Atmospheric Measurement Techniques*, *10*(10), 3677–3695. https://doi.org/10.5194/amt-10-3677-2017

Sun, K., Yousefi, M., Chan Miller, C., Chance, K., González Abad, G., Gordon, I. E., Liu, X., O'Sullivan, E., Sioris, C. E., & Wofsy, S. C. (2022). An optimal estimation-based retrieval of upper atmospheric oxygen airglow and temperature from SCIAMACHY limb observations. *Atmospheric Measurement Techniques*, *15*(12), 3721–3745. https://doi.org/10.5194/amt-15-3721-2022

TEMPO Validation Team and TEMPO Ad-hoc Working Group. (2023). *TROPOSPHERIC EMISSIONS: MONITORING OF POLLUTION (TEMPO) PROJECT Level 2 Science Data Product Validation Plan*.

Thalman, R., & Volkamer, R. (2013). Temperature dependent absorption cross-sections of O2–O2 collision pairs between 340 and 630 nm and at atmospherically relevant pressure. *Physical Chemistry Chemical Physics*, *15*(37), 15371. https://doi.org/10.1039/c3cp50968k

Thompson, A. M. (1992). The Oxidizing Capacity of the Earth's Atmosphere: Probable Past and Future Changes. *Science*, *256*(5060), 1157–1165. https://doi.org/10.1126/science.256.5060.1157

Tilstra, L. G., Tuinder, O. N. E., Wang, P., & Stammes, P. (2017). Surface reflectivity climatologies from UV to NIR determined from Earth observations by GOME-2 and SCIAMACHY. *Journal of Geophysical Research: Atmospheres*, *122*(7), 4084–4111. https://doi.org/10.1002/2016JD025940

van der Gon, H. D., Hendriks, C., Kuenen, J., Segers, A., & Visschedijk, A. (2011, December). *TNO Report: Description of current temporal emission patterns and sensitivity of predicted AQ for temporal emission patterns*.

Vandaele, A. C., Hermans, C., Simon, P. C., Carleer, M., Colin, R., Fally, S., Mérienne, M. F., Jenouvrier, A., & Coquart, B. (1998). Measurements of the NO2 absorption cross-section

from 42 000 cm−1 to 10 000 cm−1 (238–1000 nm) at 220 K and 294 K. *Journal of Quantitative Spectroscopy and Radiative Transfer*, *59*(3–5), 171–184. https://doi.org/10.1016/S0022-4073(97)00168-4

Veefkind, J. P., Aben, I., McMullan, K., Förster, H., de Vries, J., Otter, G., Claas, J., Eskes, H. J., de Haan, J. F., Kleipool, Q., van Weele, M., Hasekamp, O., Hoogeveen, R., Landgraf, J., Snel, R., Tol, P., Ingmann, P., Voors, R., Kruizinga, B., … Levelt, P. F. (2012). TROPOMI on the ESA Sentinel-5 Precursor: A GMES mission for global observations of the atmospheric composition for climate, air quality and ozone layer applications. *Remote Sensing of Environment*, *120*(2012), 70–83. https://doi.org/10.1016/j.rse.2011.09.027

Voors, R., Dobber, M., Dirksen, R., & Levelt, P. (2006). Method of calibration to correct for cloud-induced wavelength shifts in the Aura satellite's Ozone Monitoring Instrument. *Applied Optics*, *45*(15), 3652. https://doi.org/10.1364/AO.45.003652

Wang, H., Nowlan, C. R., González Abad, G., Chong, H., Hou, W., Houck, J. C., Liu, X., Chance, K., Yang, E., Vasilkov, A., Joiner, J., Qin, W., Fasnacht, Z., Knowland, K. E., Chan Miller, C., Spurr, R. J. D., Flittner, D. E., Carr, J. L., Suleiman, R. M., … Fitzmaurice, J. A. (2025). Algorithm Theoretical Basis for Version 3 TEMPO O_2 -O_2 Cloud Product. *Earth and Space Science*, *12*(2), e2024EA004165. https://doi.org/10.1029/2024EA004165

Wargan, K., Pawson, S., Olsen, M. A., Witte, J. C., Douglass, A. R., Ziemke, J. R., Strahan, S. E., & Nielsen, J. E. (2015). The global structure of upper troposphere-lower stratosphere ozone in GEOS-5: A multiyear assimilation of EOS Aura data. *Journal of Geophysical Research: Atmospheres*, *120*(5), 2013–2036. https://doi.org/10.1002/2014JD022493

Wilmouth, D. M., Hanisco, T. F., Donahue, N. M., & Anderson, J. G. (1999). Fourier Transform Ultraviolet Spectroscopy of the $A^2\,\Pi_{3/2} \leftarrow X^2\,\Pi_{3/2}$ Transition of BrO. *The Journal of Physical Chemistry A*, *103*(45), 8935–8945. https://doi.org/10.1021/jp991651o

Worden, H. M., Bowman, K. W., Worden, J. R., Eldering, A., & Beer, R. (2008). Satellite measurements of the clear-sky greenhouse effect from tropospheric ozone. *Nature Geoscience*, *1*(5), 305–308. https://doi.org/10.1038/ngeo182

Zhao, F., Liu, C., Cai, Z., Liu, X., Bak, J., Kim, J., Hu, Q., Xia, C., Zhang, C., Sun, Y., Wang, W., & Liu, J. (2021). Ozone profile retrievals from TROPOMI: Implication for the variation of tropospheric ozone during the outbreak of COVID-19 in China. *Science of The Total Environment*, *764*, 142886. https://doi.org/10.1016/j.scitotenv.2020.142886

Zhou, Y., Brunner, D., Boersma, K. F., Dirksen, R., & Wang, P. (2009). An improved tropospheric NO_2 retrieval for OMI observations in the vicinity of mountainous terrain. *Atmospheric Measurement Techniques*, *2*(2), 401–416. https://doi.org/10.5194/amt-2-401-2009

Ziemke, J. R., Olsen, M. A., Witte, J. C., Douglass, A. R., Strahan, S. E., Wargan, K., Liu, X., Schoeberl, M. R., Yang, K., Kaplan, T. B., Pawson, S., Duncan, B. N., Newman, P. A., Bhartia, P. K., & Heney, M. K. (2014). Assessment and applications of NASA ozone data products derived from Aura OMI/MLS satellite measurements in context of the GMI chemical transport model. *Journal of Geophysical Research: Atmospheres*, *119*(9), 5671–5699. https://doi.org/10.1002/2013JD020914

Zoogman, P., Liu, X., Chance, K., Sun, Q., Schaaf, C., Mahr, T., & Wagner, T. (2016). A climatology of visible surface reflectance spectra. *Journal of Quantitative Spectroscopy and Radiative Transfer*, *180*, 39–46. https://doi.org/10.1016/j.jqsrt.2016.04.003

Zoogman, P., Liu, X., Suleiman, R. M., Pennington, W. F., Flittner, D. E., Al-Saadi, J. A., Hilton, B. B., Nicks, D. K., Newchurch, M. J., Carr, J. L., Janz, S. J., Andraschko, M. R., Arola, A., Baker, B. D., Canova, B. P., Chan Miller, C., Cohen, R. C., Davis, J. E., Dussault, M. E., … Chance, K. (2017). Tropospheric emissions: Monitoring of pollution (TEMPO). *Journal of Quantitative Spectroscopy and Radiative Transfer*, *186*(2017), 17–39. https://doi.org/10.1016/j.jqsrt.2016.05.008